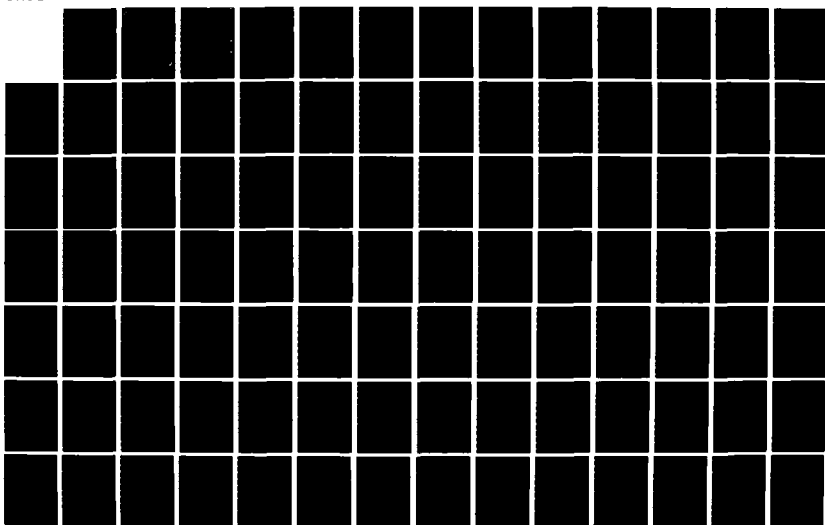
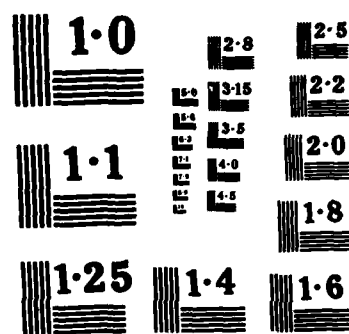
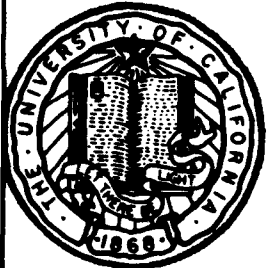


AD-A157 270 BEAM STEERING OF ELECTRICALLY SEGMENTED PIEZO-CERAMIC 1/2  
ULTRASONIC TRANSDUC. (U) SCRIPPS INSTITUTION OF  
OCEANOGRAPHY LA JOLLA CA MARINE PHYSIC. H ESLAMBOLCHI  
UNCLASSIFIED 01 DEC 84 MPL-U-76/84 N00014-80-C-0220 F/G 20/1 NL





NATIONAL BUREAU OF STANDARDS  
MICROCOPY RESOLUTION TEST CHART



AD-A157 270

**BEAM STEERING OF ELECTRICALLY SEGMENTED  
PIEZOCERAMIC ULTRASONIC TRANSDUCERS  
USING NORMAL MODE COUPLING**

Hossein Eslambolchi

Sponsored by the  
Office of Naval Research  
Contract N00014-80-C-0220  
and in part by the  
National Oceanic and Atmospheric Administration  
National Sea Grant College Program  
Grant NA80AA-D-00120  
Project Number R/OT-3

*Approved for public release; distribution unlimited.*

**SIO REFERENCE 84-38**

December 1, 1984

AUG 5 1985  
D 25 016  
7 25 016  
8 5

**MARINE PHYSICAL LABORATORY**  
of the Scripps Institution of Oceanography  
San Diego, California 92152

## **DISCLAIMER NOTICE**

**THIS DOCUMENT IS BEST QUALITY  
PRACTICABLE. THE COPY FURNISHED  
TO DTIC CONTAINED A SIGNIFICANT  
NUMBER OF PAGES WHICH DO NOT  
REPRODUCE LEGIBLY.**

REPORT DOCUMENTATION PAGE		READ INSTRUCTIONS BEFORE COMPLETING FORM
1. REPORT NUMBER SIO REFERENCE 84-38	2. GOVT ACCESSION NO.	3. RECIPIENT'S CATALOG NUMBER
4. TITLE (and Subtitle) BEAM STEERING OF ELECTRICALLY SEGMENTED PIEZO-CERAMIC ULTRASONIC TRANSDUCERS USING NORMAL MODE COUPLING		5. TYPE OF REPORT & PERIOD COVERED Summary
7. AUTHOR(s) Hossein Eslambolchi		6. PERFORMING ORG. REPORT NUMBER MPL-U-76/84
8. CONTRACT OR GRANT NUMBER(s) N00014-80-C-0220 and NA80AA-D-00120		9. PERFORMING ORGANIZATION NAME AND ADDRESS University of California, San Diego, Marine Physical Laboratory of the Scripps Institution of Oceanography, San Diego, California 92152
11. CONTROLLING OFFICE NAME AND ADDRESS Office of Naval Research, Department of the Navy, 800 North Quincy Street, Arlington, Virginia 22209		10. PROGRAM ELEMENT, PROJECT, TASK AREA & WORK UNIT NUMBERS
14. MONITORING AGENCY NAME & ADDRESS (if different from Controlling Office)		12. REPORT DATE 1984
		13. NUMBER OF PAGES 182 pages
		15. SECURITY CLASS. (of this report) Unclassified
		16a. DECLASSIFICATION/DOWNGRADING SCHEDULE
16. DISTRIBUTION STATEMENT (of this Report)  Approved for public release; distribution unlimited.		
17. DISTRIBUTION STATEMENT (of the abstract entered in Block 20, if different from Report)		
18. SUPPLEMENTARY NOTES		
19. KEY WORDS (Continue on reverse side if necessary and identify by block number)  mode coupling, piezoelectric plates, dispersion curve		
20. ABSTRACT (Continue on reverse side if necessary and identify by block number)  It is well known that normal mode coupling in large diameter piezoelectric plates causes serious difficulties when attempting to operate over wide frequency bands. As a consequence transducers are commonly constructed as a mosaic of elemental resonators, each of which has a predominant single mode of mechanical oscillation at the frequency of interest. Such transducer arrays may be electrically steered to angles other than normal by applying different phases of driving voltages to different elements.		

Continued

A continuous plate can also be used to steer a radiated beam using normal mode coupling in a narrow band system. The technique is to adjust the frequency of the driving voltage to match the travelling wave velocity of the normal mode which possesses the desired spatial phase relationship across the face of the plate. If the electrodes of a continuous piezoelectric plate are segmented so that regions of the plate can be driven with different phases, adjacent normal modes corresponding to a sine-cosine spatial phasing can be preferentially excited to generate a travelling wave. A true travelling wave will suppress the strong mirror lobe that would exist if a standing wave were excited. The velocity of the wave will be frequency dependent and the wavenumber can be controlled to generate a steered radiated beam.

In this research the theory of normal mode steering will be developed, the dispersion curve will be derived so the travelling wave velocities can be evaluated, and the effect of the mirror lobe due to the reflection from the edge boundary will be analyzed. Finally, the theory will then be verified by measurements on an experimental normal mode transducer which will be compared with a companion staved or mechanically segmented transducer.

UNIVERSITY OF CALIFORNIA

SAN DIEGO

Beam Steering of Electrically Segmented Piezo-Ceramic  
Ultrasonic Transducers Using Normal Mode Coupling

A dissertation submitted in partial satisfaction of the  
requirements for the degree of Doctor of Philosophy  
in Electrical Engineering  
(Applied Physics)

by

Hossein Eslambolchi

Committee in Charge:

Professor Victor C. Anderson, Chair

Professor Charles W. Vanatta

Professor Barney J. Rickett

Professor Manuel Rotenberg

Professor Kenneth M. Watson

1984



Accession For	
NTIS	GRA&I
DTIC TAB	<input type="checkbox"/>
Unannounced	<input type="checkbox"/>
Justification	
By	
Distribution/	
Availability Codes	
Avail and/or	Special
A1	

The dissertation of Hossein Eslambolchi is approved,  
and is acceptable in quality and form for  
publication on microfilm:

Daniel Rotsenberg  
Charles W. Van Atta  
R.J. Ricketts  
Kenneth M. Watson  
Victor C Anderson  
Chair

University of California, San Diego

1984

## TABLE OF CONTENTS

	Page
List of Symbols.....	vi
List of Figures.....	viii
Acknowledgments.....	xii
Vita, Publications and Fields of Study.....	xiii
Abstract .....	xiv
CHAPTER I INTRODUCTION.....	1
1. Statement of the Problem.....	2
2. Introduction.....	2
3. Background.....	4
4. Approach.....	6
5. Grating Lobe in Discrete and Continuous Plates.....	13
6. Phase Quantization.....	14
References.....	15
CHAPTER II THEORETICAL ANALYSIS.....	18
2.0 Introduction.....	19
2.1 Dispersion Curve.....	19

	Page
2.2 General Equations.....	23
2.3 Electrical Steering.....	45
2.4 Grating Lobe in a Discrete and Continuous Plate.....	48
References.....	72
 CHAPTER III EXPERIMENTAL ANALYSIS.....	 75
3.0 Introduction.....	76
3.1 Receiver/Transmitter.....	76
3.1.1 Transducer.....	77
3.1.2 Instrumentation System Design.....	86
3.1.3 Phasing Scheme.....	93
3.2 Experimental Analysis.....	94
3.2.1 Dispersion Curve.....	99
3.2.2 Grating Lobe.....	107
3.2.3 Mirror Lobe.....	122
3.2.4 Quantization Effect on the Lobes of the Discrete and Continuous Plate.....	132
 CHAPTER IV CONCLUSION.....	 169
4.0 Conclusion.....	170

## LIST OF SYMBOLS

$T_{ij}$	mechanical stress
$U_j$	mechanical displacement
$D_i$	electrical displacement
$S_{K\ell}$	mechanical strain
$E_K$	electrical field
$\psi_K$	potential function
$e_{Kij}$	piezoelectric stress constant
$K$	wavenumber
$\theta_0$	steering angle
$\rho$	mass density
$\epsilon_{ij}$	dielectric contant
$C_{ijk\ell}$	elastic constant
$L$	propagation wavenumber
$P$	thickness wavenumber
$\omega$	angular frequency
$\tau$	time
$\Omega$	normalized frequency
$\eta$	normalized wavenumber (propagation)
$\alpha$	normalized wavenumber (thickness)

$k_0$	driving wavenumber
$c_w$	speed of sound in water
$\theta$	physical angle
$D$	segment spacing
$\psi_H$	homogeneous solution (potential)
$\psi_{PS}$	particular solution (potential)
$2h$	thickness
$G_1$	normalization factor
$R_m$	individual amplitude of each element
$\bar{c}_{pq}$	normalized elastic constant
$\bar{e}_{ip}$	normalized piezoelectric stress constant
$\bar{\epsilon}_{ip}$	normalized dielectric constant
$\bar{\omega}$	normalized factor

## LIST OF FIGURES

	Page
CHAPTER I	
Fig. 1. Electrically acoustically isolated plate, discrete type.....	8
Fig. 2 Electrically isolated plate, continuous type.....	12
CHAPTER II	
Fig. 1 Coordinate of electrically segmented plate, continuous type.....	22
Fig. 2 Theoretical dispersion curve (normalized wavenumber vs. normalized frequency.....	44
Fig. 3 Theoretical dispersion curve (steering angle vs. frequency).....	47
Fig. 4 Theoretical spatial filtering function.....	50
Fig. 5 Theoretical beam pattern, $10^\circ$ steering, $2\lambda$ spacing, uniform shading, no spatial filtering.....	69
Fig. 6 Theoretical beam pattern, $10^\circ$ steering, $2\lambda$ , spacing, uniform shading, spatial filtering.....	71

### CHAPTER III

	Page
Fig. 1      Electrically acoustically isolated plate, discrete plate.....	80
Fig. 2      Electrically isolated plate, continuous plate.....	82
Fig. 3      Crystal mount package.....	84
Fig. 4      Test tank.....	88
Fig. 5      Instrumentation system design diagram.....	90
Fig. 6      Quantization of $\pi/8$ , four, three and two bit.....	96
Fig. 7      Quantization of $\pi/8$ , $\frac{1}{2}\lambda$ , $\lambda$ , $2\lambda$ spacing.....	98
Fig. 8      3-dimensional of beam pattern (right hand view).....	100
Fig. 9      3-dimensional of beam pattern (left hand view).....	102
Fig. 10     Experimental dispersion curve, (angle vs. frequency)...	105
Fig. 11     Theoretical beam pattern, $10^\circ$ steering, $2\lambda$ spacing, 4 bit quantization.....	109
Fig. 12     Experimental beam pattern, $10^\circ$ steering, $2\lambda$ spacing, 4 bit quantization.....	111
Fig. 13     Theoretical and experimental acoustic amplitude distribution of a continuous plate at $10^\circ$ steering....	114

	Page
Fig. 14 Theoretical beam pattern, 10° steering, $2\lambda$ , using FFT..	116
Fig. 15 Theoretical beam pattern, 10° steering, $2\lambda$ , using FFT, spatial filtering .....	118
Fig. 16 Experimental beam pattern, 10° steering, $2\lambda$ , 4 bit quantization.....	120
Fig. 17 Experimental beam pattern, mirror lobe.....	124
Fig. 18 Experimental beam pattern, mirror lobe suppressed.....	126
Fig. 19 3D view of 15° beam (right hand view).....	128
Fig. 20 3D view of 15° beam (left hand view).....	130
Fig. 21 3D view of 0° beam (right hand view).....	134
Fig. 22 3D view of 0° beam (left hand view).....	136
Fig. 23a Beam pattern, $\frac{1}{2}\lambda$ , 4 bit quantization, discrete plate..	138
Fig. 23b Beam pattern, $\frac{1}{2}\lambda$ , 3 bit quantization, discrete plate..	140
Fig. 23c Beam pattern, $\frac{1}{2}\lambda$ , 2 bit quantization, discrete plate..	142
Fig. 24a Beam pattern, $\frac{1}{2}\lambda$ , 4 bit quantization, continuous plate.....	145
Fig. 24b Beam pattern, $\frac{1}{2}\lambda$ , 3 bit quantization, continuous plate.....	147
Fig. 24c Beam pattern, $\frac{1}{2}\lambda$ , 2 bit quantization, continuous plate.....	149

	Page
Fig. 25a Beam pattern, 5° steering, 4 bit quantization, discrete plate.....	152
Fig. 25b Beam pattern, 5° steering, 3 bit quantization, discrete plate.....	154
Fig. 25c Beam pattern, 5° steering, 2 bit quantization, discrete plate.....	156
Fig. 26a Beam pattern, 5° steering, $2\lambda$ , 4 bit quantization, continuous plate.....	158
Fig. 26b Beam pattern, 5° steering, $2\lambda$ , 3 bit quantization, continuous plate.....	160
Fig. 26c Beam pattern, 5° steering, $2\lambda$ , 2 bit quantization, continuous plate.....	162
Fig. 27a Beam pattern, 10° steering, $\frac{1}{2}\lambda$ , 4 bit quantization, continuous plate.....	164
Fig. 27b Beam pattern, 10° steering, $\frac{1}{2}\lambda$ , 3 bit quantization, continuous plate.....	166
Fig. 27c Beam pattern, 10° steering, $\frac{1}{2}\lambda$ , 2 bit quantization, continuous plate.....	168

#### ACKNOWLEDGEMENTS

The completion of this dissertation would not have been possible without contributions from several people. For their technical as well as moral support I will always be grateful.

My sincere thanks to Professor Victor C. Anderson for his patience, guidance and encouragement in the supervision of this research project. His guidance had the greatest influence in the progress of my research.

I would like to thank Mr. Fred Ulman for his helpful and useful advice for segmenting the ultrasonic transducer.

Last and most of all, I thank my wife for her patience, tolerance and moral support.

This research was supported in part by the Office of Naval Research Contract N00014-80-C-0220 and by the National Oceanic and Atmospheric Administration, National Sea Grant College Program, Department of Commerce, under grant number NA80AA-D-00120, project number R/OT-3, through the California Sea Grant College Program, and in part by the California State Resources Agency. The U.S. Government is authorized to reproduce and distribute for governmental purposes.

## **VITA**

**Sept. 19, 1957 - Born - Tehran, Iran**

1980 BSEE, University of California, San Diego  
1981 MSEE, University of California, San Diego  
1984 Doctor of Philosophy, University of California, San Diego

## **PUBLICATIONS**

1982 Experimental TV with color mapped sonars

## **FIELDS OF STUDY**

**Major field: Electrical Engineering (Applied Physics)**

**Studies in TV/Sonar Imaging Systems**

**Professor Victor C. Anderson, University of California, S.D.**

**Studies in Normal-Mode Steering**

**Professor Victor C. Anderson, University of California, S.D.**

ABSTRACT OF THE DISSERTATION

Beam Steering of Electrically Segmented Piezo-Ceramic  
Ultrasonic Transducers Using Normal Mode Coupling

by

Hossein Eslambolchi

Doctor of Philosophy in Electrical Engineering  
(Applied Physics)

University of California, San Diego, 1984

Professor Victor C. Anderson, Chairman

It is well known that normal mode coupling in large diameter piezoelectric plates causes serious difficulties when attempting to operate over wide frequency bands. As a consequence transducers are commonly constructed as a mosaic of elemental resonators, each of which has a predominant single mode of mechanical oscillation at the frequency of interest. Such transducer arrays may be electrically steered to angles other than normal by applying different phases of driving

voltages to different elements. A continuous plate can also be used to steer a radiated beam using normal mode coupling in a narrow band system. The technique is to adjust the frequency of the driving voltage to match the travelling wave velocity of the normal mode which possesses the desired spatial phase relationship across the face of the plate. If the electrodes of a continuous piezoelectric plate are segmented so that regions of the plate can be driven with different phases, adjacent normal modes corresponding to a sine-cosine spatial phasing can be preferentially excited to generate a travelling wave. A true travelling wave will suppress the strong mirror lobe that would exist if a standing wave were excited. The velocity of the wave will be frequency dependent and the wave number can be controlled to generate a steered radiated beam.

In this research the theory of normal mode steering will be developed, the dispersion curve will be derived so the travelling wave velocities can be evaluated, and the effect of the mirror lobe due to the reflection from the edge boundary will be analyzed. Finally, the theory will then be verified by measurements on an experimental normal mode transducer which will be compared with a companion staved or mechanically segmented transducer.

CHAPTER I  
INTRODUCTION

### 1. Statement of the Problem

This thesis deals with electrically steering a piezoelectric plate transducer to generate an acoustic beam at angles other than normal to the plate while still retaining the high coupling associated with normal mode operation.

The theoretical analysis that treats the dispersion relation, reflections at the boundary, and grating lobe structure will be presented.

### 2. Introduction

In vibrating piezoelectric solids, many effects cause small changes in the natural frequency of the plate, corresponding to different vibrational modes with different amplitudes. These effects include such things as material stiffness, water loading of the surface, stiffening of the surface (due to the presence of a thin surface conducting sheet), the biassing stress, strains, and electric fields which may be applied.

When generating an acoustic beam at angles other than normal to the transducer plate, we are applying different phases of driving voltage to different sections of the transducer. This

phase difference causes a small change in the resonant frequency of the plate which corresponds to a different mode of mechanical oscillation.

Since the plate is driven close to its natural frequency, different modes with different amplitudes will be excited. But since we are applying different phases across the plate as we steer the beam electrically from normal, we are particularly looking for modes which have the same spatial phase distribution as the ones which we are applying. Therefore the problem is to find frequencies close to the plate's natural frequency which have the same spatial distribution. Finally, by matching these with the frequency of the driving voltage, the maximum response can be achieved. The advantage of this continuous plate with normal mode operation is that the grating lobe would be suppressed. By contrast, if one applies the phase distribution to a discrete segmented plate which has no normal mode coupling, the grating lobe will pose a major problem if the segments are wider than one-half wavelength.

### 3. Background

Wave propagation in a homogeneous infinite piezoelectric plate has been the subject of extensive investigation over the years. Rayleigh [1] gave the solution for an isotropic elastic plate and Ekstein [2] gave the solution for a particular anisotropic elastic plate. Since then several authors have calculated the roots of Rayleigh [3-7] and Ekstein [8-10] transcendental frequency equations in order to determine the resulting dispersion relations and solve high and low frequency vibrational problems. These solutions and calculations are applicable to purely elastic plates and to plates which obey the linear piezoelectric equations but which have low electro-mechanical coupling factors. However, certain polarized piezoelectric plates such as PZT-4, PZT-5 and PZT-7 which obey the linear piezoelectric equations have high electromechanical coupling factors; consequently the aforementioned solutions are inadequate to describe wave propagation in these plates.

Tiersten [11] solved the problem of wave propagation in an infinite piezoelectric plate belonging to the crystallographic class situated between shorted electrodes for two special orientations of the sixfold axis. The solution was derived using

the linear piezoelectric equations. He showed that for a given frequency and wave number in the propagation direction there are three independent solutions which are coupled at the traction-free boundaries of the plate. The dispersion curve was derived from the resulting transcendental equation. Tiersten's solution to derivation of the dispersion curve was focused on the unforced mechanical vibration where there is no electrical drive on the sections of the plate. This results in no electrical stress in the plate.

In later years Tiersten [12] solved the problem of the wave propagation by assuming that the plate is driven electrically with constant electric field in the plate and traction-free boundaries. The dispersion curve derived from his analysis is not too much different from the undriven plate. His electrical drive consisted of uniform amplitude and no phase distribution in the form of a constant electric field. He investigated different modes of wave propagation to determine which modes can be excited under electrical stress. Both symmetric and antisymmetric waves were analyzed. The different propagational modes contribute different spatial phase distributions in the plate with different acoustical amplitude distributions.

Bleustein [13] approached the problem of wave propagation in an infinite plate by assuming that there are perfectly thin electrodes coated on the surface of the plate and that the electrodes are short circuited. His solution results in zero potential on the two surfaces of the plate -- a boundary condition which is different from that which has been investigated in this thesis.

This thesis evaluates the dispersion curve for an infinite piezoelectric plate by assuming pressure release boundaries and a constant voltage but different phases to different sections of the plate. The theory will be analyzed in Chapter II and verified against the experimental data in Chapter III.

#### 4. Approach

Much research has been devoted to generating an acoustic beam at angles other than normal to the transducer plate using piezoelectric transducers. Up until now, transducers have usually been segmented by dicing the plate into elemental resonators which have been both electrically and acoustically isolated. Figure 1 shows such a segmented piezoelectric plate.

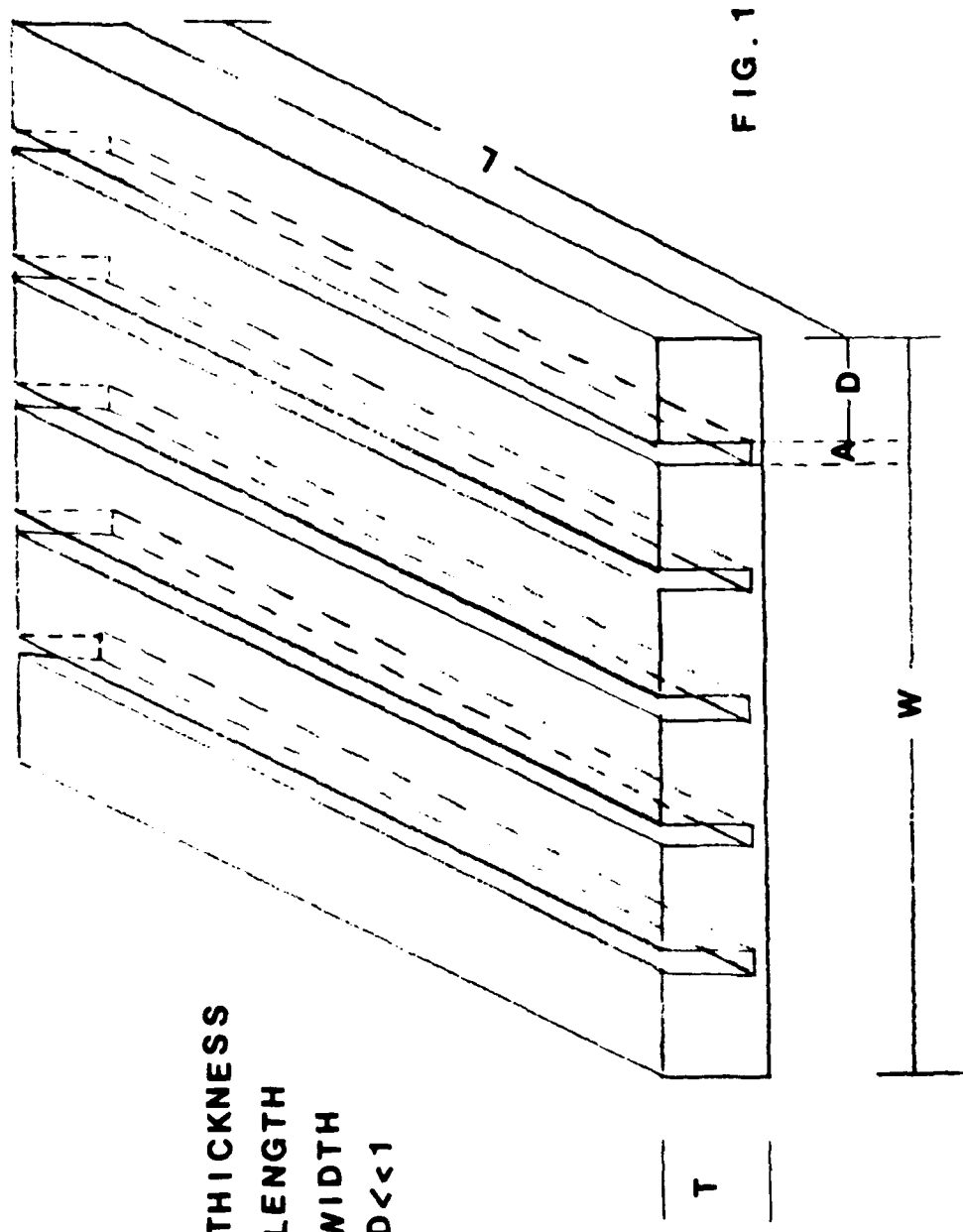


Fig. 1. Electrically acoustically isolated plate, discrete type.

For a segmented plate the simple dispersion equation can be written as

$$K_D^2 = K_x^2 + K_y^2 + K_z^2$$

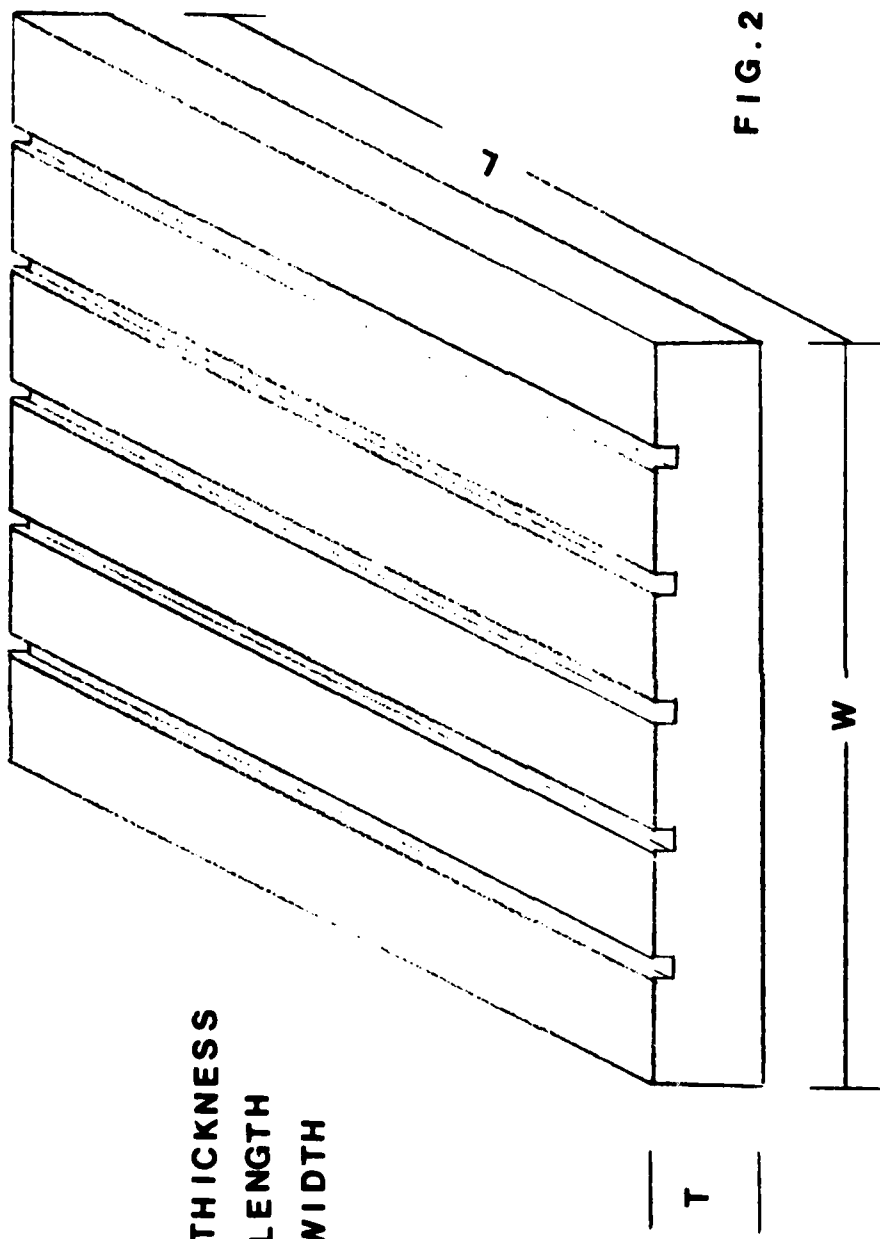
where  $K_D$  = wave number (discrete elemental resonator) and  $K_x$ ,  $K_y$  and  $K_z$  are wave numbers along  $x$ ,  $y$ ,  $z$ , respectively. The equation can be rewritten as:

$$\left(\frac{\omega}{C_S}\right)^2 = \left(\frac{n\pi}{L}\right)^2 + \left(\frac{m\pi}{D}\right)^2 + \left(\frac{p\pi}{T}\right)^2 \quad (1)$$

where  $L$ ,  $D$ , and  $T$  are length, width, and thickness of an elemental resonator,  $n$ ,  $m$ , and  $p$  are integers ( $0, 1, 2, \dots$ ), and  $C_S$  is the velocity in the plate. Since the plate is resonant in its fundamental mode of mechanical oscillation in the thickness direction,  $p=1$ ,  $m=n=0$ . For such a resonator, there exists not only this fundamental mode of mechanical oscillation but also other higher order modes ( $n, m > 0$ ) which are overtones in the frequency response of the plate. An array of these resonators can be electrically steered to angles other than normal by driving the individual elements at the main natural frequency, but applying different phases to the resonators.

An alternative approach that will be demonstrated here is to use a continuous plate to electrically steer a beam to angles other than normal by applying different phases of driving voltage to different electrodes. If the electrodes of a piezoelectric plate are segmented such that sections of the plate can be driven with different phases, then certain normal modes can be deliberately excited. This can be achieved in a continuous plate where there is normal mode coupling.

For a continuous plate the dispersion equation of (1) also applies, only the dimension differs. The dimensions of a continuous plate (Figure 2) are large with respect to a segmented discrete type; as a consequence there will be normal modes which are close to the natural mode of the plate. Because of the coupling in the plate, there exist normal modes with different amplitude and spatial phase distributions in the plate. In our application the plate is driven close to its natural resonant frequency, and different modes with different amplitudes will be excited. We will particularly look for modes which have the same spatial phase distribution as that of the impressed electric field. When this match is achieved, we will realize a maximum response on the beam pattern of the transducers.



**ELECTRICALLY ISOLATED PLATE  
CONTINUOUS TYPE**

Fig. 2. Electrically isolated plate, continuous type

When the frequency of the travelling wave which possesses the desired spatial phase distribution is found, the reflections from the edge boundary will create a mirror lobe. The creation of the mirror lobe is due to the standing wave that will be formed. The magnitude of the ratio of the travelling wave can be enhanced by applying suitable dissipative damping coupled to the edges of the plate to reduce the reflections that cause a standing wave to be formed.

An active approach which has been used in this thesis is to reduce the reflection of the edge boundary by driving the last few segments out of phase and forcing a reduction in the magnitude of the travelling wave by the time it reaches the boundary.

The approach for a continuous plate also circumvents the necessity of dicing the fragile ceramic disk, and allows one merely to use segmented electrodes.

##### 5. Grating Lobe in Discrete and Continuous Plates

Discrete plates have disadvantages due to the grating lobe, which is an aliasing problem in comparison to the continuous plate. In a discrete plate the bar moves as a whole. The

assumption we could make here is that the displacement across the segment is uniform, so that what we have is a distribution that is spatially quantized, with an accompanying high spatial harmonic content caused by the discontinuities between segments. Because of the coupling in the plate, spatial frequency content of the continuous plate is different in that there are no discontinuities. This reduces the high frequency component and lowers the grating lobe amplitude considerably. The analysis for the grating lobe will be discussed in Chapter II.

#### 6. Phase Quantization

Phase quantization has been used in this investigation in order to generate electrical phase distribution. This quantization was achieved by dividing the phase uniformly between zero and  $2\pi$ . Two, three, and four bit quantization was used in order to evaluate the effect of the quantization on the beam-pattern. This quantization technique will be discussed in Chapter III.

## REFERENCES

1. Lord Rayleigh, Proc. Lond. Math. Soc. 20, 225 (1888-1889)
2. H. Ekstein, Phys. Rev. 68, 11 (1945)
3. H. Lamb, Proc. Roy. Soc. A93, 114 (1917)
4. A. N. Holden, Bell System Tech. J. 30, 956 (1951)
5. R. D. Mindlin, "An Introduction to the Mathematical Theory of Vibrations of Elastic Plates," U. S. Army Signal Corps Eng. Lab., Fort Monmouth, N.J. (1955)
6. M. Onoe, "A Study of the Branches of the Velocity-Dispersion Equations of Elastic Plates and Rods," Rept. Joint Committee on Ultrasonics of the Inst. of Electr. Common. Eng. and the Acoust. Soc. of Japan (1955)
7. I. Tolstoy and E. Usdin, J. Acoust. Soc. Am. 29, 37 91957)
8. E. G. Neuman and R. D. Mindlin, J. Acoust. Soc. Am. 29, 1206 (1957)
9. R. K. Kaul and R. D. Mindlin, J. Acoust. Soc. Am. 34, 1895 (1962)
10. R. K. Kaul and R. D. Mindlin, J. Acoust. Soc. Am. 34, 1902 (1962)

11. H. F. Tiersten, "Thickness Vibrations of Piezoelectric Plates," *J. Acoust. Soc. Am.* 35, 53 (1963)
12. H. F. Tiersten and R. D. Mindlin, "Forced Vibrations of Piezoelectric Crystal Plates," *Quart. Appl. Math.* 20, 107 (1962)
13. J. L. Bleustein and H. F. Tiersten, "Forced Thickness Shear Vibrations of Discontinuously Plated Piezoelectric Plates," *J. Acoust. Soc. Am.* 43, 1311 (1968)

#### OTHER REFERENCES

14. W. P. Mason, *Piezoelectricity, its History and Applications*, *J. Acoust. Soc. Am.* 70(6) (1981)
15. W. P. Mason, *Piezoelectric Crystals and their Applications to Ultrasonics*, D. Van Nostrand Co., New York, 1950
16. H. S. Paul, "Vibrational Waves in a thick Infinite Plate of Piezoelectric crystal," *J. Acoust. Soc. Am.* 44, 478 (1968)
17. S. Kaliski and L Solarz, *Proceedings of Vibration Problems*, 13, 51 (1972)
18. R. K. Kaul and R. D. Mindlin, *J. acoust. Soc. Am.* 34, 1895 (1962)

19. D. V. Schick and H. F. Tiersten, "An Analysis of Thickness Extensional Trapped Energy Mode Transducers," Ultrasonics Symposium, 509 (1982)

CHAPTER II  
THEORETICAL ANALYSIS

## 2.0 INTRODUCTION

The small vibrations of piezoelectric bodies are governed by the equation of the linear theory of piezoelectricity. In piezoelectricity the quasistatic electric field is coupled to the dynamic mechanical motion. To be more specific, the equations of linear elasticity are coupled to the charge equations of electrostatics by means of piezoelectric constants.

Although there are a reasonable number of papers on piezoelectricity currently available [1-2], they have all been investigations from different practical points of view, and use the theory sporadically, without a systematic development. All the existing papers discuss the piezoelectric vibrations of bodies only in the simplest cases of the thickness vibrations and the low-frequency extensional and flexural vibrations of thin rods. In addition, considerations of large piezoelectric coupling are absent in papers on this subject except for discussions of the simplest case of elementary thickness vibrations [3-5].

### 2.1 Dispersion Curve

In this paper, the rigorous solution of the problem of wave propagation in an infinite piezoelectric plate is derived

from the linear piezoelectric equations. The surfaces of the plate are pressure release and completely coated with segmented electrodes. No restriction on the relative magnitude of the elastic, piezoelectric, or dielectric constants is imposed. The solution will be valid for materials with high electromechanical coupling factors. We will consider the piezoelectric plate polarized in the thickness direction. A transcendental frequency equation is derived, the roots of which determine the modes of propagation and the dispersion relations in an unbounded plate.

Figure 1 shows a piezoelectric plate which has been segmented and isolated electrically. A rectangular Cartesian coordinate system  $x_i$ ,  $i=1,..3$  is chosen with  $x_3 = \pm h$  defining the faces of the plate which is poled in the thickness direction. An index preceded by a comma denotes differentiation with respect to a space coordinate.

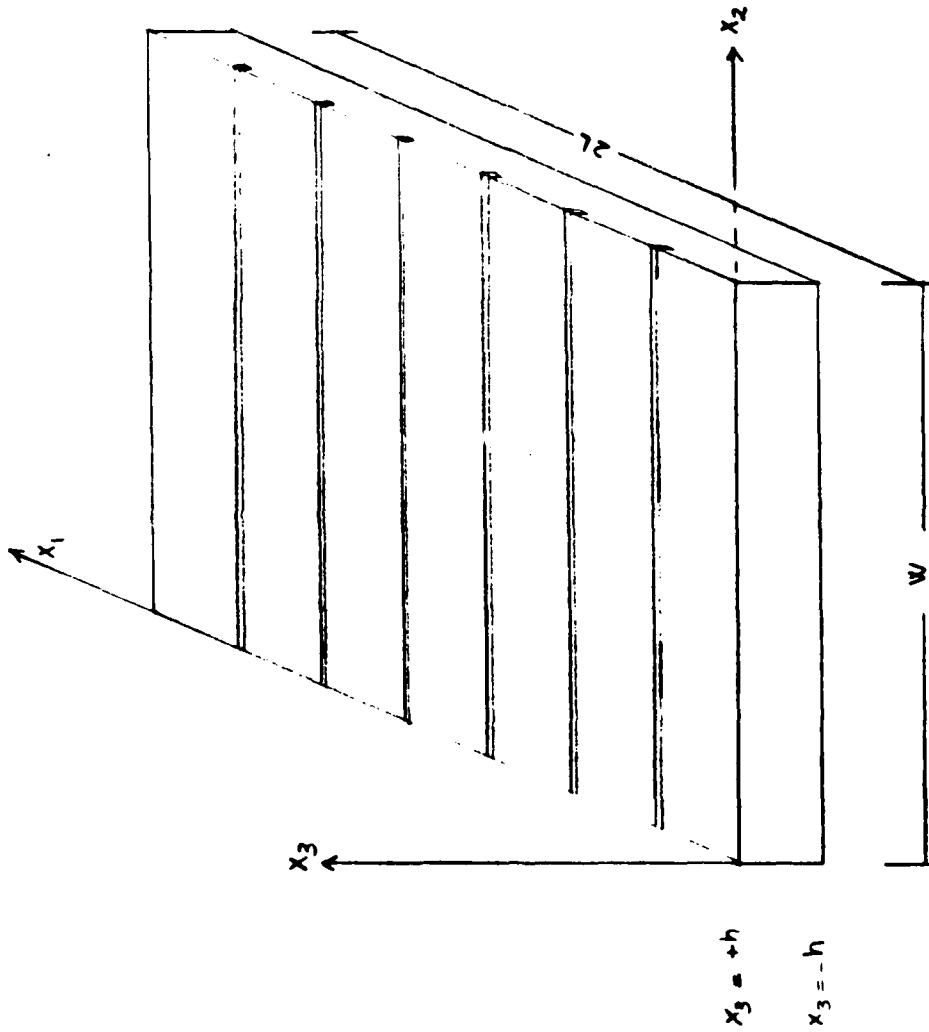


**FIG. 1**  
**ELECTRICALLY ISOLATED PLATE**  
**CONTINUOUS TYPE**

Fig. 1. Coordinate of electrically segmented plate, continuous type

## 2.2 General Equations

The system of equations governing the behavior of this plate consists of the following.

The stress equations of motion [6]:

$$T_{ij,i} = \rho \ddot{u}_j \quad (1)$$

The charge equation of electrostatics:

$$D_{i,i} = 0 \quad (2)$$

The strain-mechanical displacement relations:

$$S_{kl} = \frac{1}{2} (u_{k,l} + u_{l,k}) \quad (3)$$

The electric-field potential relations:

$$E_k = -\psi_{,k} \quad (4)$$

The linear, piezoelectric relations [7-8]:

$$T_{ij} = C_{ijk\ell} S_{k\ell} - e_{kij} E_k \quad (5.1)$$

$$D_i = e_{ik\ell} S_{k\ell} + \epsilon_{ik} E_k \quad (5.2)$$

where, in the above,  $T_{ij}$ ,  $u_j$ ,  $D_i$ ,  $S_{k\ell}$ ,  $E_k$  are the components of stress, mechanical displacement, electric displacement, strain,

and electric field, respectively;  $\rho$  and  $\psi$  are the mass density and the electric potential, respectively;  $C_{ijkl}$ ,  $e_{Kij}$ ,  $\epsilon_{ik}$  are the elastic, piezoelectric, and dielectric constants, respectively.

The face of the infinite plate is immersed in castor oil in a surrounding circular package and tested in water. Since the impedance of the water is much smaller than the impedance of the ceramic, we can ignore the medium loading and basically assume that we have a pressure release boundary. This assumption is not as valid at the resonant frequency of an entitled normal mode.

The faces of the infinite plate are coated with segmented electrodes so it can be steered electrically. Since the electrodes are assumed to be infinitesimally thin, we can ignore all possible mechanical effects.

$$T_{3j} = 0 \text{ at } x_3 = \pm h \quad (6)$$

$$\psi = \text{RE} [e^{i(Kx_1 \sin \theta_0 - \omega t)}] \text{ at } x_3 = \pm h \quad (7)$$

where  $\theta_0$  is the steering angle,  $\omega$  is the frequency of the driving distribution,  $t$  is the time, and  $\psi$  is the driving potential.

For the plate which has been used in this thesis, lead-zirconate, the piezoelectric stress matrix can be written as

$$\epsilon_{ip} = \begin{vmatrix} 0 & 0 & 0 & 0 & 0 & 0 \\ 0 & 0 & 0 & 0 & 0 & 0 \\ e_{31} & e_{31} & e_{33} & 0 & 0 & 0 \end{vmatrix} \quad (8a)$$

$e_{31}$  states that the plate is driven along its thickness direction and the resulting strain is along  $x_1$  direction. Since the material property is the same along the  $x_1, x_2$  direction but is different along the  $x_3$  direction,  $e_{33}$  would be different from both  $e_{31}$  and  $e_{32}$ .

The dielectric matrix can be written as

$$\epsilon_{ij} = \begin{vmatrix} \epsilon_{11} & 0 & 0 \\ 0 & \epsilon_{11} & 0 \\ 0 & 0 & \epsilon_{33} \end{vmatrix} \quad (8b)$$

where again, because of material symmetry along  $x_1, x_2$ ,  $\epsilon_{11}$  and  $\epsilon_{22}$  are the same and  $\epsilon_{33}$  is different.

The elastic constants are:

$$C_{pq} = \begin{vmatrix} C_{11} & C_{12} & C_{13} & 0 & 0 & 0 \\ C_{12} & C_{11} & C_{13} & 0 & 0 & 0 \\ C_{13} & C_{13} & C_{33} & 0 & 0 & 0 \\ 0 & 0 & 0 & C_{44} & 0 & 0 \\ 0 & 0 & 0 & 0 & C_{44} & 0 \\ 0 & 0 & 0 & 0 & 0 & C_{66} \end{vmatrix} \quad (8c)$$

where p or q = 1,2,3,4,5,6 may be replaced by 11,22,33,23 or 32,31, or 13,12 or 21, respectively.

Now within the plate we could write the stress equation of motion as follows:

$$\begin{aligned} \rho \ddot{u}_1 &= \frac{\delta T_{11}}{\delta x_1} + \frac{\delta T_{12}}{\delta x_2} + \frac{\delta T_{13}}{\delta x_3} \\ \rho \ddot{u}_2 &= \frac{\delta T_{21}}{\delta x_1} + \frac{\delta T_{22}}{\delta x_2} + \frac{\delta T_{23}}{\delta x_3} \\ \rho \ddot{u}_3 &= \frac{\delta T_{31}}{\delta x_1} + \frac{\delta T_{32}}{\delta x_2} + \frac{\delta T_{33}}{\delta x_3} \end{aligned} \quad (9)$$

and by Maxwell's electrostatic relation:

$$\nabla \cdot \vec{D} = 0 \quad (10)$$

$$\text{where } \nabla \equiv \left( \frac{\delta}{\delta x_1}, \frac{\delta}{\delta x_2}, \frac{\delta}{\delta x_3} \right) . \quad (11)$$

In a piezoelectric plate the electric flux density can be written as:

$$D_i = e_{ikl} S_{kl} + \epsilon_{ik} E_k \quad (12)$$

Upon substitution of (8), Eq. (5) becomes:

$$T_{11} = c_{11} S_{11} + c_{12} S_{22} + c_{13} S_{33} - e_{31} E_3$$

$$T_{22} = c_{12} S_{11} + c_{11} S_{22} + c_{13} S_{33} - e_{31} E_3$$

$$T_{33} = c_{13} S_{11} + c_{13} S_{22} + c_{33} S_{33} \quad (13)$$

$$T_{23} = c_{44} S_{23}$$

$$T_{13} = c_{44} S_{13}$$

$$T_{12} = c_{66} S_{12}$$

Now by substitution of (3), (4) into (13), Eq. (14) results:

$$T_{11} = C_{11} U_{1,1} + C_{12} U_{2,2} + C_{13} U_{3,3} + e_{31} \psi_{,3}$$

$$T_{22} = C_{12} U_{1,1} + C_{11} U_{2,2} + C_{13} U_{3,3} + e_{31} \psi_{,3}$$

$$T_{33} = C_{13} U_{1,1} + C_{13} U_{2,2} + C_{33} U_{3,3} + e_{33} \psi_{,3}$$

(14)

$$T_{23} = C_{44} (U_{3,2} + U_{2,3})$$

$$T_{13} = C_{44} (U_{3,1} + U_{1,3})$$

$$T_{66} = C_{66} (U_{2,1} + U_{1,2})$$

and Eq. (12) becomes

$$D_1 = -\epsilon_{11} \psi_{,1}$$

$$D_2 = -\epsilon_{11} \psi_{,2} \quad (15)$$

$$D_3 = e_{31} U_{1,1} + e_{31} U_{2,2} + e_{33} U_{3,3} - e_{33} \psi_{,3}$$

Substituting Eqs. (14), (15) into the equations of motion and electrostatic relations of (2), Eq. (17) is achieved:

$$c_{11} u_{1,11} + c_{12} u_{2,21} + c_{13} u_{3,31} + e_{31} \psi_{,31} + c_{66} u_{2,12} \\ + c_{66} u_{1,22} + c_{44} u_{3,13} + c_{44} u_{1,33} = \rho \ddot{u}_1$$

$$c_{66} u_{2,11} + c_{66} u_{1,21} + c_{12} u_{1,12} + c_{11} u_{2,22} + c_{13} u_{3,32} + e_{31} \psi_{,32} \\ + c_{44} u_{3,23} + c_{44} u_{2,33} = \rho \ddot{u}_2$$

(16)

$$c_{44} u_{3,11} + c_{44} u_{1,31} + c_{44} u_{3,22} + c_{44} u_{2,32} + c_{13} u_{1,13} \\ + c_{13} u_{2,23} + c_{33} u_{3,33} + e_{33} \psi_{,33} = \rho \ddot{u}_3$$

and

76

$$-\epsilon_{11} \psi_{,11} - \epsilon_{11} \psi_{,22} + e_{31} u_{1,13} + e_{31} u_{2,23} + e_{33} u_{3,33} - \epsilon_{33} \psi_{,33} = 0 \quad (17)$$

and in our new notation, the boundary condition becomes:

$$T_{33} = T_{32} = T_{31} = 0 \quad \text{at} \quad x_3 = \pm h \quad (18)$$

Since the plate is driven along its length ( $x_1$  direction) we could assume that the mechanical displacement is constant along the  $x_2$  direction.

Since the plate is forced electrically into vibration, the total potential in the plate can be written as:

$$\phi(x_1, x_3, t) = [\psi_H(x_1, x_3) + \psi_{ps}(x_1, x_3)] e^{i\omega t} \quad (19a)$$

$$\text{and} \quad \psi_H = 0 \quad \text{at} \quad x_3 = \pm h \quad (19b)$$

where  $\psi_H$  is the homogeneous steady state solution and  $\psi_{ps}$  is the particular solution due to the applied potential between the two surfaces of the plate.

Now we need to solve the homogeneous solution where

$$\psi_H(x_1, x_3) = 0 \text{ at } x_3 \pm h.$$

$$\rho \ddot{u}_1 = c_{11} u_{1,11} + c_{13} u_{3,13} + e_{31} \psi_{H,31} + c_{44} (u_{3,13} + u_{1,33})$$

$$\rho \ddot{u}_3 = c_{44} u_{3,11} + c_{44} u_{1,31} + c_{13} u_{1,13} + c_{33} u_{3,33} + e_{33} \psi_{H,33} \quad (20)$$

$$- \epsilon_{11} \psi_{H,11} + e_{31} u_{1,13} + e_{33} u_{3,33} - \epsilon_{33} \psi_{H,33} = 0$$

Let's consider a solution of (20) as:

$$u_1 = K_1 \cos P x_3 \sin(L x_1 - \omega t)$$

$$u_3 = K_3 \sin P x_3 \cos(L x_1 - \omega t) \quad (21)$$

$$\psi_H = B \sin P x_3 \cos(L x_1 - \omega t)$$

where  $K_1, K_3, B$  are constants and  $P, L$  are wave number along thickness and propagation direction, respectively. Notice the form of Eq. (21) which is a standing wave along the thickness direction and a travelling wave along the propagation direction.

Eq. (21) satisfies (20) if the following holds:

$$(c_{11}L^2 + c_{44}P^2 - \rho\omega^2)K_1 + (c_{13} + c_{44})LPK_3 + e_{31}LPB = 0$$

$$(c_{44} + c_{13})LPK_1 + (c_{44}L^2 + c_{33}P^2 - \rho\omega^2)K_3 + e_{33}P^2B = 0 \quad (22)$$

$$e_{31}LPK_1 + e_{33}P^2K_3 - (\epsilon_{11}L^2 + \epsilon_{33}P^2)B = 0$$

This system of linear, homogeneous equations in  $K_1$ ,  $K_3$ ,  $B$  yields nontrivial solutions when the determinant of the coefficients of  $K_1$ ,  $K_3$ ,  $B$  vanishes; i.e., when

$$\begin{vmatrix} (c_{11}L^2 + c_{44}P^2 - \rho\omega^2) & (c_{13} + c_{44})LP & e_{31}LP \\ (c_{44} + c_{13})LP & (c_{44}L^2 + c_{33}P^2 - \rho\omega^2) & e_{33}P^2 \\ e_{31}LP & e_{33}P^2 & -(\epsilon_{11}L^2 + \epsilon_{33}P^2) \end{vmatrix} = 0 \quad (23)$$

Eq. (23) is quadratic in  $\omega^2$ , but cubic in  $L^2, P^2$ . Therefore, for a given  $\omega$  and a propagation wavenumber  $L$ , there are three thickness wavenumbers ( $P^{(1)}$ ,  $P^{(2)}$ ,  $P^{(3)}$ ), each of which yields an independent solution and amplitude ratios when substituted in (22). The amplitude ratios will be designated by

$$(k_1^{(i)} : k_3^{(i)} : b^{(i)}) = (\beta_1^{(i)} : \beta_3^{(i)} : \beta_2^{(i)}) \quad (24a)$$

where

$$\beta_1^{(i)} = [(c_{11}L^2 + c_{44}p(i)^2 - \rho\omega^2) * (c_{44}L^2 + c_{33}p(i)^2 - \rho\omega^2)] - [e_{33}p(i)^2 * e_{33}p(i)^2]$$

$$\beta_2^{(i)} = [e_{31}Lp(i) * (c_{44}L^2 + c_{33}p(i)^2 - \rho\omega^2)] - [(c_{44} + c_{13})Lp(i) * e_{33}p(i)^2]$$

$$\beta_3^{(i)} = [e_{33}p(i)^2 * e_{31}Lp(i)] + [(c_{44} + c_{13})Lp(i) * (e_{11}L^2 + e_{33}p(i)^2)]$$

Eq. (23) clearly shows that the piezoelectric constants  $e_{ip}$  couple the quasistatic electric solution of (17) to the dynamic mechanical motion of (20). These two solutions uncouple only if all the  $e_{ip}$  vanish. This coupling of a quasistatic phenomenon to a dynamic phenomenon states that a given frequency and propagation wavenumber result in three thickness wavenumbers.

One solution of the differential equation is insufficient to satisfy the boundary conditions; all three solutions are required. Hence, we must take:

$$\begin{aligned}
 u_1 &= \sin(Lx_1 - \omega t) + \sum_{i=1}^3 A(i) \beta_1(i) \cos p(i) x_3 \\
 u_3 &= \cos(Lx_1 - \omega t) \sum_{i=1}^3 A(i) \beta_3(i) \sin p(i) x_3 \\
 \psi &= \cos(Lx_1 - \omega t) \sum_{i=1}^3 A(i) \beta_2(i) \sin p(i) x_3
 \end{aligned} \tag{25}$$

as solutions of the problem.

Now we need also to consider the boundary condition in order to solve the problem completely. Substituting from (25) into the boundary conditions (18), (19b), and using the required relations in (14), (15), one obtains:

$$\begin{aligned}
 T_{33} &= c_{13} u_{1,1} + c_{33} u_{3,3} + e_{33} \psi_{,3} = 0 \\
 T_{13} &= c_{44} (u_{3,1} + u_{1,3}) = 0 \quad \text{at } x_3 = \pm h \\
 T_{23} &= c_{44} (u_{3,2} + u_{2,3}) = 0 \\
 \psi_H &= 0
 \end{aligned} \tag{26}$$

and from Eq. (26), Eq. (27) is achieved:

$$\sum_{i=1}^3 A^{(i)} T_1^{(i)} \sin p^{(i)} h = 0$$

$$\sum_{i=1}^3 A^{(i)} T_2^{(i)} \cos p^{(i)} h = 0 \quad (27)$$

$$\sum_{i=1}^3 A^{(i)} \beta_2^{(i)} \sin p^{(i)} h = 0$$

where

$$T_1^{(i)} = c_{44} (\beta_3^{(i)} L + \beta_1^{(i)} p^{(i)}) \quad (28)$$

$$T_2^{(i)} = c_{13} \beta_1^{(i)} L + c_{33} \beta_3^{(i)} p^{(i)} + e_{33} \beta_2^{(i)} p^{(i)}$$

Eq. (27) consists of a system of linear, homogeneous algebraic equations in the  $A^{(i)}$ . This system yields a non-trivial solution when the determinant of the coefficients of the  $A^{(i)}$  vanishes;

i.e., when

$$D(L, \omega) = \begin{vmatrix} T_1^{(1)} \sin p^{(1)} h & T_1^{(2)} \sin p^{(2)} h & T_1^{(3)} \sin p^{(3)} h \\ T_2^{(1)} \cos p^{(1)} h & T_2^{(2)} \cos p^{(2)} h & T_2^{(3)} \cos p^{(3)} h \\ \beta_2^{(1)} \sin p^{(1)} h & \beta_2^{(2)} \sin p^{(2)} h & \beta_2^{(3)} \sin p^{(3)} h \end{vmatrix} = 0 \quad (29)$$

Eq. (29) is a transcendental equation, the roots of which enable the determination of the dispersion relation for this piezoelectric plate. Eq. (29) contains an infinite number of roots  $h_n$ , each of which determines a point on the dispersion spectrum and yields amplitude ratios  $(A^{(1)} : A^{(2)} : A^{(3)})$  when substituted in (27).

Now for the purpose of calculating the dispersion curve, it is convenient to write the pertinent equations involved in the calculation in terms of certain dimensionless quantities. The pertinent equations are (22), (23), (27), (28), and (29). Let's assume:

$$\begin{aligned}
 \eta &= \frac{2Lh}{\pi} & \alpha &= \frac{2Ph}{\pi} \\
 \bar{c}_{pq} &= \frac{c_{pq}}{c_{44}} & \bar{e}_{ip} &= \frac{e_{ip}}{(c_{44}\epsilon_{33})^{1/2}} & \bar{\epsilon} &= \frac{\epsilon_{ij}}{\epsilon_{33}} & (30) \\
 \Omega &= \frac{\omega}{\epsilon} & \bar{\omega} &= \left(\frac{\pi}{2h}\right) \left(\frac{c_{44}}{P}\right)^{1/2} & \bar{B} &= B \left(\frac{\epsilon_{33}}{c_{44}}\right)^{1/2}
 \end{aligned}$$

Now the pertinent equations become

$$\begin{aligned}
 & (\bar{c}_{11}\eta^2 + \bar{c}_{44}\alpha^2 - \Omega^2)K_1 + (\bar{c}_{13} + \bar{c}_{44})\alpha\eta K_3 + \bar{e}_{31}\eta\alpha \bar{B} = 0 \\
 & (\bar{c}_{44} + \bar{c}_{13})\alpha\eta K_1 + (\bar{c}_{44}\eta^2 + \bar{c}_{33}\alpha^2 - \Omega^2)K_3 + \bar{e}_{33}\alpha^2 \bar{B} = 0 \\
 & \bar{e}_{31}\eta\alpha K_1 + \bar{e}_{33}\alpha^2 K_3 - (\bar{c}_{11}\eta^2 + \bar{c}_{33}\alpha^2) \bar{B} = 0
 \end{aligned} \tag{31}$$

and

$$\begin{vmatrix}
 (\bar{c}_{11}\eta^2 + \bar{c}_{44}\alpha^2 - \Omega^2) & (\bar{c}_{13} + \bar{c}_{44})\eta\alpha & \bar{e}_{31}\alpha\eta \\
 (\bar{c}_{44} + \bar{c}_{13})\alpha\eta & (\bar{c}_{44}\eta^2 + \bar{c}_{33}\alpha^2 - \Omega^2) & \bar{e}_{33}\alpha^2 \\
 \bar{e}_{31}\alpha\eta & \bar{e}_{33}\alpha^2 & -(\bar{c}_{11}\eta^2 + \bar{c}_{33}\alpha^2)
 \end{vmatrix} = 0 \tag{32}$$

$$\sum_{i=1}^3 A(i) T_1(i) \sin \frac{\pi}{2} \alpha(i) = 0$$

$$\sum_{i=1}^3 A(i) T_2(i) \cos \frac{\pi}{2} \alpha(i) = 0 \tag{33}$$

$$\sum_{i=1}^3 A(i) \bar{\beta}_2(i) \sin \frac{\pi}{2} \alpha(i) = 0$$

where

$$\bar{T}_1^{(i)} = \bar{c}_{44} (\beta_3^{(i)} n + \beta_1^{(i)} \alpha^{(i)}) \quad (34)$$

$$\bar{T}_2^{(i)} = \bar{c}_{13} \beta_1^{(i)} n + \bar{c}_{33} \beta_3^{(i)} \alpha^{(i)} + \bar{e}_{33} \bar{\beta}_2^{(i)} \alpha^{(i)}$$

and finally, from the determinant of (33)

$$x^{(1)} \cot \frac{\pi}{2} \alpha^{(1)} + x^{(2)} \cot \frac{\pi}{2} \alpha^{(2)} + x^{(3)} \cot \frac{\pi}{2} \alpha^{(3)} = 0 \quad (35)$$

where

$$\begin{aligned} x^{(1)} &= \bar{T}_2^{(1)} (\bar{T}_1^{(3)} \beta_2^{(2)} - \bar{T}_1^{(2)} \bar{\beta}_2^{(3)}) \\ x^{(2)} &= \bar{T}_2^{(2)} (\bar{T}_1^{(1)} \bar{\beta}_2^{(3)} - \bar{T}_1^{(3)} \bar{\beta}_2^{(1)}) \quad (36) \\ x^{(3)} &= \bar{T}_2^{(3)} (\bar{T}_1^{(2)} \bar{\beta}_2^{(1)} - \bar{T}_1^{(1)} \bar{\beta}_2^{(2)}) \end{aligned}$$

The relations between  $\Omega$  and  $n$ , (i.e., the dispersion relation), can now be evaluated. Several methods of obtaining the roots of the transcendental equation have been suggested by

several authors [9-10]. But a very simple, straightforward procedure for calculating the dispersion relation is by selecting a value of  $n$ . The further choice of  $\Omega$  permits the calculation of the  $\alpha^{(i)}$  from (32) and the  $\bar{\beta}_j^{(i)}$  from (31) so that the  $\bar{T}_1^{(i)}$  and  $\bar{T}_2^{(i)}$  may be computed from (34). The  $x^{(i)}$  may now be determined from (36). If the values thus determined satisfy Eq. (35), the selected values of  $n$  and  $\Omega$  constitute a point on the dispersion curve. If Eq. (35) is not satisfied, we repeat the calculation for different values of  $n$  and  $\Omega$  until Eq. (35) is satisfied and a root has been obtained. When a sufficient number of values of  $n$  and  $\Omega$  satisfying Eq. (35) has been obtained, the dispersion curve can be plotted.

The starting point on the dispersion point is critical in determination of the dispersion curve. The solution at an infinite wavelength can be obtained simply by setting  $L = 0$ . However, the procedure is not quite as straightforward. When  $L$  is set to 0, Eqs. (22) and (23) becomes, respectively,

$$\begin{aligned} (c_{44}p^2 - \rho\omega^2) K_1 &= 0 \\ (c_{33}p^2 - \rho\omega^2) K_3 + \epsilon_{33}p^2 B &= 0 \\ \epsilon_{33}p^2 K_3 - \epsilon_{33}p^2 B &= 0 \end{aligned} \quad (37)$$

and

$$\begin{vmatrix} (c_{44}p^2 - \rho\omega^2) & 0 & 0 \\ 0 & c_{33}p^2 - \rho\omega^2 & 0 \\ 0 & e_{33}p^2 & -e_{33}p^2 \end{vmatrix} = 0 \quad (38)$$

From Eq. (38), the three  $p^{(i)}$  are given by

$$(p^{(1)}, p^{(2)}, p^{(3)}) = [\omega(\rho/c_{44})^{1/2}, 0, \omega(\rho/\bar{c}_{33})^{1/2}] \quad (39)$$

where  $\bar{c}_{33} = c_{33} + \bar{e}_{33}^2/\epsilon_{33}$ . The substitution of the three  $p^{(i)}$  successively into the algebraic equation of (37) yields

$$(\beta_1^{(i)}, \beta_3^{(i)}, \bar{\beta}_2^{(i)}).$$

Eq. (27) now becomes:

$$A^{(1)} c_{44} p^{(1)} \sin p^{(1)} h = 0$$

$$A^{(2)} e_{33} p^{(2)} \cos p^{(2)} h + A^{(3)} (c_{33} + e_{33}^2/\epsilon_{33}) p^{(3)} \cos p^{(3)} h = 0 \quad (40)$$

$$A^{(2)} \sin p^{(2)} h + A^{(3)} (e_{33}/\epsilon_{33}) \sin p^{(3)} h = 0$$

The last two equations (39,40) show that as  $p^{(2)} \rightarrow 0$ ,  $c^{(2)} \rightarrow \infty$  since  $\sin p^{(3)}h$  and  $\cos p^{(3)}h$  cannot equal zero simultaneously. However,  $A^{(2)}$  and  $p^{(2)}$  always occur as an indeterminate product. Hence, Eq. (40) may be written as:

$$A^{(1)} c_{44} p^{(1)} \sin p^{(1)}h = 0$$

$$K e_{33} + A^{(3)} \bar{c}_{33} p^{(3)} \cos p^{(3)}h = 0 \quad (41)$$

$$Kh + A^{(3)} (e_{33}/\bar{c}_{33}) \sin p^{(3)}h = 0$$

where  $K \equiv A^{(2)}p^{(2)}$ . Eq. (40) yields a nontrivial solution when

$$\begin{vmatrix} c_{44} p^{(1)} \sin p^{(1)}h & 0 & 0 \\ 0 & e_{33} & \bar{c}_{33} p^{(3)} \cos p^{(3)}h \\ 0 & h & (e_{33}/\bar{c}_{33}) \sin p^{(3)}h \end{vmatrix} = 0 \quad (42)$$

holds.

Eq. (42) yields two transcendental equations, each of which determines a set of roots. The two equations may be written as:

$$\sin p^{(1)}h = 0, \tan p^{(3)}h = p^{(3)}h/K_t^2 \quad (43)$$

$$\text{where } K_t = (e_{33}^2 / \epsilon_{33} \bar{c}_{33})$$

Thus we see that the first transcendental equation yields thickness frequencies and modes which are identical with the purely elastic modes. We also see that the second transcendental equation yields thickness frequencies and modes with piezoelectric coupling. Thus for this piezoelectric plate the wavelengths of overtone resonances are not integral fractions of the fundamental; as a consequence the resonant frequencies of overtone modes are not integral multiples of the fundamental. The deviation from the integral multiple relationship depends on the electromechanical coupling factor  $K_t$  only.

The analytical approach that has just been described here was done on the piezoelectric plate (lead-zirconate) and the dispersion curve was evaluated. Figure 2 shows the dispersion curve for such a plate. The abscissa is the normalized (dimensionless) wavenumber and the ordinate is the normalized (dimensionless) frequency.

FIG. 2

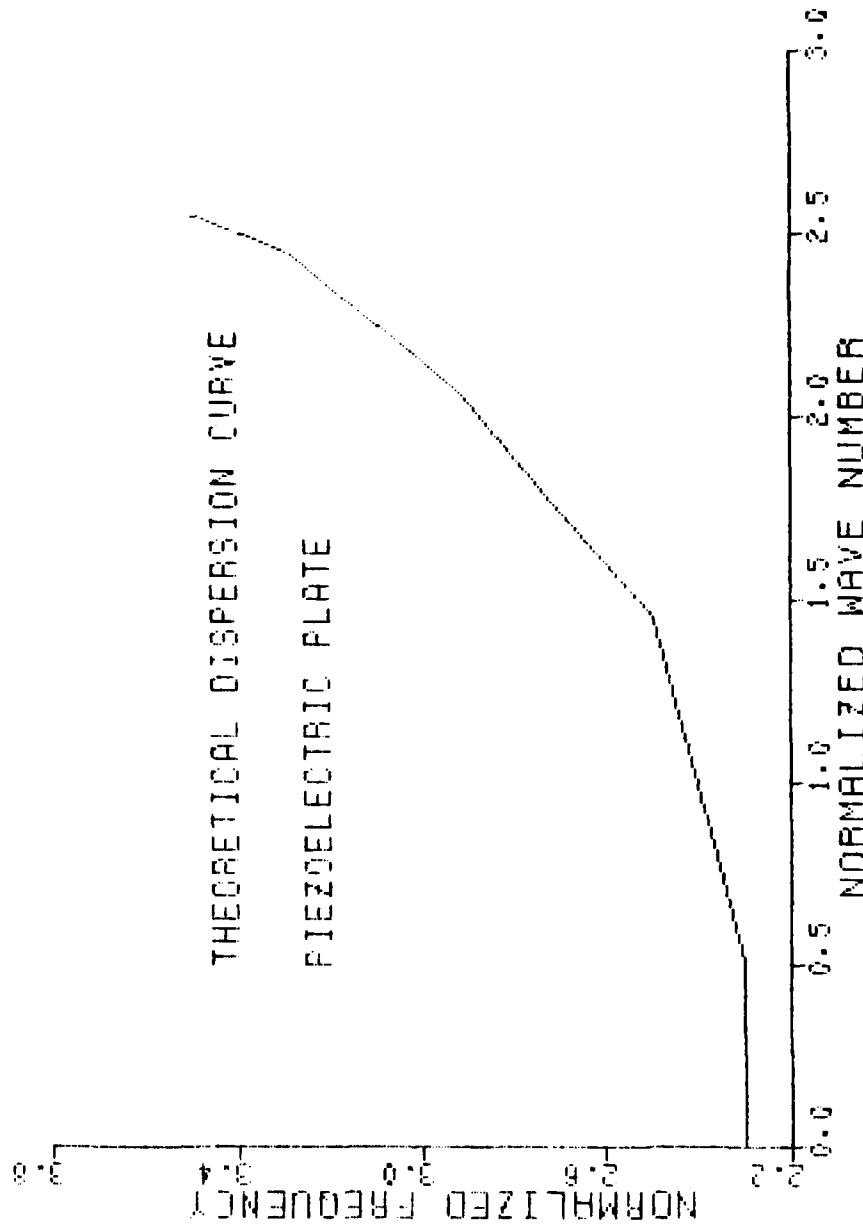


Fig. 2. Theoretical dispersion curve (normalized wavenumber vs. normalized frequency).

### 2.3 Electrical Steering

The evaluation of the dispersion curve (frequency vs. wavenumber) can now be matched to the wavenumber of the driving distribution so the beam can be steered electrically.

By Snell's Law:

$$K_0 \sin\theta_0 = K_p(\omega) \quad (44)$$

where  $K_0 = \frac{\omega}{C_w}$ ,  $C_w$  is the speed of sound in the water,  $\omega$  is the angular frequency, and  $\theta_0$  is the steering angle. By solving (44) the corresponding frequency vs. the steering angle for such a plate can now be calculated from

$$K_0 \sin\theta_0 - K_p(\omega) = 0 \quad (45)$$

Figure 3 shows the theoretical curve for such a plate which has been polarized along its thickness direction. The shape of the curve is similar to the dispersion curve of Figure 2. The abscissa is the steering angle in degrees and the ordinate, the frequency in KHZ.

THEORETICAL DISPERSION CURVE  
ANGLE 4.5 FREQUENCY  
RESONANT FREQ=325 KHZ

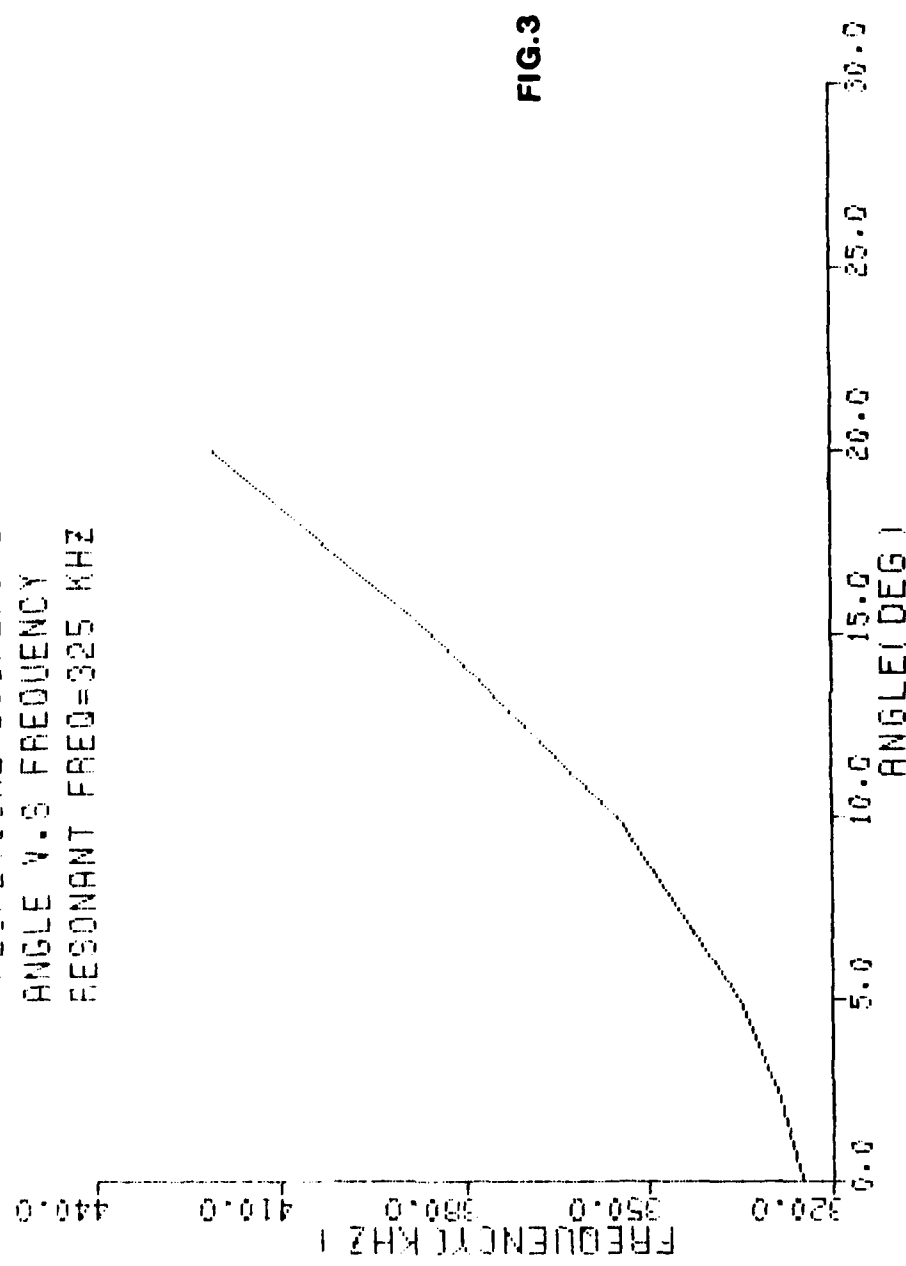


Fig. 3. Theoretical dispersion curve (steering angle vs. frequency).

#### 2.4 Grating Lobe in a Discrete and Continuous Plate

For an electrically segmented and acoustically isolated plate the acoustic amplitude distribution of the plate is uniform since the segments move as a whole. The assumption we could make here is that what we have is a spatially quantized amplitude distribution, with accompanying spatial harmonic content caused by the discontinuities between segments.

Figure 4 shows a discrete linear, equally spaced array in which the beam pattern function can be derived as:

$$V = \sum_m R_m \cos(\omega t + mu) \quad (46)$$

where  $R_m$  is the individual voltage of each array:

$$V = [R_0 + R_1 e^{iu} + \dots + R_{me} e^{imu} + R_{n-1} e^{(n-1)iu}]$$

where  $u = KD \sin\theta$  (47)

$\theta$  = physical angle

D = spacing between the elements

K = wavenumber

..... THEORETICAL AMPLITUDE DISTRIBUTION . . .

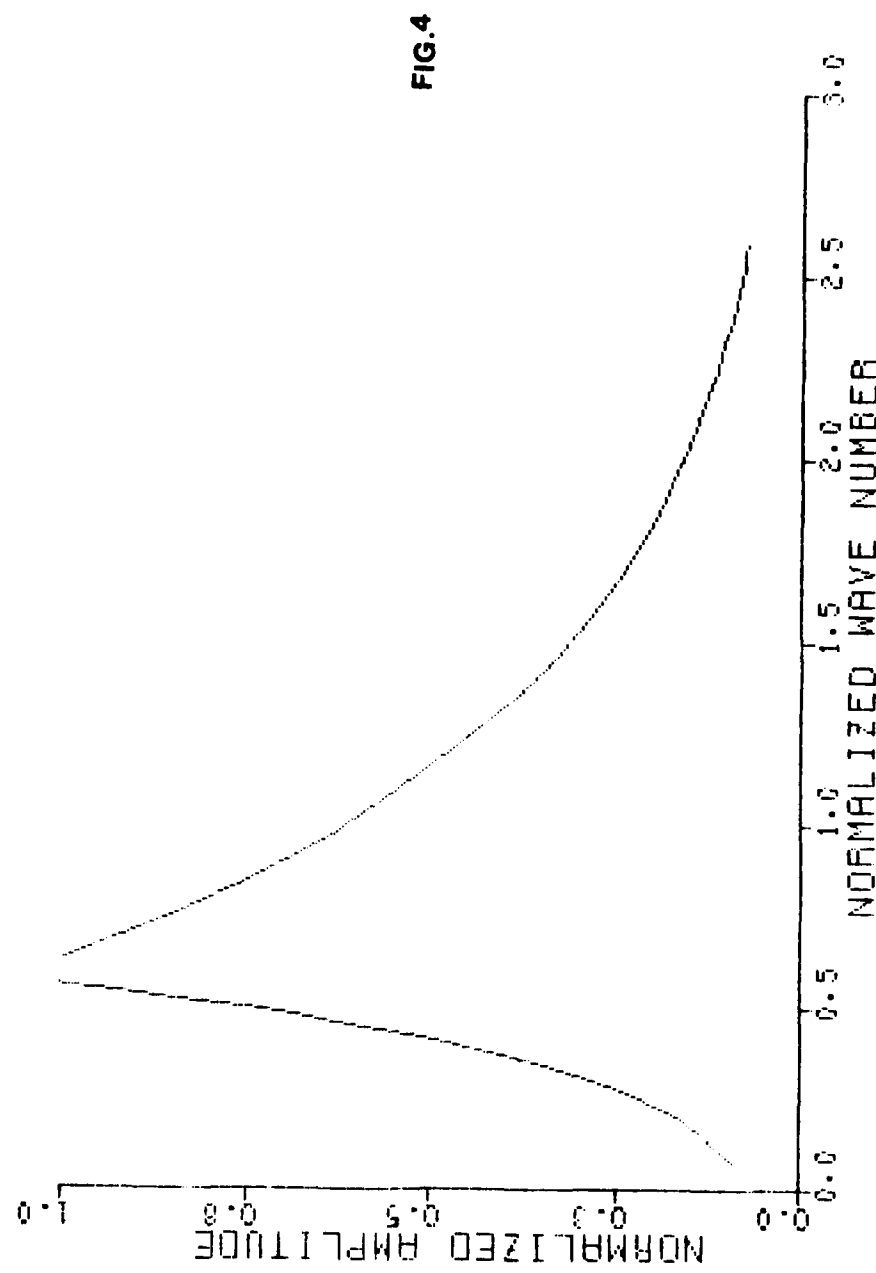


Fig. 4. Theoretical spatial filtering function.

Multiplying (47) by  $e^{iu}$  and subtracting from (47) results in:

$$V = \left( \frac{e^{inu} - 1}{e^{iu} - 1} \right) = \frac{\sin(nu/2)}{\sin(u/2)} \quad (48a)$$

Now the beam pattern  $V$  must be multiplied by the directivity of each individual element. That is,

$$V = \frac{\sin(nU/2)}{\sin(U/2)} * \frac{\sin(U/2)}{(U/2)} \quad (48b)$$

where the second term in (48) is the directivity of each elements.

Here if the beam is steered off normal [11-14]

$$u = KD(\sin\theta - \sin\theta_0) \quad (48c)$$

For the discrete segmented plate, if the path difference between the segments reaches  $2\pi$ , the pattern repeats itself; that is,

$$KD(\sin\theta - \sin\theta_0) = 2n\pi \quad n = (0, 1, 2, \dots) \quad (48d)$$

so there exists some spatial harmonic content of the resonant wavenumber that gives rise to the grating lobe in a discrete plate.

For the continuous plate, the segments' motion is different than the one for an acoustically isolated plate, since there are no discontinuities in the acoustic amplitude distribution because of the coupling in the continuous plate. This amplitude distribution has a lower spatial harmonic content which reduces the grating lobe considerably when the beam is steered off normal. The plate in effect spatially filters the high harmonic that is associated with the electric field.

This spatial filtering effect can now be derived theoretically as a function of a normalized wavenumber in the plate.

From (19)

$$\phi(x_1, x_3, t) = [\psi_H(x_1, x_3) + \psi_{PS}(x_1, x_3)] e^{i\omega t}$$

We have already solved the homogeneous solution of the problem when the dispersion curve was derived. Now we need to find the particular solution due to the applied electric field. From the particular solution we obtain the acoustic amplitude distribution as a function of the wavenumber in the plate for a fixed frequency.

Since the plate is driven externally with potential of Eq. (7) at the faces of the plate, there will be a corresponding stress and electric field due to the applied drive. Eq. (5.1) and (5.2) can now be written as:

$$T_{ij,i} = \rho \ddot{u}_j \quad (49a)$$

$$D_{i,i} + D_{i,i}^e = 0$$

where  $T_{ij}$ ,  $u_j$ ,  $D_i$  are the components of stress, mechanical displacement, and electric displacement, respectively. The quantities  $D_i^e$  represent the electrical term due to the applied potential. The associated boundary conditions for a pressure release boundary with zero-normal component of electric displacement is given by:

$$N_i(T_{ij}) = 0 \quad (49b)$$

$$N_i(D_i + D_i^e) = 0$$

The previously derived homogeneous solution yielded the functions  $(u_1^m, u_3^m, \psi^m)$ , which satisfy the equation of motion (49a) and boundary conditions (49b). Now, if we assume that the

solution due to the applied field is  $(u_1, u_3, \psi)$ , these functions must also satisfy (49a).

Now let's multiply (49a) by  $U_j^m$  once and then by  $U_j$  and subtract and integrate over the volume:

$$\int_V [(T_{ij,i}^m + \rho \omega_m^2 U_j^m) U_j - (T_{ij,i} + \rho \omega^2 U_j) U_j^m] dV = 0 \quad (50)$$

Now by the divergence theorem:

$$(\omega_m^2 - \omega^2) \int_V \rho U_j^m U_j dV = \int_S N_i [T_{ij} U_j^m - T_{ij}^m U_j + D_i \psi^m - D_i^m \psi] dS \quad (51)$$

Since the homogeneous solution yielded zero-normal component of stress, mechanical displacement and electrical displacement at the boundary, Eq. (51) can be rewritten as:

$$(\omega_m^2 - \omega^2) \int_V \rho U_j^m U_j dV = \int_S N_i (D_i^m \psi) dS \quad (52)$$

Now we can write

$$U_m = \sum_m \frac{g_m}{(\omega_m^2 - \omega^2)} \int N_i (D_i^m \psi) dS \quad (53)$$

where

$$g_m = \frac{U_j^m}{N} , \quad N = \int_V \rho U_j^m U_j dV \quad (54)$$

Eq. (53) shows that at  $\omega = \omega_m$  the displacement function goes to infinity, and this is usually the case for the driven plate if there is no damping in the plate. Now the displacement and potential function due to the applied field is required, so first we expand the solutions of the problem in Fourier sine and cosine series:

$$\begin{aligned} U_1 &= \sum_{n=1}^{\infty} U_n(x_3) \sin(L_n x_1) \\ U_3 &= \sum_{n=1}^{\infty} V_n(x_3) \cos(L_n x_1) \\ \psi_{ps} &= \sum_{n=1}^{\infty} B_n(x_3) \cos(L_n x_1) \end{aligned} \quad (55)$$

where  $U_1, U_3$  are the displacements along  $x_1, x_3$ , respectively,  $\psi_{ps}$  is the particular solution due to the applied

electric fields,  $U_n(x_3)$ ,  $V_n(x_3)$ ,  $B_n(x_3)$  are acoustic amplitude distributions in the plate, and  $L_n$  are the discrete eigenvalues of the wavenumber.

Substitution of (55) into the linear piezoelectric equations of (5.1), (5.2) gives

$$K_1 U(x_3) + (K_2 + K_4) V_{,3} + K_3 B_{,3} + K_5 V_{,33} = 0 \quad (56a)$$

$$L_1 V(x_3) - (L_2 + K_4) U_{,3} + L_2 V_{,33} + L_3 B_{,33} = 0 \quad (56b)$$

$$M_1 B(x_3) - K_3 U_{,3} + L_3 V_{,33} + M_2 B_{,33} = 0 \quad (56c)$$

where

$$K_1 = -\bar{C}_{11} L_n^2 \quad K_2 = -\bar{C}_{13} L_n \quad K_3 = -\bar{e}_{31} L_n \quad K_4 = -\bar{C}_{44} L_n \quad K_5 = \bar{C}_{44}$$

$$L_1 = -\bar{C}_{44} L_n^2 \quad L_2 = \bar{C}_{33} \quad L_3 = \bar{e}_{33}$$

$$M_1 = \bar{C}_{11} L_n^2 \quad M_2 = -\bar{e}_{33}$$

(57)

The sets of equations in (55) constitute the solution for the forced vibration problem considered here.

Now multiply (56b) by  $-K_3$  and (56c) by  $(K_2+K_4)$  and add:

$$V_{,33} = \left(\frac{x_2}{x_1}\right) V + \left(\frac{x_3}{x_1}\right) B_{,33} - \left(\frac{x_4}{x_1}\right) B \quad (58)$$

where

$$x_1 = L_3 (K_2 + K_4) - K_3 L_2$$

$$x_2 = K_3 L_1$$

$$x_3 = K_3 L_3 - M_2 (K_2 + K_4)$$

$$x_4 = M_1 (K_2 + K_4) \quad (59)$$

Now taking the derivative of the (56a) with respect to the  $x_3$  coordinate and multiplying it by  $(K_2+K_4)$ , and (56b) by  $K_1$ , and adding:

$$K_1 U_{,1} + (K_2 + K_4) V_{,33} + K_3 B_{,33} + K_5 U_{,333} = 0$$

$$L_1 V - (K_2 + K_4) U_{,3} + L_2 V_{,33} + L_3 B_{,33} = 0$$

which results in

$$V_{,33}Y_1 + VY_2 + B_{,33}Y_3 + U_{,333}Y_4 = 0 \quad (60)$$

where

$$Y_1 = (K_2 + K_4)^2 + K_1 L_2$$

$$Y_2 = L_1 K_1$$

$$Y_3 = K_3 (K_2 + K_4) + K_1 L_3$$

$$Y_4 = K_5 (K_2 + K_4) \quad (61)$$

Also from (56c), let's take the double derivative with respect to  $x_3$  coordinate:

$$U_{,333} = \frac{M_1}{K_3} B_{,33} + \frac{L_3}{K_3} V_{,3333} + \frac{M_2}{K_3} B_{,3333} \quad (62)$$

Substitution back into the equation of (60):

$$\begin{aligned}
 & V_{,3333} \left( \frac{L_3}{K_3} \right) + V_{,33} Y_1 + VY_2 + B_{,33} \left( Y_3 + Y_4 \left( \frac{M_1}{K_3} \right) \right) \\
 & + B_{,3333} \left( Y_4 \left( \frac{M_2}{K_3} \right) \right) = 0
 \end{aligned} \tag{63}$$

Now let's take the double derivative of (58) and substitute back into (58):

$$V_{,3333} = \frac{x_3}{x_1} B_{,3333} + \left( \frac{x_2 x_3}{x_1^2} - \frac{x_4}{x_1} \right) B_{,33} + \left( \frac{x_2 x_4}{x_1^2} \right) B + \left( \frac{x_2}{x_1} \right)^2 V \tag{64}$$

By substituting (64) into (63), Eq. (65) results:

$$\begin{aligned}
 & \left( \frac{L_3 x_3}{K_3 x_1} + \frac{M_2}{K_3} \right) B_{,3333} + \left[ \frac{x_2 x_3}{x_1} - \frac{x_4}{x_1} + \frac{x_3}{x_1} ((K_2 + K_4)^2 + K_1 L_2) \right. \\
 & \left. + (K_3 (K_2 + K_4) + K_1 L_3) \right] B_{,33} + \left[ \frac{x_2 x_4}{x_1^2} - \frac{x_4}{x_1} ((K_2 + K_4)^2 + K_1 L_2) \right] B \\
 & + \left[ \left( \frac{x_2}{x_1} \right)^2 - \frac{x_2}{x_1} ((K_2 + K_4)^2 + K_1 L_2) + K_1 L_1 \right] V = 0
 \end{aligned} \tag{65}$$

in which  $V$  can now be defined as a function of  $B$ :

$$v = \left(\frac{z_1}{z_4}\right) B_{3333} + \left(\frac{z_2}{z_4}\right) B_{33} + \left(\frac{z_3}{z_4}\right) B \quad (66)$$

where

$$z_1 = \frac{L_3 x_3}{K_3 x_1} + \frac{M_2}{K_3}$$

$$z_2 = \frac{x_2 x_3}{x_1^2} - \frac{x_4}{x_1} + \frac{x_3}{x_1} ((K_2 + K_4)^2 + K_1 L_2) + (K_3 (K_2 + K_4) + K_1 L_3)$$

$$z_3 = \frac{x_2 x_4}{x_1^2} - \frac{x_4}{x_1} ((K_2 + K_4)^2 + K_1 L_2)$$

$$z_4 = \frac{x_2}{x_1} ((K_2 + K_4)^2 + K_1 L_2) - K_1 L_1 - \left(\frac{x_2}{x_1}\right)^2 \quad (67)$$

Now by substituting (66) back into (58):

$$M_1 B_n^{(VI)}(x_3) + M_2 B_n^{(IV)}(x_3) + M_3 B_n^{(II)}(x_3) + M_4 B_n(x_3) = 0 \quad (68)$$

where

$$M_1 = \frac{(-(\bar{c}_{13} L_n + L_n) + \bar{e}_{31} L_n \bar{c}_{33}) [(-\bar{e}_{31} L_n - \bar{e}_{33} (\bar{c}_{13} L_n + L_n) + \bar{e}_{33} (\bar{c}_{13} L_n + L_n) + \bar{e}_{31} L_n \bar{c}_{33})]}{-(\bar{e}_{31} L_n)^2 L_n^2 [(\bar{e}_{31} L_n^3)^3 - \bar{c}_{11} L_n^4 - ((\bar{c}_{13} L_n + L_n)^2 - \bar{c}_{11} L_n^2 \bar{c}_{33})]}$$

$$\begin{aligned}
& \frac{\bar{e}_{31} L_n^3 (+\bar{e}_{31} L_n + \bar{\epsilon}_{33} (\bar{c}_{13} L_n - L_n))}{(\bar{c}_{13} L_n + L_n) - \bar{e}_{13} L_n \bar{c}_{33}} - \epsilon_{11} L_n^2 (-\bar{e}_{13} L_n - L_n) \\
& + [-\bar{e}_{31} L_n + \bar{\epsilon}_{33} (-\bar{c}_{13} L_n - L_n)] * [((\bar{c}_{13} L_n - L_n)^2 - c_{11} L_n^2 c_{33}) \\
& - \bar{e}_{31} L_n (-\bar{c}_{13} L_n - L_n) - \bar{c}_{11} L_n^2] - \bar{e}_{31} L_n^3 \left[ \frac{-1}{\bar{e}_{31} L_n} * \right. \\
& \left. \left( \frac{-\bar{e}_{31} L_n + \bar{\epsilon}_{33} (-\bar{c}_{13} L_n - L_n)}{(-\bar{c}_{13} L_n - L_n) - \bar{e}_{31} L_n^2 \bar{c}_{13}} \right) + \frac{\bar{\epsilon}_{33}}{\bar{e}_{31} L_n} \right] \\
M_2 = & \frac{\bar{e}_{31} L_n^3}{\frac{-\bar{e}_{31} L_n^3}{(\bar{c}_{13} L_n + L_n) + \bar{e}_{31} L_n \bar{c}_{33}} [((-\bar{c}_{13} L_n - L_n)^2 - c_{11} L_n^2 \bar{c}_{33}) - \bar{c}_{11} L_n^4 + \left( \frac{\bar{e}_{31} L_n^3}{(c_{13} L_n + L_n) - \bar{e}_{31} L_n \bar{c}_{33}} \right)]}
\end{aligned}$$

$$\frac{+\bar{e}_{31}L_n^5 \bar{\epsilon}_{11}(\bar{c}_{13}L_n + L_n)}{\bar{e}_{33}(\bar{c}_{13}L_n + L_n) + \bar{e}_{31}L_n\bar{c}_{33}} - \bar{\epsilon}_{11}L_n^2((-\bar{c}_{13}L_n - L_n)^3 - \bar{c}_{11}L_n^2\bar{c}_{33})$$

$$M_3 = \frac{-(\bar{e}_{31}L_n + \bar{e}_{33}(-\bar{c}_{13}L_n - L_n))(\bar{e}_{31}L_n^3) - \bar{c}_{11}L_n^4 - \left[ \frac{\bar{e}_{31}L_n^3}{(-\bar{c}_{13}L_n - L_n) + \bar{e}_{31}L_n\bar{c}_{33}} \right]^2}{\frac{\bar{e}_{31}L_n^3}{(-\bar{c}_{13}L_n - L_n) + \bar{e}_{31}L_n\bar{c}_{33}} ((-\bar{c}_{13}L_n - L_n)^2 - \bar{c}_{11}L_n^2\bar{c}_{33}) - \bar{c}_{11}L_n^4 - \left( \frac{\bar{e}_{31}L_n^3}{(-\bar{c}_{13}L_n - L_n) + \bar{e}_{31}L_n} \right)^2}$$

$$( \bar{e}_{31}L_n^3 ) \left[ \frac{\bar{e}_{31}L_n^5 \bar{\epsilon}_{11}(-\bar{c}_{13}L_n - L_n)}{(-\bar{c}_{13}L_n - L_n) + \bar{e}_{31}L_n\bar{c}_{33}} - \frac{\bar{\epsilon}_{11}L_n^2(c_{13}L_n + L_n)}{(c_{13}L_n + L_n) - \bar{c}_{31}L_n\bar{c}_{33}} ((-\bar{c}_{13}L_n - L_n)^2 - \bar{c}_{11}L_n^2\bar{c}_{33}) \right]$$

$$M_4 = \frac{\left( \frac{\bar{e}_{31}L_n^3}{(-\bar{c}_{13}L_n - L_n) + \bar{e}_{31}L_n\bar{c}_{33}} \right) [ ((-\bar{c}_{13}L_n - L_n)^2 - \bar{c}_{11}L_n^2\bar{c}_{33}) - \bar{c}_{11}L_n^4 - \left( \frac{\bar{e}_{31}L_n^3}{(-\bar{c}_{31}L_n - L_n) + \bar{e}_{31}L_n\bar{c}_{33}} \right)^2 ]}{-\bar{\epsilon}_{11}L_n^2(\bar{c}_{13}L_n + L_n)} \quad (69)$$

The solution to Eq. (55) will be the acoustic amplitude distribution in the plate. the particular potential solution now

must be matched at the boundary of the plate to complete the solution of the problem. Eq. (68) is a sixth-order ordinary differential equation, which has six roots, but because of the form of the solution only three roots need to be considered, since the other three roots yield the same solution and need not be considered.

Now let's take the solution of the form

$$B(x_3) = E e^{\gamma x_3} \quad (70)$$

Substitution in Eq. (68) results in:

$$M_1\gamma^6 + M_2\gamma^4 + M_3\gamma^2 + M_4 = 0 \quad (71)$$

Since only three roots need to be considered, this results in:

$$M_1\gamma^3 + M_2\gamma^2 + M_3\gamma + M_4 = 0 \quad (72)$$

The roots of (72) must now be introduced back into the equation of (70):

$$B(x_3) = \sum_{i=1}^3 E_i e^{\gamma_i x_3} \quad (73)$$

Also from (55)

$$\psi_{PS}(x_1, x_3) = \sum_{n=1}^{\infty} \sum_{i=1}^3 E_i e^{\gamma_i x_3} \cos(L_n x_1) \quad (74)$$

which must also satisfy the driving potential at the face of the plate (i.e.,  $x_3 = +h$ )

$$\psi_{PS}(x_1, h) = \sum_{n=1}^{\infty} B_n(h) \cos(L_n x_1) \quad (75)$$

where  $L_n$  now must be matched with the driving wavenumber (i.e.,  $K = \frac{\omega}{c_w} \sin \theta_0$ ), where in the above  $c_w$  is the speed of sound in water,  $\omega$  is the driving frequency,  $\theta_0$  is the steering angle and  $B_n(h)$  is the amplitude of the wave at the surface evaluated from (73).

To obtain the spatial filtering curve (i.e., acoustic amplitude distribution versus normalized wavenumber), a particular wavenumber corresponding to specific steering angle was chosen and the operating frequency was set at the corresponding resonant frequency. This results in the evaluation of the acoustic amplitude distribution from (75).

The theoretical analysis that was just derived was performed for the parameters of the piezoelectric material used in this thesis for a fixed normalized frequency and 10° steering. Figure 4 shows such a plot. The abscissa is the normalized wavenumber and the ordinate is the normalized acoustic amplitude distribution in the plate truncated to unity. It is clear that at the normalized wavenumber of 10° steering, the acoustic amplitude distribution goes to infinity. and as the wavenumber changes, the amplitude decreases exponentially. This spatial filtering curve is the main phenomenon in the continuous piezoelectric plate that serves to reduce the grating lobe.

Since the phases to steer the beam in the continuous plate have been quantized, the numerical analysis using fast Fourier transform was performed to get the theoretical beam pattern for a continuous plate. The beam pattern for a continuous piezoelectric plate length of 2L can be written as:

$$V(K', \theta) = \int_{-L}^{L} e^{iK'x_1 \sin \theta} e^{i\zeta(x)} \quad (76)$$

where  $\zeta(x)$  is the quantized phase necessary to steer the beam electrically. The first term in the integral is the directivity

pattern,  $K'$  is the wavenumber,  $x_1$  is the distance (i.e.,  $-L < x_1 < L$ ) and  $\theta$  is the physical angle. Taking the inverse Fourier transform of the second term in Eq. (76) gives;

$$D(K) = \int_{-L}^L e^{ikx} [\cos[\zeta(x)] - i \sin[\zeta(x)]] dx \quad (77)$$

Now the spatial filtering function of Figure 4 must be multiplied to obtain a new spatial distribution:

$$Y(K) = Z(K) D(K) \quad (78)$$

where  $Z(K)$  is the spatial filtering curve defined numerically from (75). Now by taking the inverse Fourier transform of (78), we obtain

$$Y(x) = \int_{-L}^L e^{-ikx} Y(K) dK \quad (79)$$

and the beam pattern can now be evaluated by taking yet another inverse Fourier transform by using Eq. (76):

$$V(K', \theta) = \int_{-L}^L e^{ik'x_1} \sin\theta Y(x) dx \quad (80)$$

Figure 5 shows the theoretical beam pattern for  $2\lambda$  spacing where there is no spatial weighting function and the beam has been steered to  $10^\circ$  with uniform amplitude shading. The first grating lobe can be seen to be at about  $27^\circ$ . Figure 6 shows the same beam pattern identically except the spatial filtering function has been introduced. The grating lobe can be seen to be reduced considerably. In contrast to the acoustically isolated and electrically segmented plate the acoustic amplitude distribution in the plate is uniform since the segments move as a whole, so there is no spatial filtering effect in a discrete segmented piezoelectric plate.

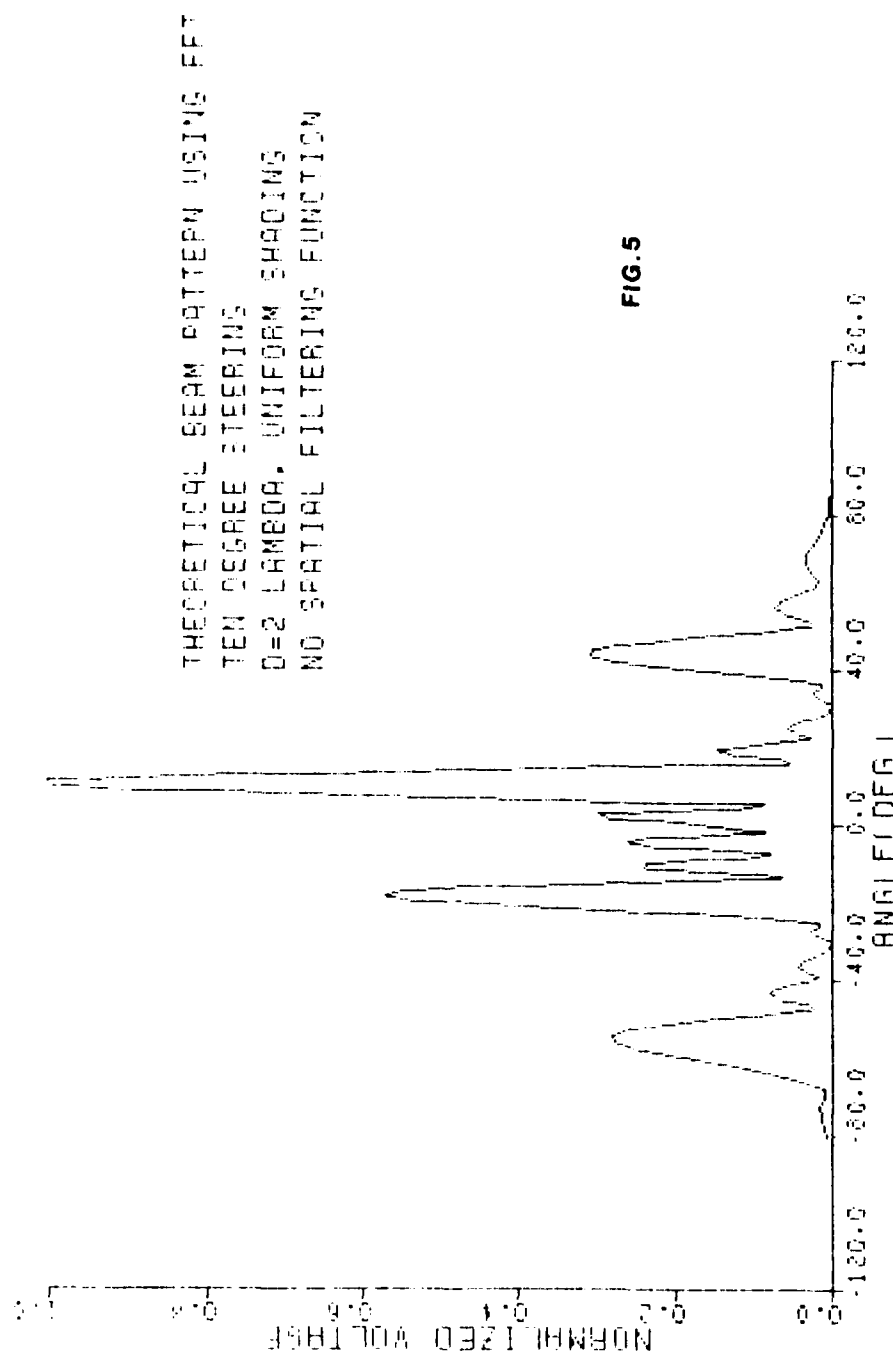


Fig. 5 Theoretical beam pattern,  $10^\circ$  steering,  $2\lambda$  spacing, uniform shading, no spatial filtering

THEORETICAL BEAM PATTERN USING FET  
TEN DEG STEERING  
 $\lambda=2$  LAMBDA. UNIFORM SHAPING  
SPATIAL FILTERING FUNCTION

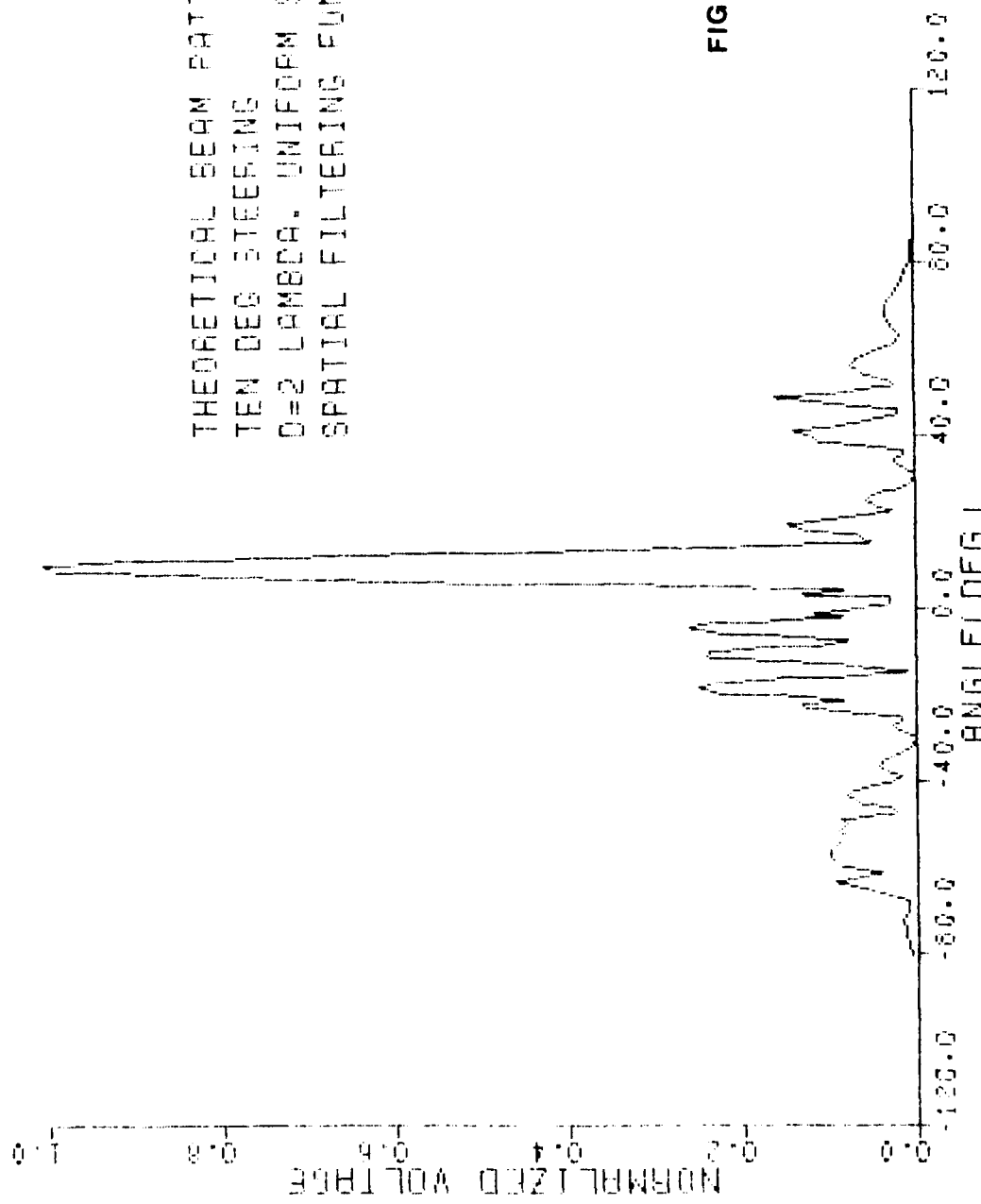


Fig. 6 Theoretical beam pattern,  $10^\circ$  steering,  $2\lambda$ , spacing, uniform shading, spatial filtering

## REFERENCES

## CHAPTER II

1. H. F. Tiersten and R. D. Mindlin, "Forced Vibrations of Piezoelectric Crystal Plates," *Quart. Appl. Math.* 20, 107 (1962)
2. D. C. Gazis and R. F. Wallis, *Acta Mech.* 1, 253-264 (1965)
3. R. D. Mindlin, "High Frequency Vibrations of Crystal Plates," *Quart. Appl. Math.* 20, 107 (1962)
4. H. F. Tiersten, "Thickness Vibrations of Piezoelectric Plates," *J. Acoust. Soc. Am.* 35, 53 (1963)
5. H. S. Paul, "Vibrational Waves in a Thick Infinite Plate of Piezoelectric Crystal," *J. Acoust. Soc. Am.* 44, 478 (1968)
6. R. D. Mindlin, Ref. 3, (1962)
7. W. P. Mason, Piezoelectric Crystals and their Application to Ultrasonics, D. Van Nostrand Co, New York, N. Y., 1950
8. H. Jeffreys, Cartesian Tensors, Cambridge University Press, New York, 1931
9. R. K. Kaul and R. D. Mindlin, "Vibrations of an Infinite Monoclinic Crystal Plate at High Frequencies and Long Wavelength," *J. Acoust. Soc. Am.*, 34, 1895 (1962)

10. H. Ekstein, "High Frequency Vibrations of Thin Crystal Plates," *Phys. Res.* 68, 11 (1945)
11. R. S. Elliot, Antenna Theory and Design, Prentice Hall, Englewood Cliffs, N.J., 1981.
12. E. C. Jordan and K. G. Balmain, Electromagnetic Waves and Radiating Systems, Prentice-Hall, Englewood Cliffs, N.J., 1968
13. R. Urick, Principles of Underwater Acoustics, McGraw-Hill, New York, N.Y.

#### OTHER REFERENCES

14. R. D. Mindlin, "High Frequency Vibrations of Crystal Plates," *Quart. Appl. Math.* 19, 51 (1961)
15. R. D. Mindlin, "Forced Thickness-Shear and Flexural Vibrations of Piezoelectric Crystal Plates," *J. Appl. Phys.* 23, 83 (1952)
16. D. V. Schick and H. F. Tiersten, An Analysis of Thickness-Extensional Trapped Energy Mode Transducers, *Ultrasonics Symposium*, 509 (1982)
17. W. G. Cady, Piezoelectricity, Dover Publications, Inc., New York (1962), p. 16

18. H. F. Tiersten and B. K. Sinha, An Analysis of Extensional Modes in High Coupling Trapped Energy Resonators, Ultrasonic Symposium Proceedings, 167, 1978
19. B. A. Auld, Wave propagation and Resonance in Piezoelectric Materials, J. acoust. Soc. Am., 70, 1577 (1981)
20. J. L. Bleustein and H. F. Tiersten, "Forced Thickness Shear Vibrations of Discontinuously Plated Piezoelectric Plates," J. Acoust. Soc. Am. 43, 1311 (1968)
21. R. D. Mindlin and H. L. Cooper, "On the Equations of Extensional Motion of Crystal Plates," Quart. Appl. Math., Vol XIX, No. 2, 111 (1960)
22. B. A. Auld, Acoustic Fields and Waves in Solids, Vol. II, Wiley and Son, New York, N.Y. (1973)

CHAPTER III  
EXPERIMENTAL ANALYSIS

### 3.0 Introduction

In this chapter the theoretical analysis of Chapter II will be verified against experimental data. The first part of this chapter provides a description of the receiver-transmitter, the physical condition in which the transducer was tested, the experimental set-up, system design and the phasing scheme used to steer the beam electrically over a certain aperture range.

In the second part of this chapter the experimental measurements for the dispersion curve, the grating lobe, and the mirror lobe in the continuous plate and in the discrete plate when applicable will be analyzed. The effect of two, three and four bit quantization on side-lobe structure, the mirror lobe and grating lobe will be compared against the lobes of a segmented discrete type.

### 3.1 Receiver/Transmitter

In this part the receiver and transmitter properties, the physical condition under which the transducer was tested, the instrumentation system design to obtain the data, and the phasing scheme used to steer the beam electrically will be discussed.

### 3.1.1 Transducer

Although the transducer used in this thesis to provide the experimental measurement could be used both as a receiver and transmitter, it was used as a transmitter only. The transducer material used is piezoelectric ceramic (CHANNEL INDUSTRIES 5500). CHANNEL 5500 has a high sensitivity and good time stability. The dimensions of the piezoelectric plate used in this experiment are  $2 \times 2 \times 0.24$  inches. It is operated in its thickness fundamental mode of mechanical oscillation and is also polarized along its thickness direction.

The numerical values of elastic, piezoelectric, mass density and dielectric constants obtained from CHANNEL INDUSTRIES for lead zirconate (CHANNEL 5500) are:

$$C_{11} = 12.1 \times 10^{10} \text{ Newton/meter}^2 \quad \rho = 7.75 \times 10^3 \text{ kg/m}^3$$

$$C_{33} = 11.1 \times 10^{10} \text{ Newton/meter}^2 \quad \epsilon_{11}/\epsilon_0 = 1730 \text{ Relative dielectric constant, free}$$

$$C_{44} = 2.11 \times 10^{10} \text{ Newton/meter}^2 \quad \epsilon_{33}/\epsilon_0 = 1700 \text{ Relative dielectric constant, free}$$

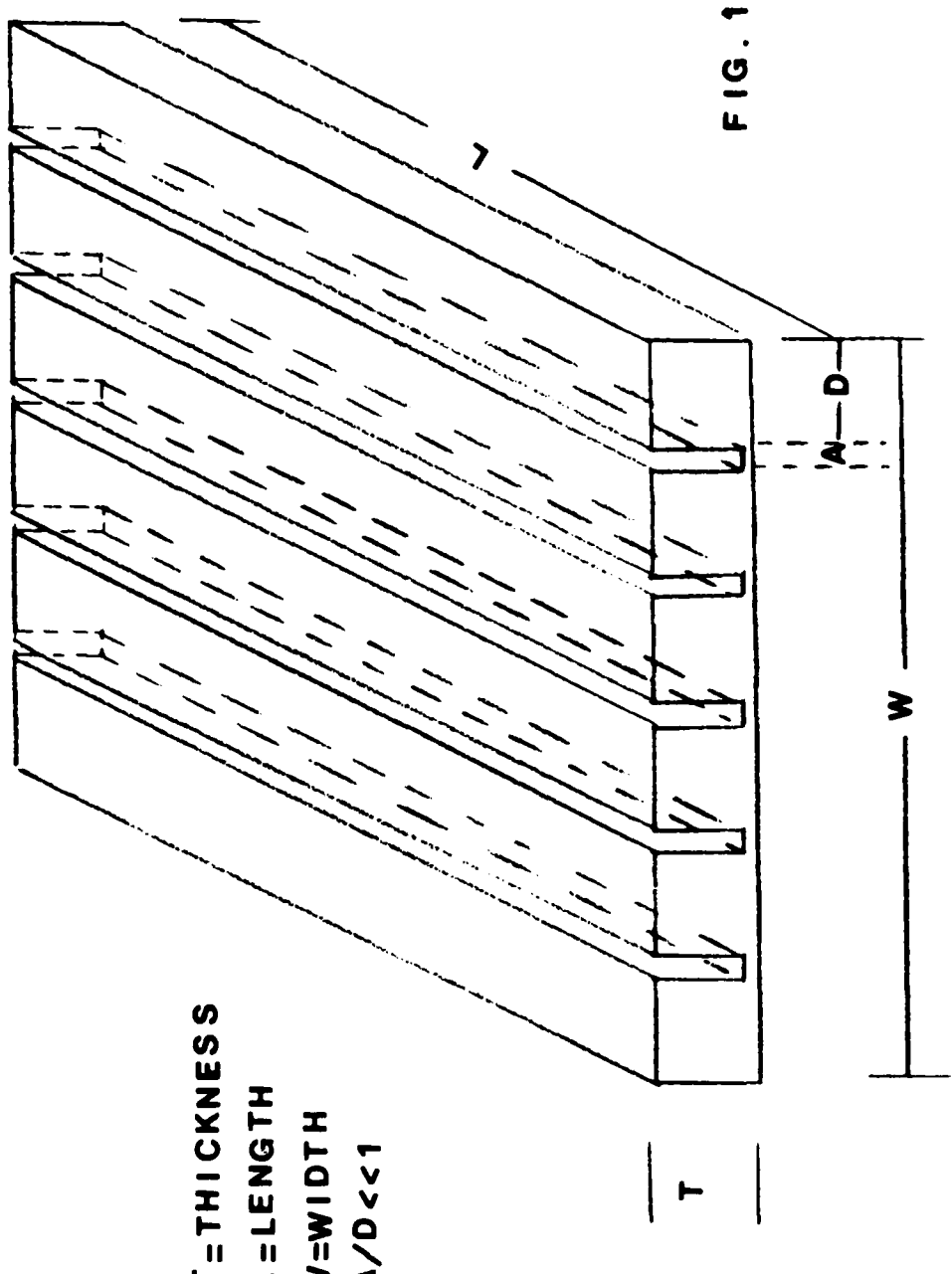
$$C_{12} = 7.54 \times 10^{10} \text{ Newton/meter}^2 \quad e_{33} = 15.8 \text{ Columb/m}^2$$

$$C_{13} = 7.52 \times 10^{10} \text{ Newton/meter}^2$$

For CHANNEL type 5500 piezoelectric material the frequency constant of the thickness mode is approximately 78 KHZ-INCH. Using this figure the resonant frequency of the continuous plate was calculated to be approximately 325 KHZ. The actual maximum response at zero degree steering was measured to be at 348 KHZ.

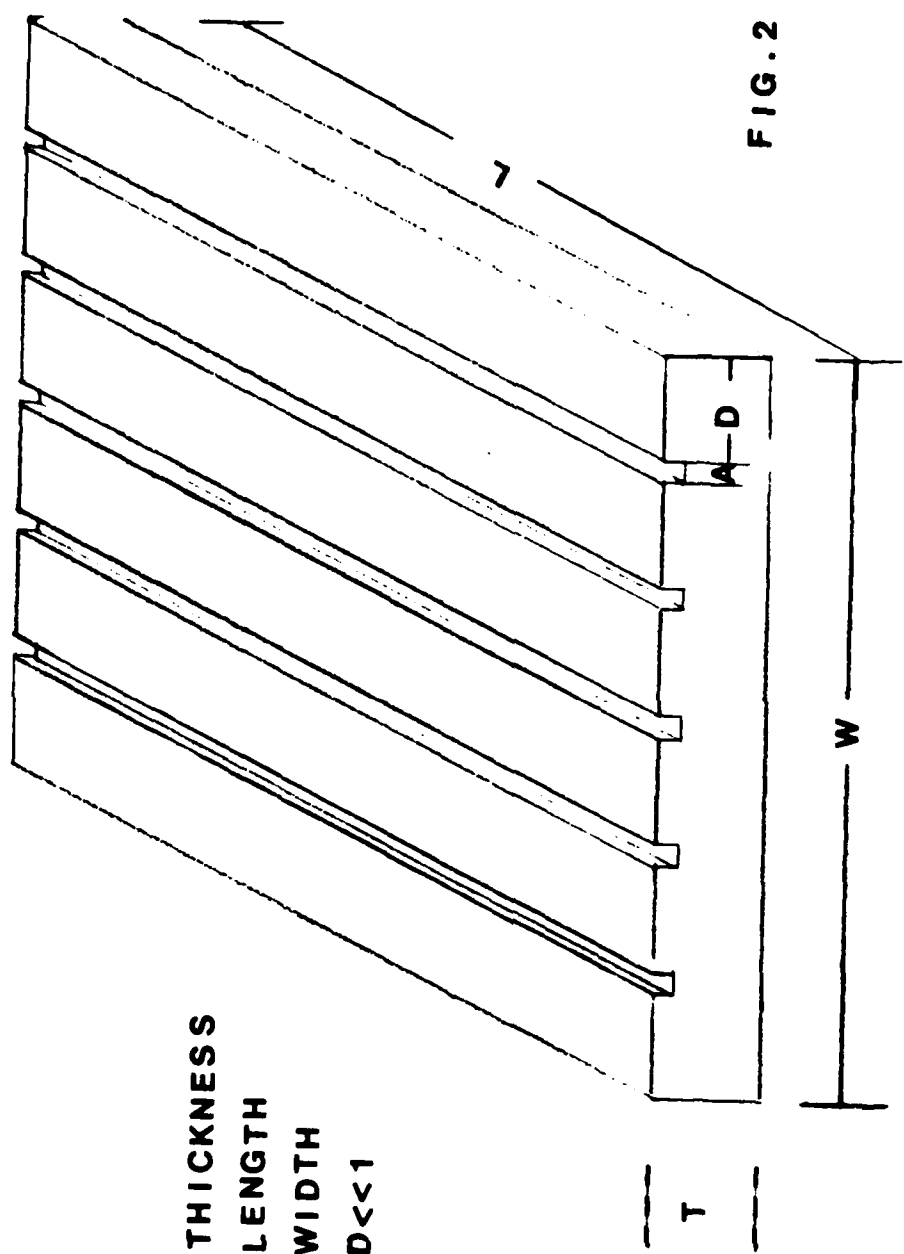
In order to permit the beam to be steered electrically, the transducer was segmented by a diamond saw to isolate the thin conducting sheet electrically. Twenty segments approximately 0.92 inches wide were cut. For the discrete type the segments were cut deep enough to isolate the segments both acoustically and electrically. Figure 1 shows the physical cross-section for such a plate. The segments for the continuous plate were isolated electrically by cutting only the thin conducting sheet with very shallow depth. Figure 2 shows the cross-section for this plate.

Both transducers were set in polyvinyl circular packages. The piezoceramic elements were mounted only at the top and bottom edges of the plate, where the acoustical loading is so minimal that it can be neglected. Figure 3 shows the cross-section of the package which was used in this thesis. Since the plate segments will be driven electrically the package was filled



**ELECTRICALLY, ACOUSTICALLY ISOLATED PLATE  
DISCRETE TYPE**

Fig. 1. Electrically acoustically isolated plate, discrete plate



**ELECTRICALLY ISOLATED PLATE  
CONTINUOUS TYPE**

Fig. 2. Electrically isolated plate, continuous plate.

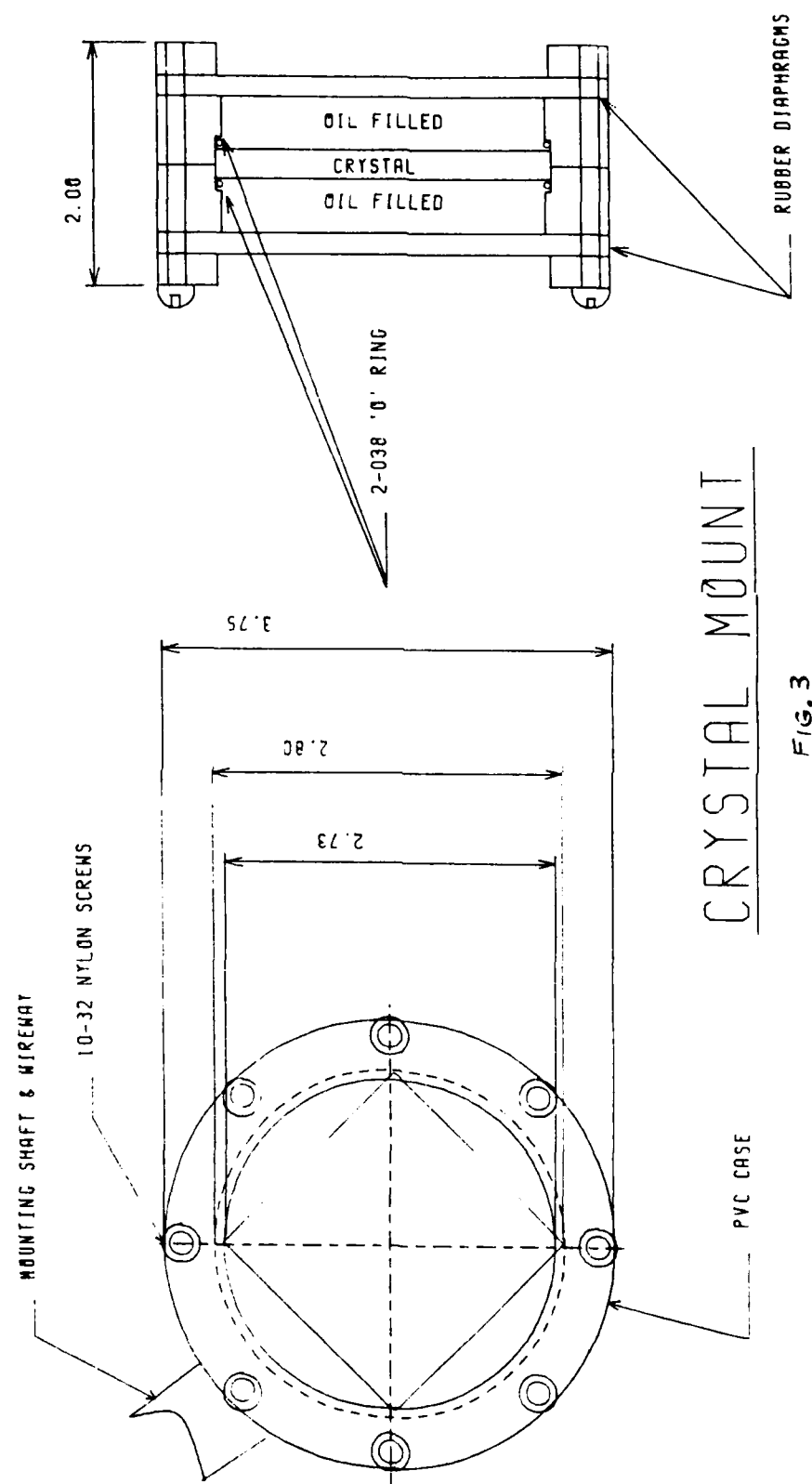


Fig. 3. Crystal mount package.

with castor oil. The main reason for choosing castor oil as an insulating medium is that its acoustic impedance matches that of the water.

Since the plate, which can have a wide variation in electrical impedance, must be driven electrically over long wire length, there could be additional phase shifts which could distort the phasing scheme and could affect the beam pattern of the system, especially the side-lobe structure. A solution to this was to shunt the segments with a resistor which, in combination with the 1.8 KOHM reactance of the ceramic (at resonance) yields a characteristic impedance of approximately 100 OHM, matching the characteristic impedance of the twisted pair wire. The cable used is made by the 3M Company as ribbon cable type. It has 20 twisted pairs which are used for the twenty segments.

The beam width of the transducer used in this experiment was calculated to be approximately 5.2 degrees at the operating frequency of 325 KHZ beyond 1 meter and 5 cm wide at shorter ranges.

The hydrophone used to obtain the acoustical data is an encapsulated 1/8x1/8 inch ceramic cylinder resonant at about 380 KHZ. It was located approximately 1 meter away from the

transducer so that a far field measurement of the transducer would be valid. This distance was calculated to be 1/2 meter from  $D^2/\lambda$ , where D is the aperture size of the transducer and  $\lambda$  is the wavelength at the operating frequency of 325 KHZ.

The experiment was tested in a 2'x3'x4' polyethelene-lined tank. Figure 4 shows the tank in which the system was tested. Because of the limited dimensions of the test tank, the pulse width for the signal was set short enough to isolate the reflection from the boundaries.

### 3.1.2 Instrumentation System Design

Figure 5 is a block diagram of the instrumentation system used in this thesis which consists of seven basic blocks: transducer driver, transducer, hydrophone, hydrophone receiver, analog to digital converter, system motor drive and data acquisition system.

The system was designed to provide arbitrary phasing of the individual segments. This was set by picking a minimum quantization interval of  $2\pi/16$ . To obtain this we multiplied the carrier frequency by 16 on a frequency burst generator (WAVETEK) to clock the sixteen stage shift register (74LS164). A

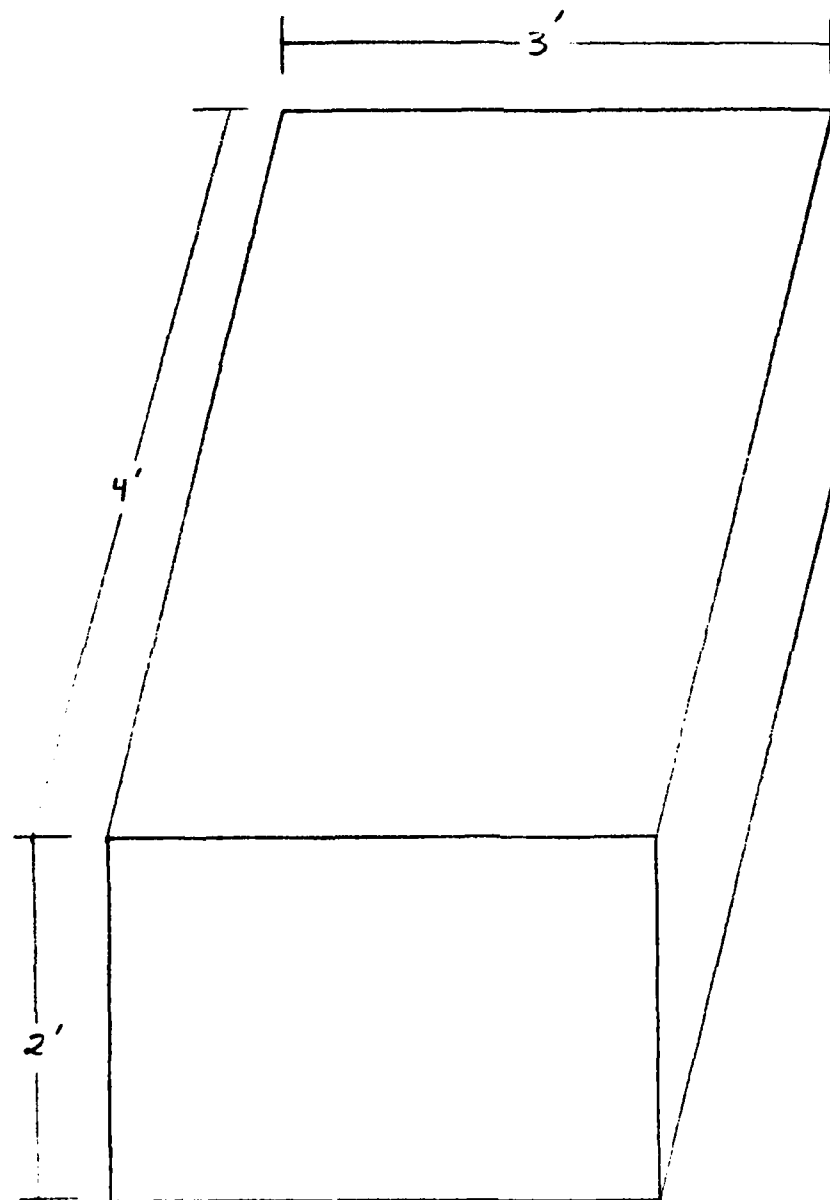


FIG. 4

Fig. 4. Test tank.

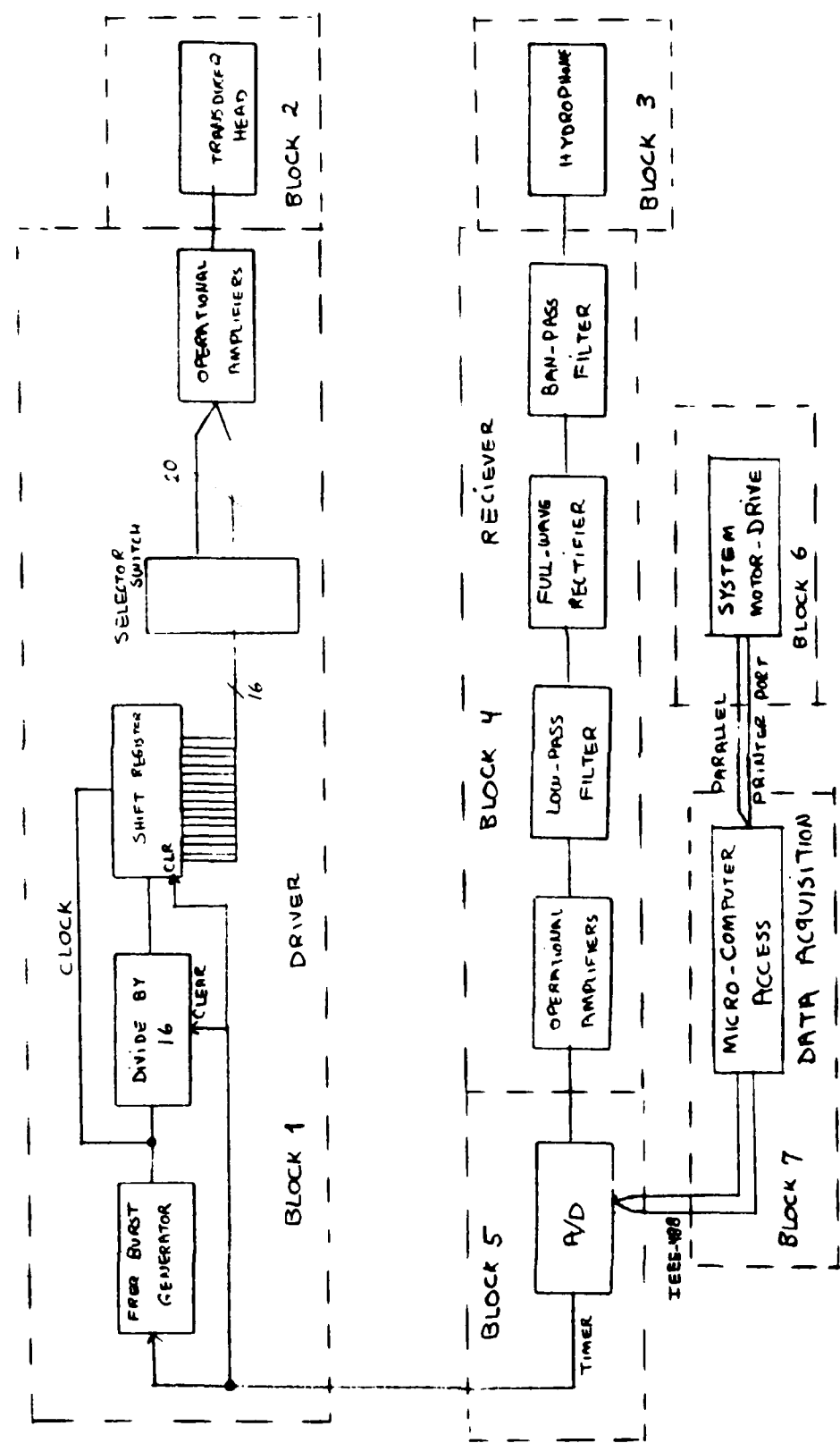


FIG. 5

Fig. 5 Instrumentation system design diagram

divide by sixteen counter output (74LS163) was used as the input to the shift register. This method provided sixteen phases uniformly between zero and  $2\pi$ . The first eight phases out of the shift register were used as inputs to a pair of (8x10) mini-matrix selector switches and the last eight to another pair of (8x10) switches. These selector switches provided the selection of any of the sixteen phases to each of the 20 individual segments. Twenty double-pole single throw switches were used to select between the first eight and the last eight phases. A variable gain amplifier is used to amplify the signal that now must drive the transducer segments. This variable gain amplifier allows the amplitude to be adjusted on each individual segment to obtain any desired drive amplitude shading across the transducer.

The hydrophone output was filtered to reduce the noise in the channel and increase the signal to noise ratio for measurements. A full wave rectifier and a low-pass filter was used to generate the envelope of the acoustic signal and then amplified by two stages of low noise and high bandwidth gain (HA4620-8) to drive the A/D converter input.

Block five shows the analog to digital converter. This is a multiplexed A/D converter controlled over the IEEE-488 bus

RD-A157 278

BEAM STEERING OF ELECTRICALLY SEGMENTED PIEZO-CERAMIC  
ULTRASONIC TRANSDUC. (U) SCRIPPS INSTITUTION OF  
OCEANOGRAPHY LA JOLLA CA MARINE PHYSIC. - H ESLAMBOLCHI

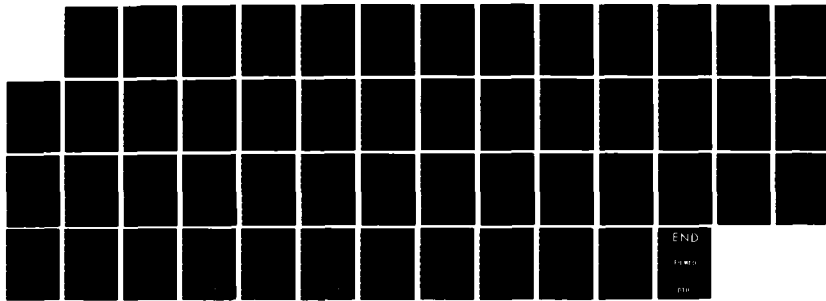
2/2

UNCLASSIFIED

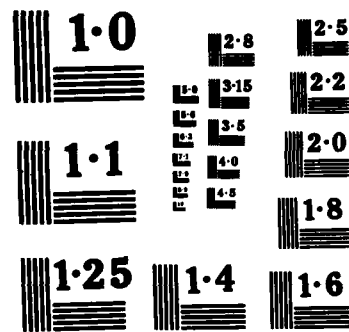
01 DEC 84 MPL-U-76/84 N00014-88-C-0220

F/G 20/1

NL



END  
FILED  
DPO



NATIONAL BUREAU OF STANDARDS  
MICROCOPY RESOLUTION TEST CHART

(Connecticut Micro Computer). The A/D converter has sixteen channels of analog input multiplexer which sequentially sample the input data at a 110 microsecond sampling rate into an 8 bit packed data stream. It also includes the time which was used both to trigger the WAVE TEK and to reset the divide by sixteen counter and shift register after the analog data was converted into digital data.

Block six is the system motor drive which is controlled by the computer. This motor is a SLO-SYN motor with 72 steps per revolution. In order to achieve higher resolution on the rotating angle, a reducing gear was used. This motor was rotated mechanically by using a two bit sequence that was controlled by the software in the computer via its parallel printer port.

Block seven is the data acquisition system which is the main processor in the experiment. This microcomputer (ACCESS) uses its IEEE-488 port to control the WAVE TEK parameters and to control and receive data from the A/D converter. It also generates the sequence needed to step the motor via the parallel printer port. The data reduction was controlled in the software and then stored on a 5 1/4 inch floppy disk (MAXWELL MD1). The

divide by sixteen counter output (74LS163) was used as the input to the shift register. This method provided sixteen phases uniformly between zero and  $2\pi$ . The first eight phases out of the shift register were used as inputs to a pair of (8x10) mini-matrix selector switches and the last eight to another pair of (8x10) switches. These selector switches provided the selection of any of the sixteen phases to each of the 20 individual segments. Twenty double-pole single throw switches were used to select between the first eight and the last eight phases. A variable gain amplifier is used to amplify the signal that now must drive the transducer segments. This variable gain amplifier allows the amplitude to be adjusted on each individual segment to obtain any desired drive amplitude shading across the transducer.

The hydrophone output was filtered to reduce the noise in the channel and increase the signal to noise ratio for measurements. A full wave rectifier and a low-pass filter was used to generate the envelope of the acoustic signal and then amplified by two stages of low noise and high bandwidth gain (HA4620-8) to drive the A/D converter input.

Block five shows the analog to digital converter. This is a multiplexed A/D converter controlled over the IEEE-488 bus

plot of the beam pattern was made on the integral dot-matrix printer of the ACCESS by a software plotting package obtained from Enercomp Company.

### 3.1.3 Phasing Scheme

Quantization of the phase was necessary in order to steer the beam electrically. The required phases can be calculated for four, three and two bit quantization and for different spacing between the segments. The input drive to the system can be written as:

$$V(\tau) = A \cos(\omega\tau - \phi)$$

where  $A$  is the amplitude of the drive,  $\omega$  is the driving frequency,  $\tau$  is the time, and  $\phi$  is the phase. The phase which must now be quantized can be written by setting  $V(\tau)$  equal to zero; (i.e.,  $\phi = \omega\tau = KC_\omega\tau$ ) where  $C_\omega$  is the speed of sound in

water. Since the plate has been segmented, the total path can be written as:

$$x(N) = C_w \tau = C_w N D \sin\theta$$

where  $N$  is the segment number,  $D$  is the segment spacing. This results in:

$$\phi(N) = \text{INT}\left[\frac{KND \sin\theta}{2\pi}\right] \text{MOD } L$$

where  $L$  is the quantization variable, which can be sixteen, eight, or four depending on the quantization desired (4, 3 or 2 bits).

Figure 6 shows an example of four, three and two bit quantization for  $10^\circ$  steering, one-half wavelength spacing. Figure 7 shows an example of four bit quantization at  $10^\circ$  steering for different spacing. For  $1\lambda$  and  $2\lambda$  spacing, the segments were electrically tied together to form larger segments.

### 3.2 Experimental Analysis

In this part of the thesis the experimental dispersion curve, grating lobe and mirror lobe will be discussed for both the

**TABLE 1**  
**QUANTIZATION OF  $\pi/8$**

SEGMENT NUMBER	4 BIT QUANTIZATION	3 BIT QUANTIZATION	2 BIT QUANTIZATION
1	1	0	0
2	2	2	0
3	4	4	4
4	5	4	4
5	6	6	4
6	8	8	8
7	9	8	8
8	11	10	8
9	12	12	12
10	13	12	12
11	15	14	12
12	0	0	0
13	2	2	0
14	3	2	0
15	4	4	4
16	6	6	4
17	7	6	4
18	9	8	8
19	10	10	8
20	15	10	8

**QUANTIZATION SCHEME**

**FIG.6**

Fig. 6 Quantization of  $\pi/8$ , four, three and two bit

**TABLE 2**

**QUANTIZATION OF PI/8**

**4 BIT**

SEGMENT NUMBER	ONE - HALF LAMBDA	ONE LAMBDA	TWO LAMBDA
1	1	2	4
2	2	2	4
3	4	4	4
4	5	4	4
5	6	8	8
6	8	8	8
7	9	10	8
8	11	10	8
9	12	12	0
10	13	12	0
11	15	0	0
12	0	0	0
13	2	2	4
14	3	2	4
15	4	6	4
16	6	6	4
17	7	8	8
18	9	8	8
19	10	10	8
20	15	10	8

FIG. 7

Fig. 7      Quantization of  $\pi/8$ ,  $\frac{1}{2}\lambda$ ,  $\lambda$ ,  $2\lambda$  spacing

discrete and continuous types of transducers when applicable. The effect of quantization on the beam pattern of the two transducers will be evaluated.

### 3.2.1 Dispersion Curve

The theoretical analysis that was derived in Chapter II was evaluated for the parameters of the experimental continuous segmented transducer. In order to obtain the dispersion curve (i.e., change in velocity versus frequency), a set of phases computed for a desired steering angle was set up on the segments of the transducer. Then a sequence of beam patterns similar to Figures 8 and 9 was generated to identify the frequency of maximum response out of the transducer. The angle of the maximum response was then measured and compared against the desired steering angle. If the angles were matched then the frequency corresponding to the maximum amplitude constitute a point on the dispersion curve; if the angle was not matched, another frequency was chosen, another set of phases computed, and another beam pattern sequence was run. This iteration process was repeated as necessary to obtain points on a dispersion curve.

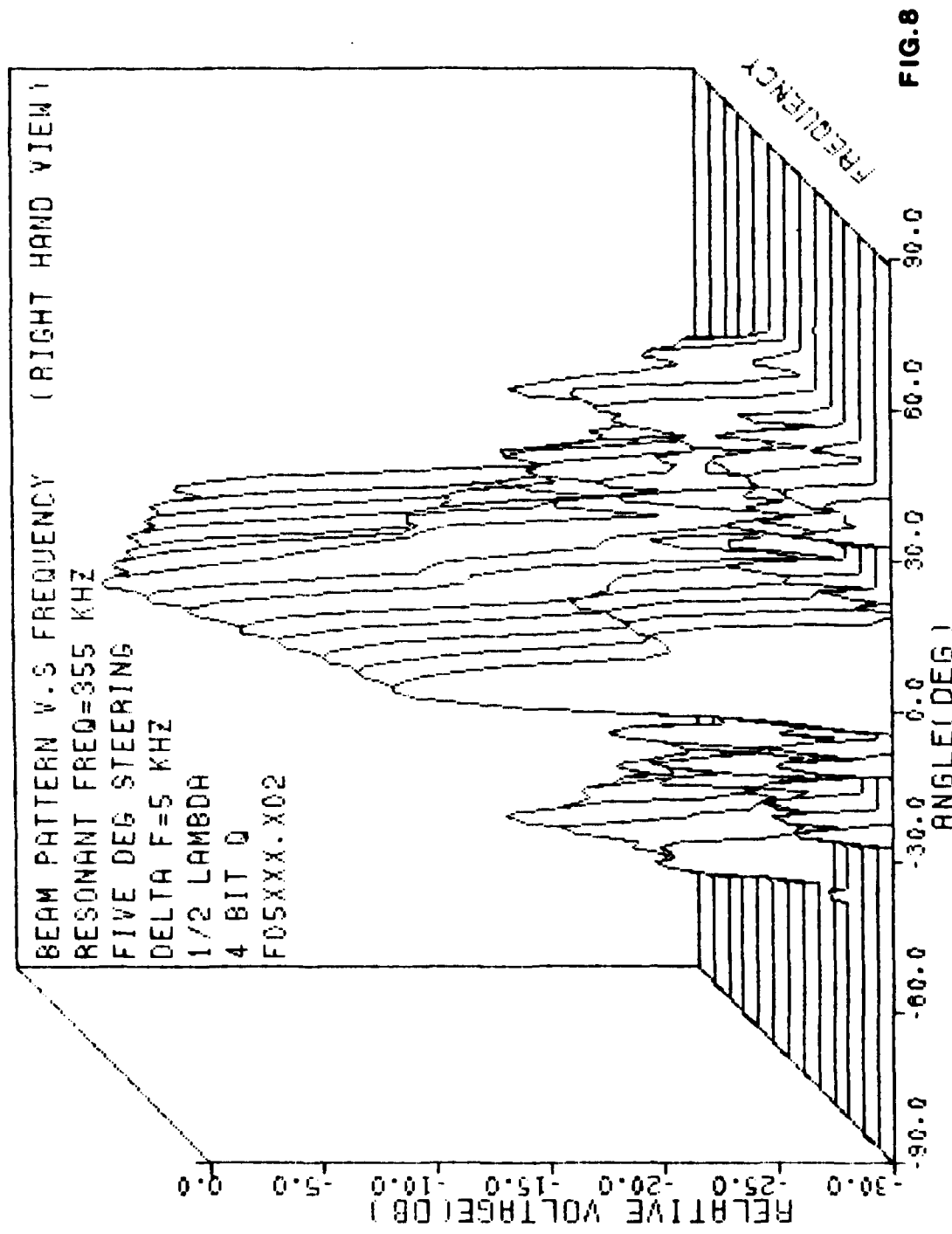


Fig. 8 3-dimensional of beam pattern (right hand view)

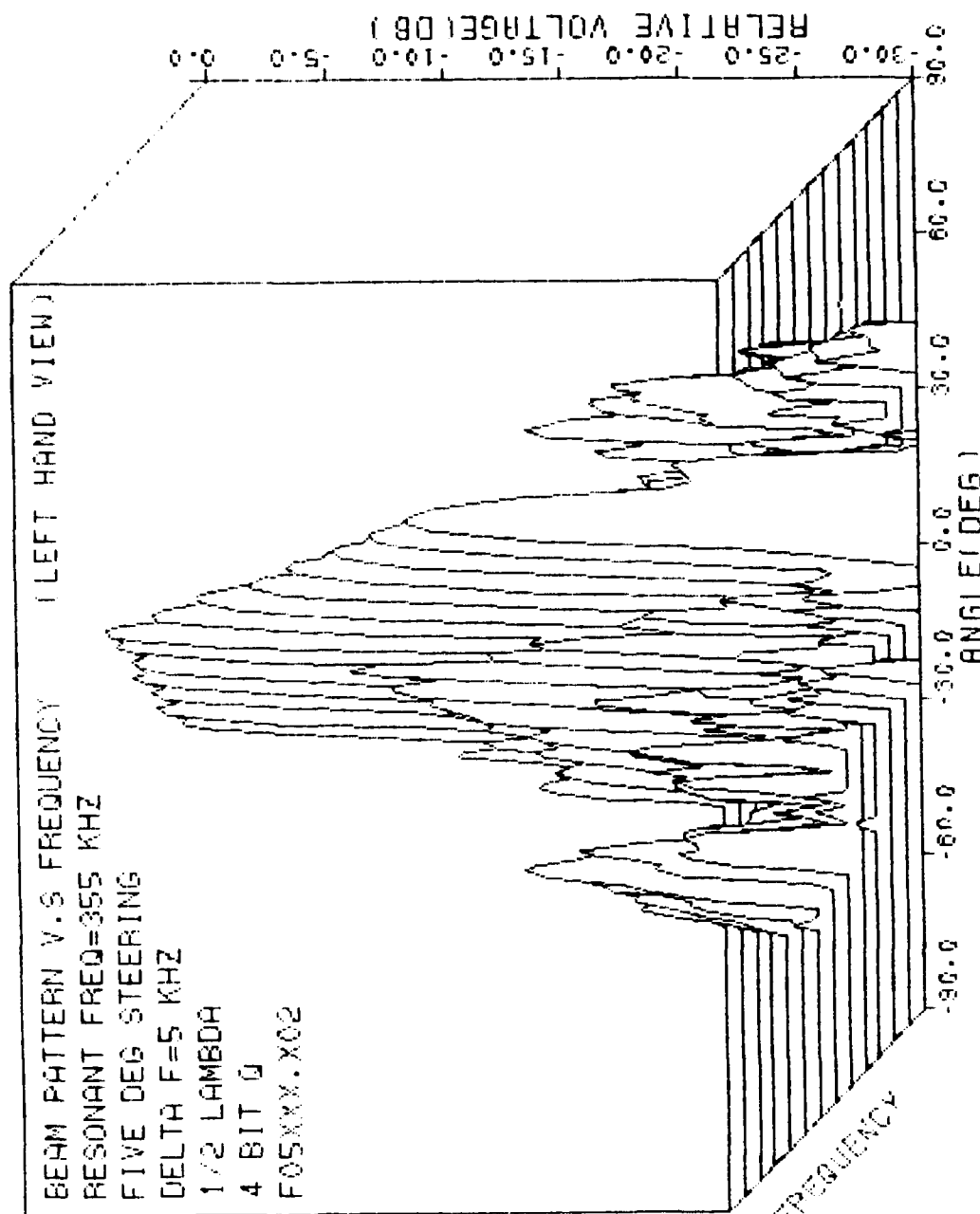


Fig. 9 3-dimensional of beam pattern (left hand view)

Figure 8 and 9 show the final beam pattern for a 5° steering angle at one-half wavelength segment spacing. The abscissa is the angle in degrees, the ordinate is the normalized voltage in (db) and the third axis is the frequency in KHZ. As the frequency is changed the amplitude will rise until it reaches a maximum and then decays as the frequency increases. Figure 8 is a right-hand view and Figure 9 is a left-hand view of the same data.

In order to compare the theoretical dispersion curve versus the experimental one, the data for the experimental transducer was normalized to 325 KHZ so that the comparison could be achieved. The normalized dispersion curve is plotted for the continuous plate in Figure 10. The abscissa is the steering angle in degrees and the ordinate is the frequency in KHZ. The points obtained from measurements form a well-defined curve with very little scatter. Although the experimental points are similar in shape to the theory, the magnitude of dispersion effect of the experimental curve is significantly less. The difference between the experimental and theoretical curves could have been due to limitations in the model. Water loading of the transducer,

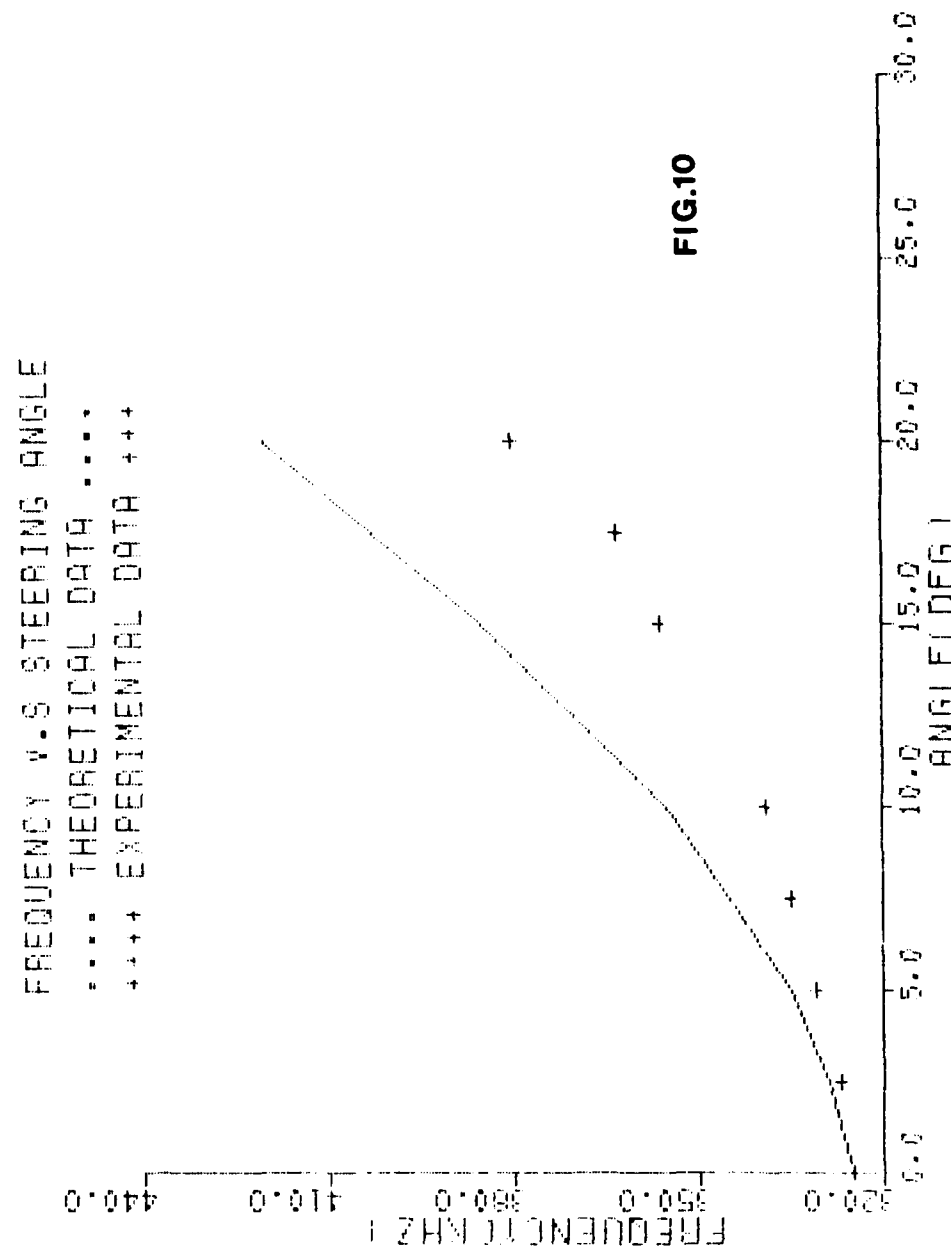


Fig. 10 Experimental dispersion curve, (angle vs. frequency)

ignoring boundary impedance, and the assumption of an infinite plate are all factors that could influence the dispersion.

### 3.2.2 Grating Lobe

In Chapter II it was shown theoretically that because of the spatial filtering in the continuous plate the grating lobe in a continuous plate was reduced considerably. For the discrete segmented plate the grating lobe occurs when the spacing between the segments is greater than one-half wavelength when the beam is steered off normal; i.e.:

$$KD(\sin\theta - \sin\theta_0) = 2n\pi \quad (n = 1, 2, \dots)$$

where  $K$  is the wavenumber,  $D$  is segment spacing,  $\theta$  is the physical angle and  $\theta_0$  is the steering angle.

This results in:

$$\sin\theta = \frac{n\lambda}{2D} \quad \text{if } \theta_0 = -\theta$$

When the phase between the segments reaches  $2\pi$ , the pattern repeats itself, and this happens when we have some integer multiple of spatial harmonic of the wavenumber. Both the theoretical and experimental data for the discrete segmented plate show such an effect. The theoretical and experimental data for 10° steering,  $2\lambda$  spacing, four bit quantization and uniform shading is shown in Figures 11 and 12, respectively. The first grating lobe in both cases occurs at about -27°, as predicted by the theory. The other two grating lobes can also be seen at about +42° and -66° in Figures 11 and 12. The side-lobe structure of both the theoretical and experimental pattern seem to match each other rather well.

In the continuous plate, because of the spatial filtering, the grating lobe was observed to be reduced considerably, as predicted by the theory. The spatial filtering effect in the continuous plate was measured and compared against the theoretical data. To obtain the experimental spatial filtering curve, a particular reference steering angle was selected and the operating frequency was set at the corresponding resonant frequency. The amplitude was then measured for different electrical drive wavenumbers. The normalized experimental curve is plotted in

TEN DEG STEERING  
L=2 LAMGSUR, 4 BIT Q, UNIFORM SPACING  
5 SEGMENTS DISCRETE TIRE

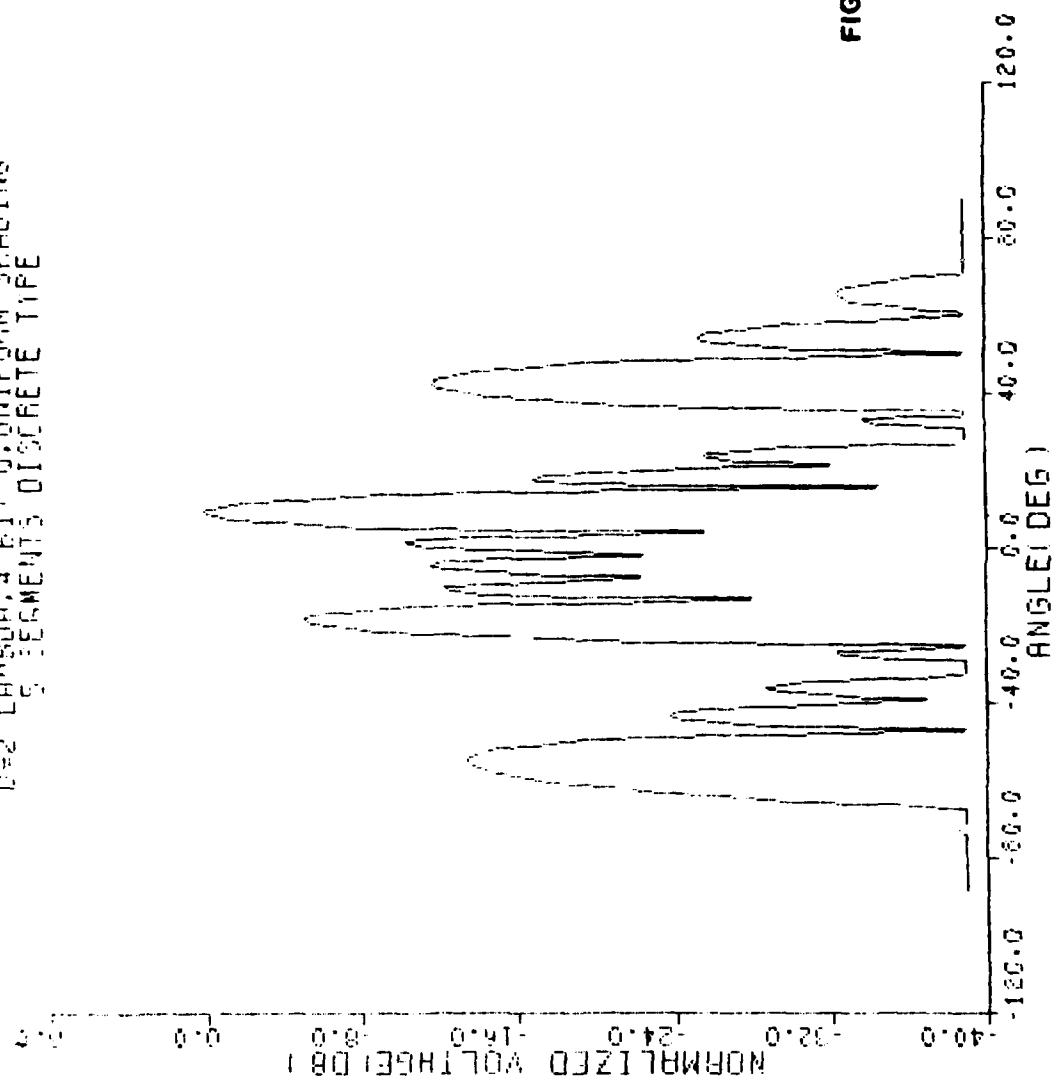
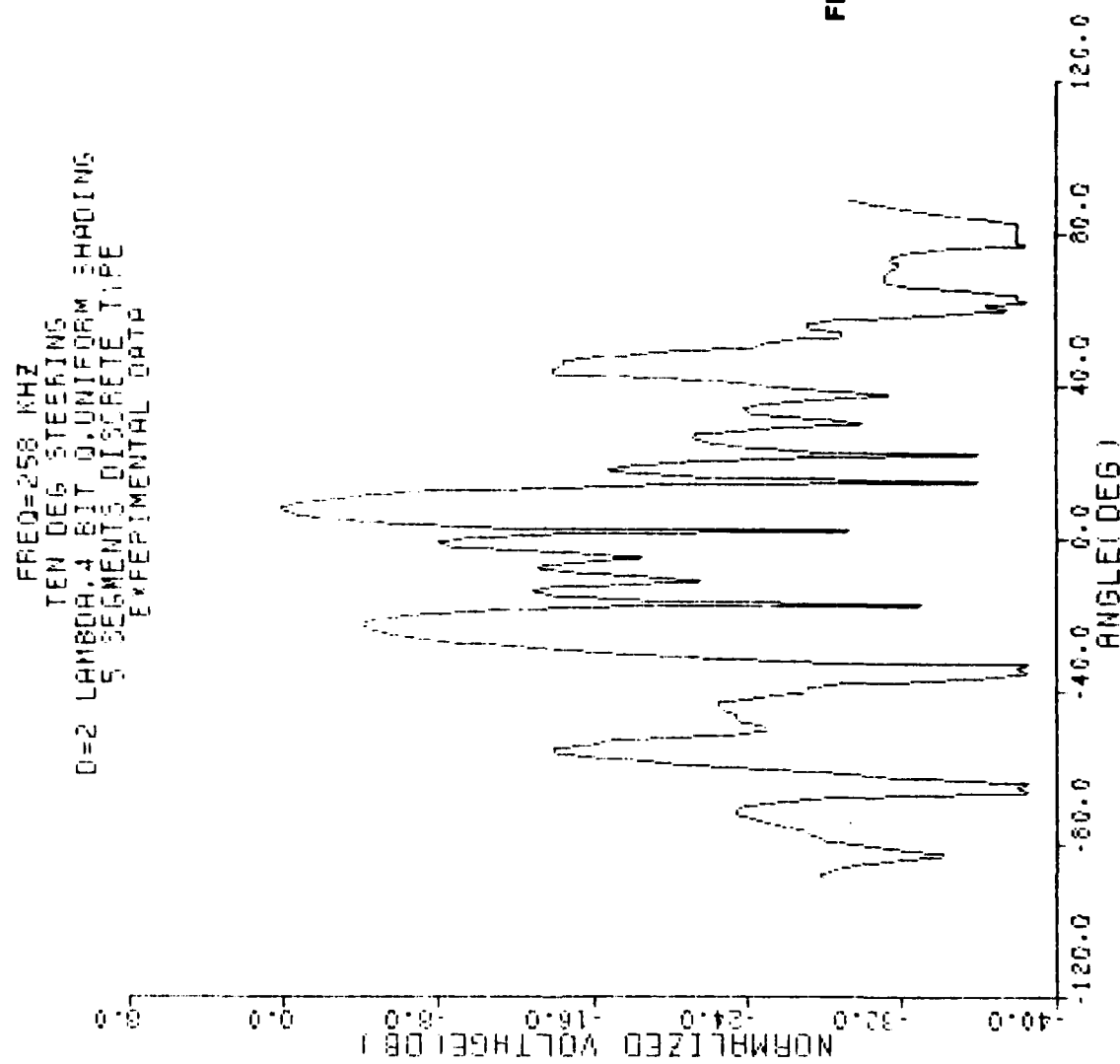


Fig. 11 Theoretical beam pattern,  $10^\circ$  steering,  $2\lambda$  spacing, 4 bit quantization



## Quantization

Figure 13 along with the theoretical spatial filtering curve. The theoretical spatial curve was truncated to unity to achieve a normalization equivalent to measurement. This plot also includes an adjusted wavenumber normalization which was a best match to the experimental curve. The wavenumber adjustment necessary to match this was approximately 10%. This plot is for 10° steering. The abscissa is the normalized wavenumber and the ordinate is the normalized amplitude.

Figures 14 and 15 show the theoretical beam pattern for a 10° steering angle,  $2\lambda$  spacing, and uniform shading, with no spatial filtering and with spatial filtering, respectively. The first grating lobe from the main beam has been reduced by 16 db. The other two grating lobes are shown to have an improvement of about 18 db. The experimental beam pattern for a continuous plate with the same characteristics is shown in Figure 16. The first grating lobe is down at approximately -23 db, which agrees well with the theory. Although the other two grating lobes are shown to also be reduced, the reduction is about 15 db versus a theoretical 20 db.

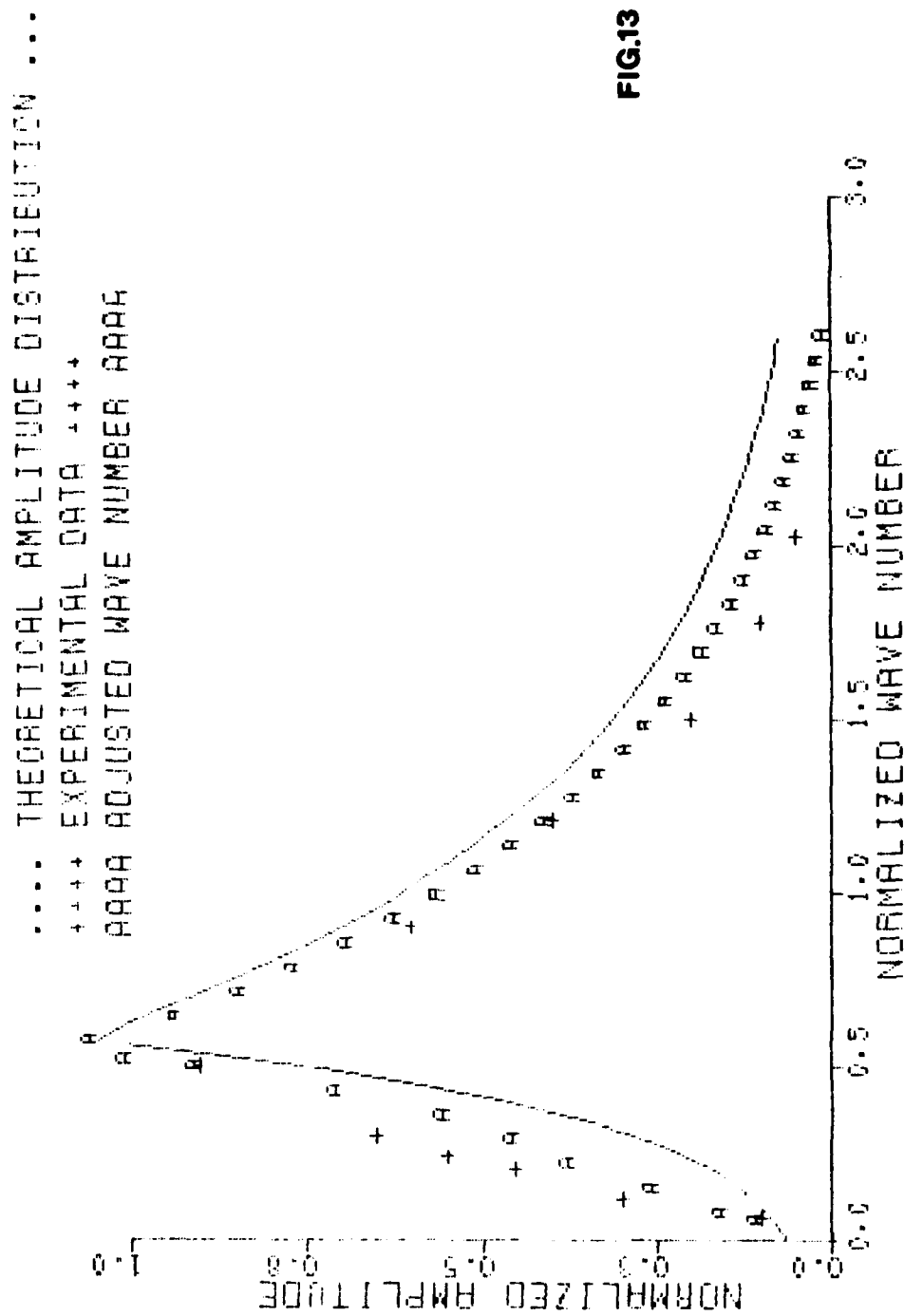


Fig. 13 Theoretical and experimental acoustic amplitude distribution of a continuous plate at  $10^\circ$  steering

THEORETICAL BEAM PATTERN USING FFT  
TEN DEGREE STEERING  
 $D=2$  LAMBDA. UNIFORM SHADING  
NO SPATIAL FILTERING FUNCTION

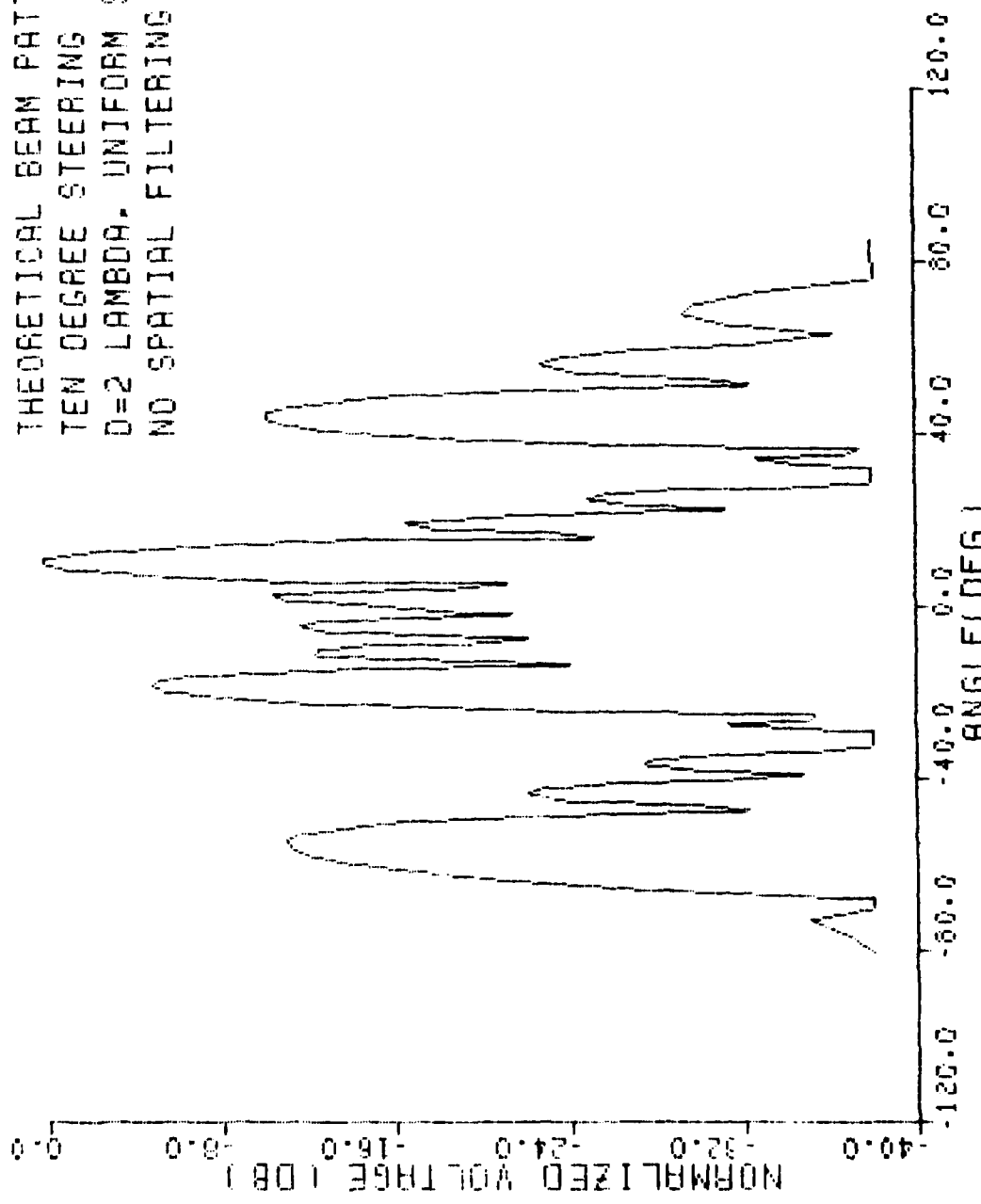


FIG.14

Fig. 14 Theoretical beam pattern,  $10^\circ$  steering,  $2\lambda$ , using FFT

THEORETICAL BEAM PATTERN USING FFT  
TEN DEG STEERING  
 $D=2 \lambda$ , UNIFORM SHADING  
SPATIAL FILTERING FUNCTION

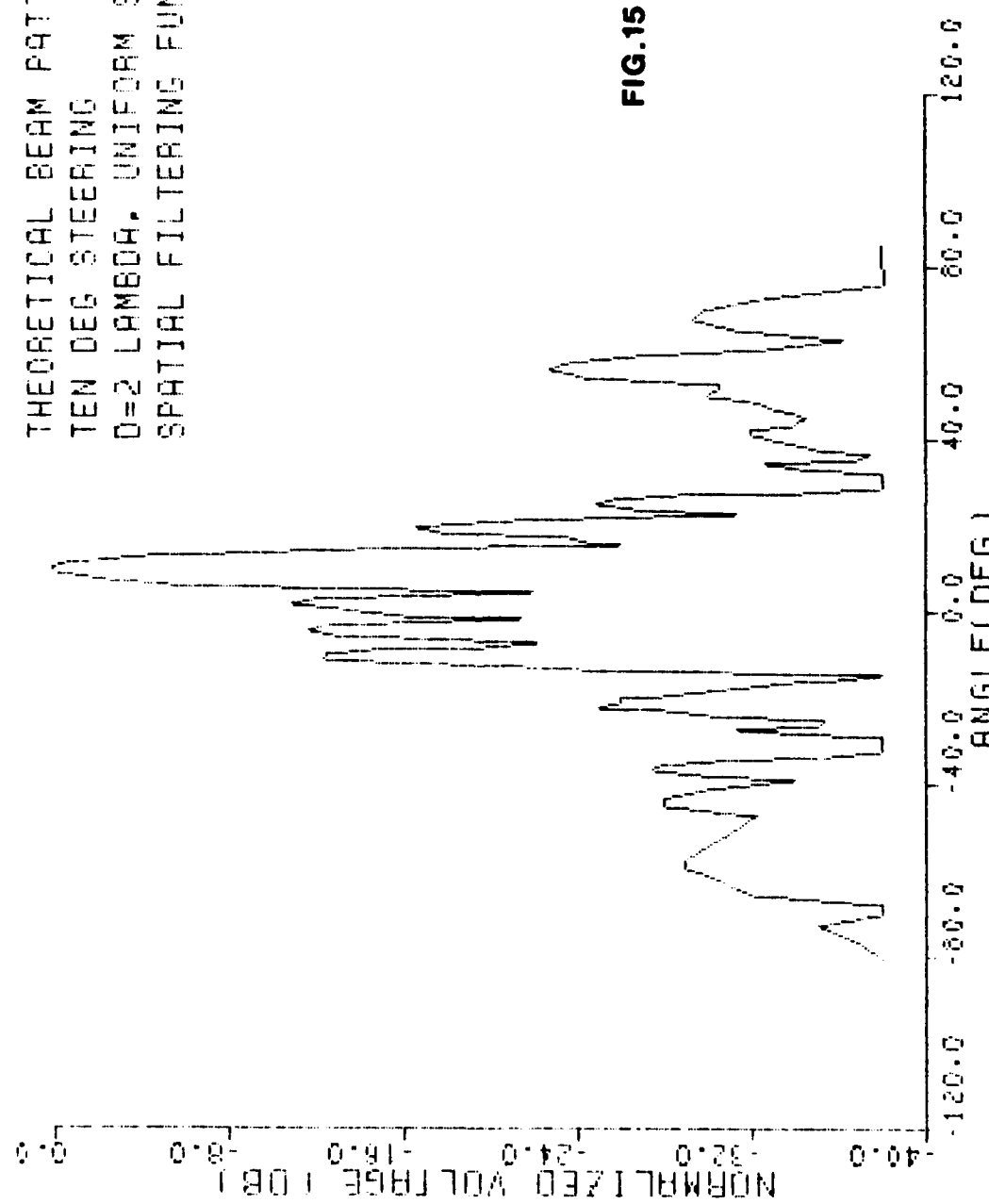


Fig. 15 Theoretical beam pattern,  $10^\circ$  steering,  $2\lambda$ , using FFT,  
spatial filtering function

TEN DEG STEERING  
 $\lambda=2$  LAMBDA 4 BIT, UNIFORM SPACINGS  
 5 STEAVES, CONTINUOUS TYPE  
 EXPERIMENTAL DATA

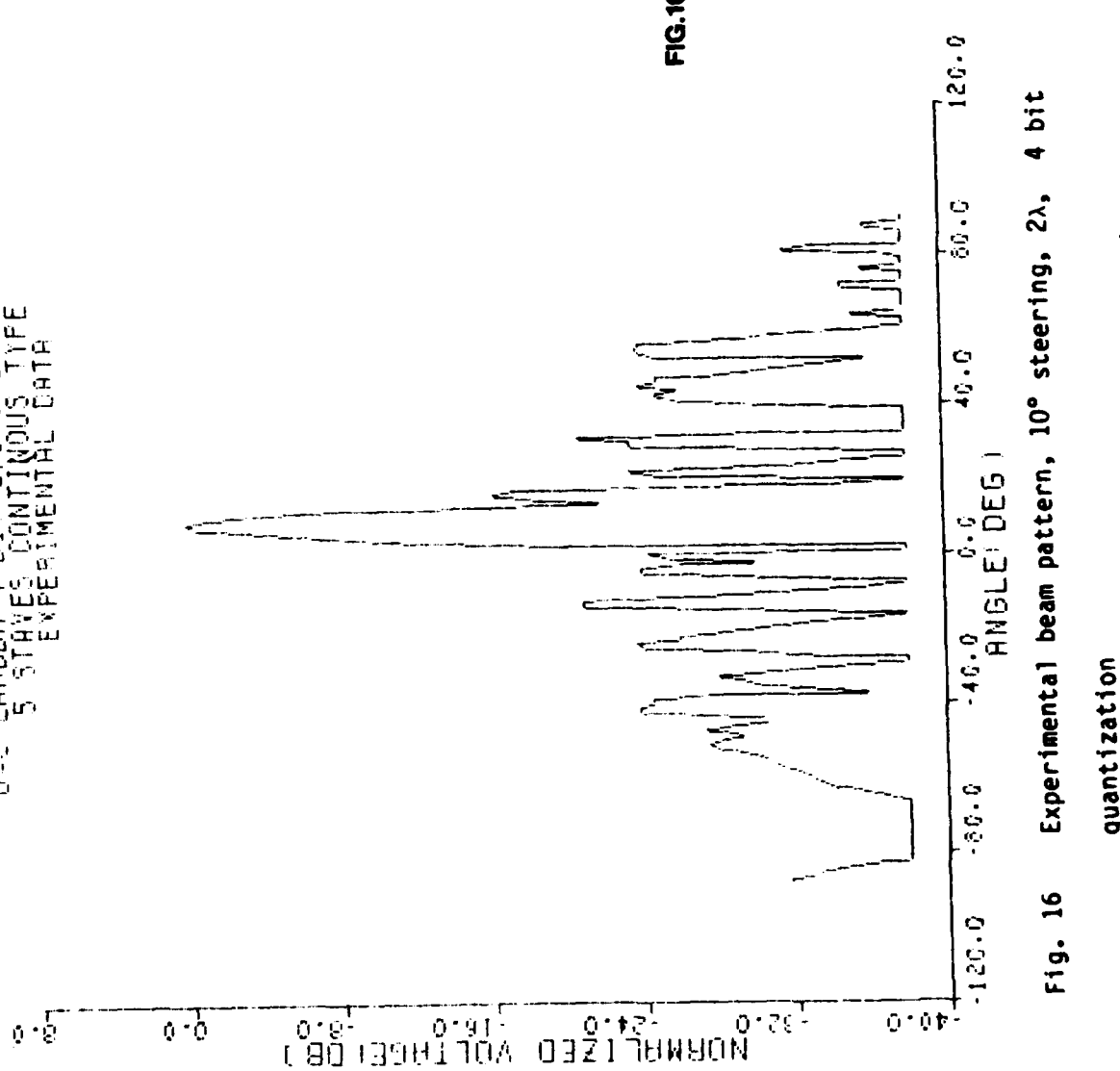


Fig. 16 Experimental beam pattern, 10° steering,  $2\lambda$ , 4 bit quantization

### 3.2.3 Mirror Lobe

The reflection from the edge boundary of the continuous plate that was discussed in Chapter I will cause a standing wave to be formed. This results in a mirror lobe when the beam is steered off normal. An active approach to suppression of the mirror lobe was used and gave good results. Since the phase for each segment could be set independently, it was possible to drive the last three segments in the plate out of phase with the original distribution. This acts to cancel the amplitude of the wave by the time it reaches the edge boundary and in effect reduced the mirror lobe significantly. The number of segments used to reduce the mirror lobe was determined experimentally.

Figure 17 shows the  $12^\circ$  steered beam for a continuous plate with one-half wavelength spacing between the segments. The mirror lobe can be seen to have a high level nearly comparable to the main lobe at about  $-12^\circ$ . Figure 18 shows the same beam pattern except the last three segments were driven out of phase. The mirror lobe can be seen to be suppressed considerably. The suppression is about 12 db. Figures 19 and 20 show the 3-D view of the  $15^\circ$  beam for one-half wavelength spacing for the right-hand view and the left-hand view, respectively. The figures

D=1/2 LAMBDA 0.4 SIT CONTOUR FORM SHADING  
20 STAVES CONTINUOUS TYPE  
EXPERIMENTAL DATA

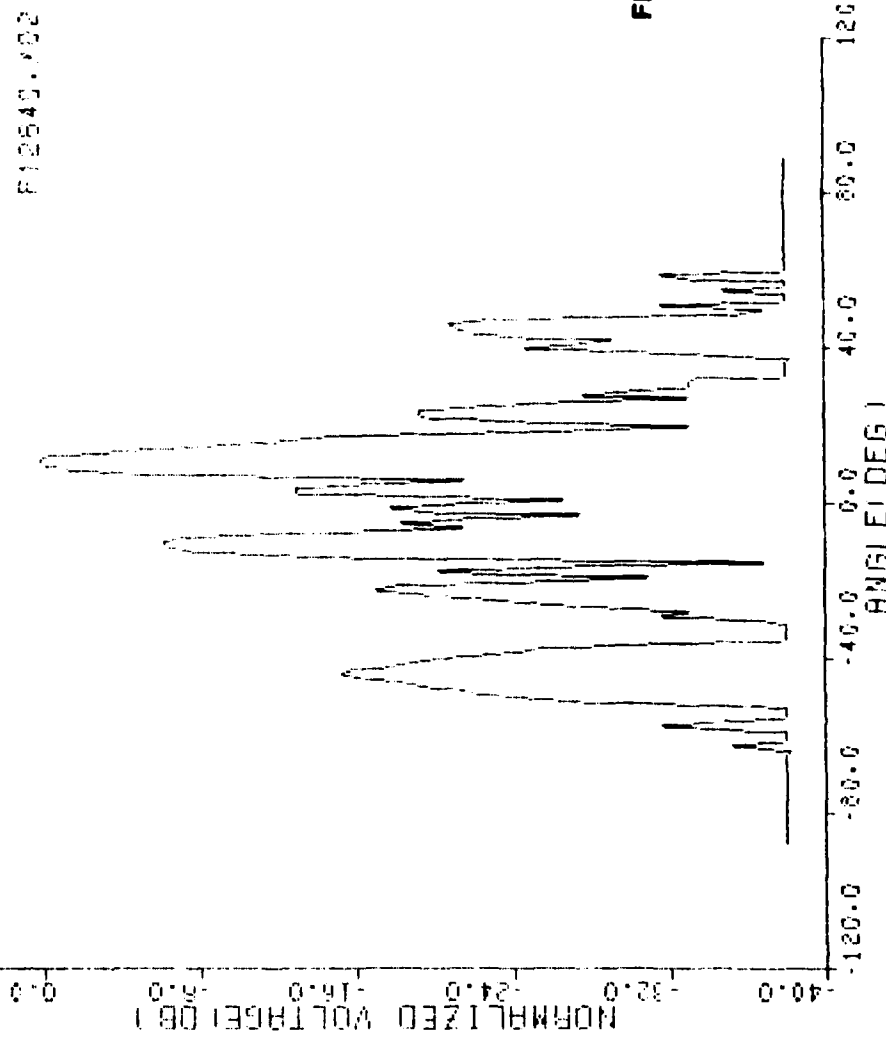


Fig. 17 Experimental beam pattern, mirror lobe

FIG. 18 LENGTH 4 BIT QUINIFORM SHADING  
12.5 DEGREES COUNTING 1 DEG  
EXPERIMENTAL DATA

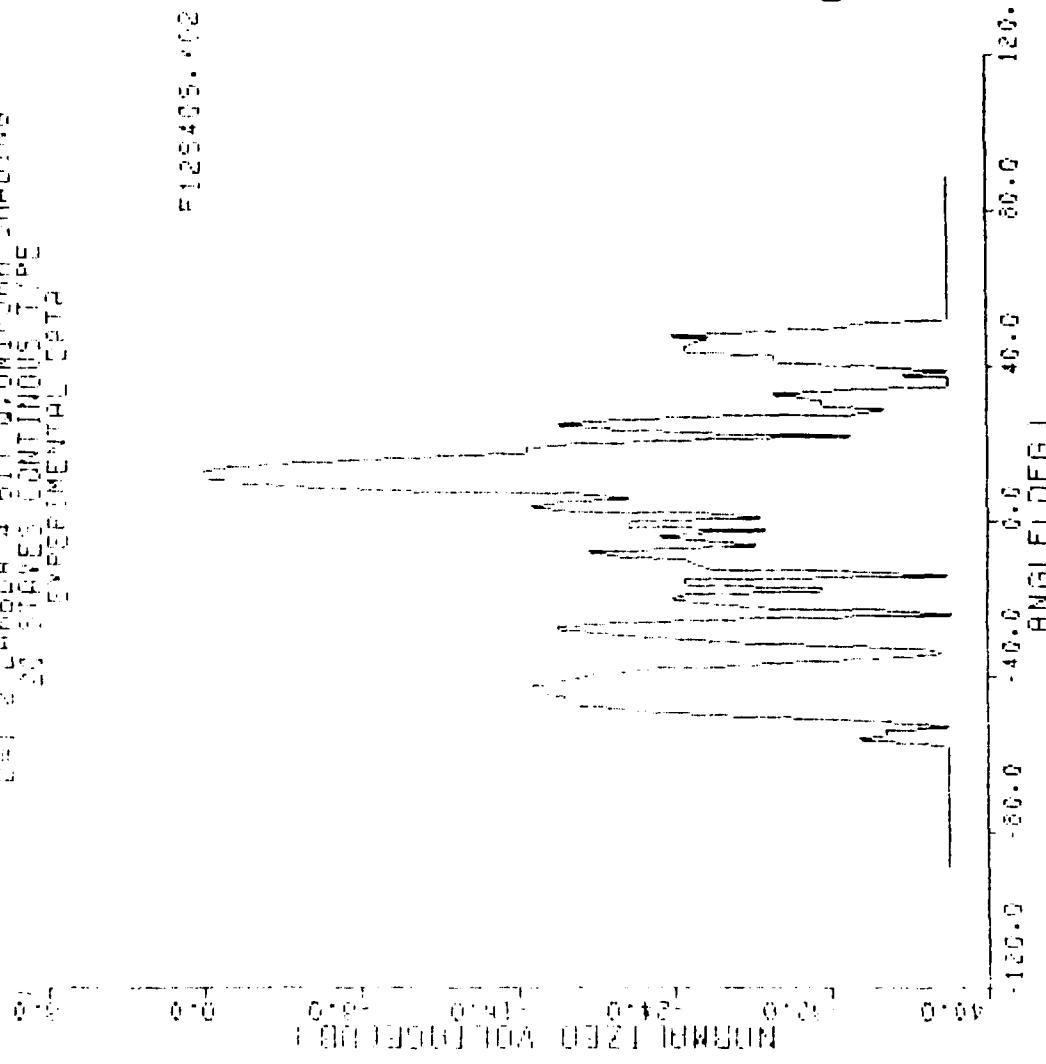


Fig. 18 Experimental beam pattern, mirror lobe suppressed

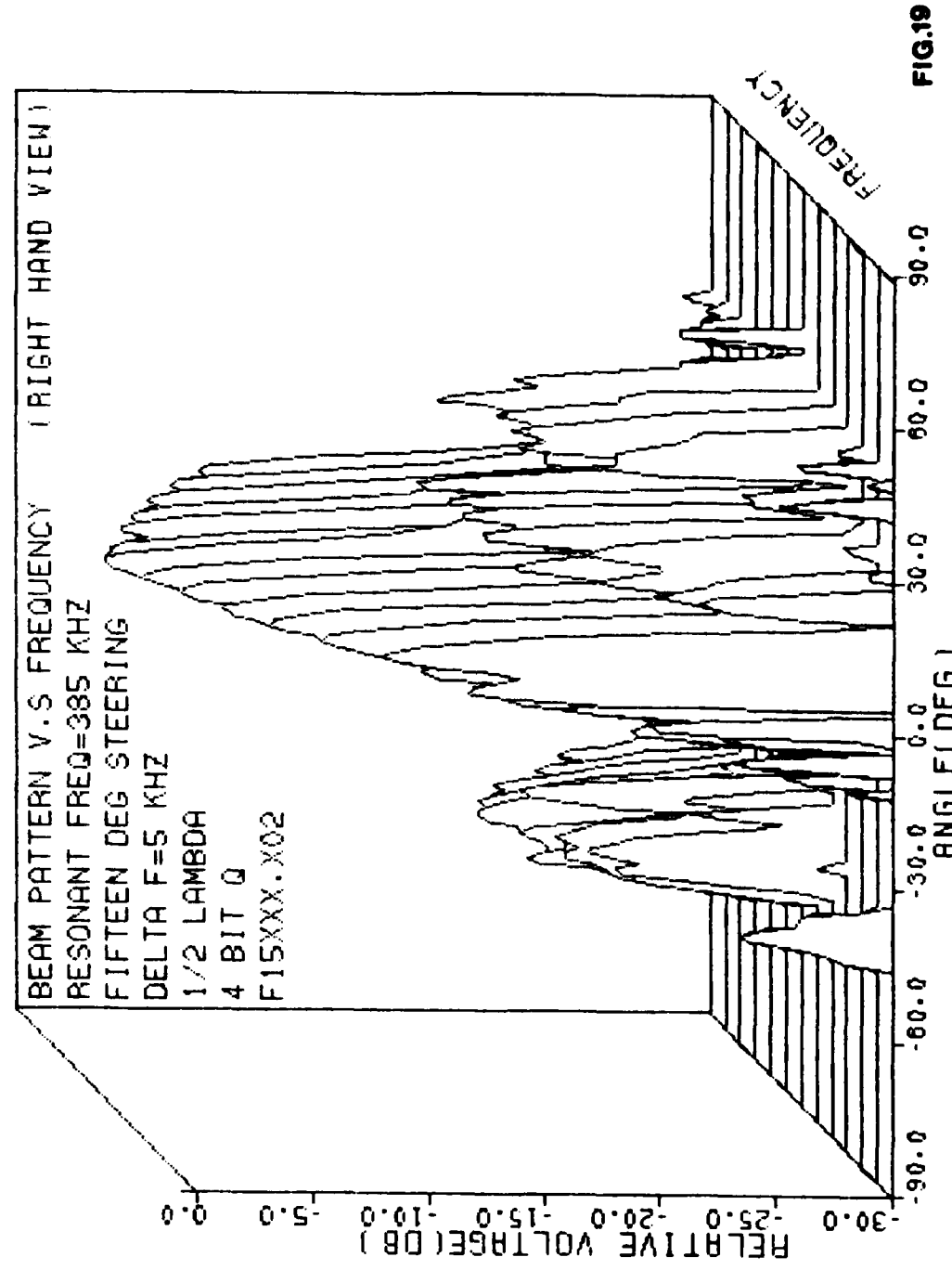


Fig. 19 3D view of 15° beam (right hand view)

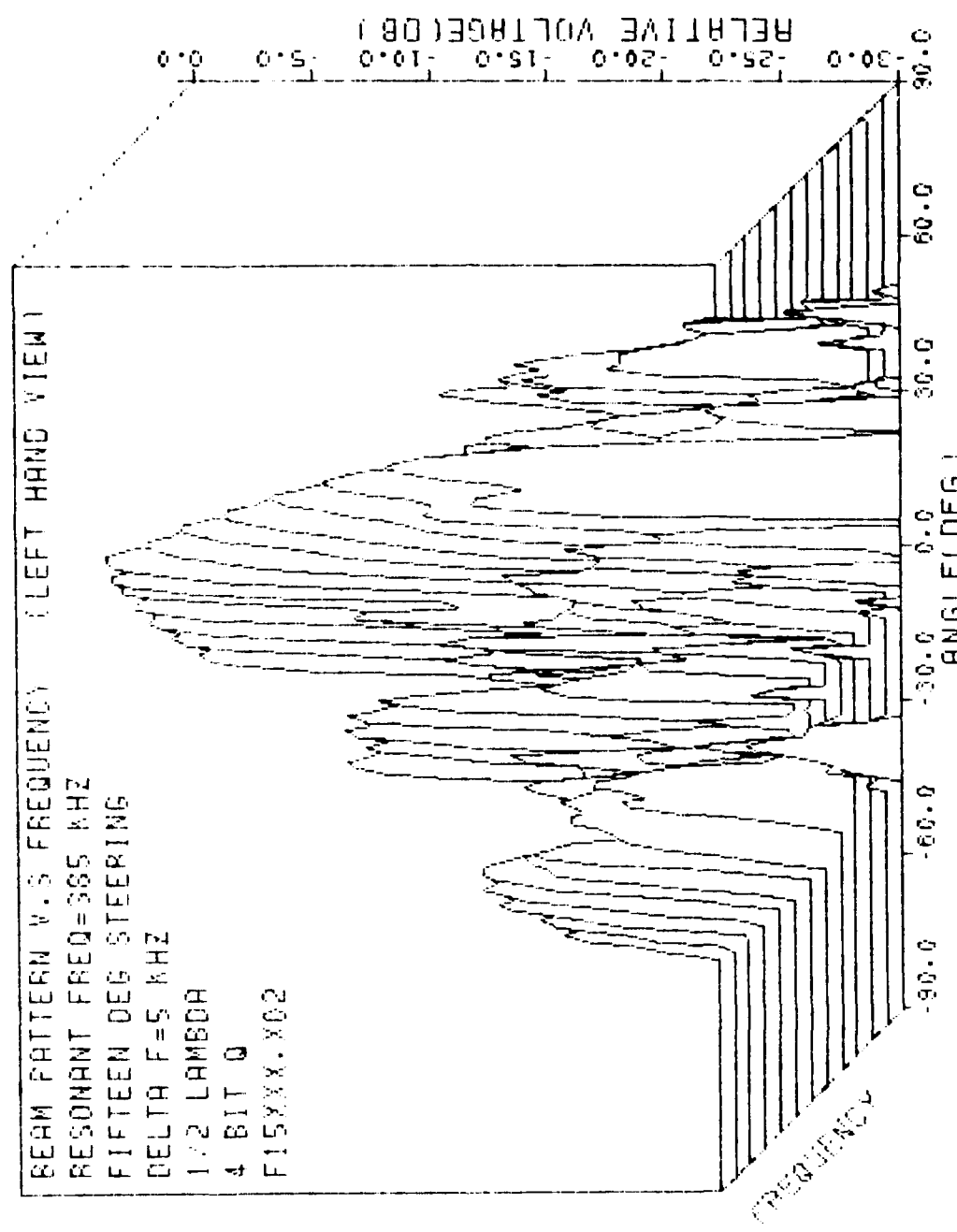


Fig. 20 3D view of 15° beam (left hand view)

show how the mirror lobe moves as the frequency changes. This is an indication of the frequency dependency of the mirror lobe in the continuous plate.

An unexpected low level (-15 db or less) lobe in the measurements of the beam pattern for the continuous plate was observed at approximately -42°. This was probably generated because of the shear modes in the plate which were weakly excited by the electrical drive. With this shear mode there is an associated shear velocity. By Snell's law the angle of the radiated beam can be written as:

$$\sin\theta = \frac{C_w}{C_s}$$

where  $C_w$  is the speed of sound in the water and  $C_s$  is the shear velocity in the plate. In the continuous piezoceramic plate this was given by CHANNEL INDUSTRIES to be 2250 meters/sec. Although the location of the shear lobe was independent of both steering angle and frequency, the amplitude of the radiated lobe had dependency on both frequency and steering angle.

Figure 19 shows a right-hand view and Figure 20 shows a left-hand view for a 15° steered beam and one-half wavelength

spacing. The abscissa is the angle in degrees, the ordinate is the normalized voltage in db and the third axis is the frequency in KHZ. The effect of frequency can be seen to change the amplitude of the shear lobe at  $-42^\circ$  in the beam pattern of the continuous plate. The effect of steering angle on the shear lobe is illustrated by Figure 21, which shows a right-hand view, and Figure 22, which shows a left-hand view for a  $0^\circ$  beam. The amplitude of the lobe is about  $-24$  db for  $0^\circ$  steering versus the  $-16$  db for  $15^\circ$  steering.

### 3.2.4 Quantization Effect on the Lobes

#### of the Discrete and Continuous Plate

The effect of four, three and two bit quantized driving signals was investigated for the discrete and continuous plates.

Figure 23a, 23b and 23c shows a  $10^\circ$  steered beam for a discrete plate at  $1/2\lambda$  spacing, uniform shading for four, three and two bit quantization, respectively. Because of the finer phases of the 4 bit quantization, the side-lobe structure for this quantization was best in comparison with the other two quantizations. This effect can be seen very well at  $-23^\circ$ , where the side-lobe is about  $-20$ ,  $-15$ ,  $-14$  db for the four, three and

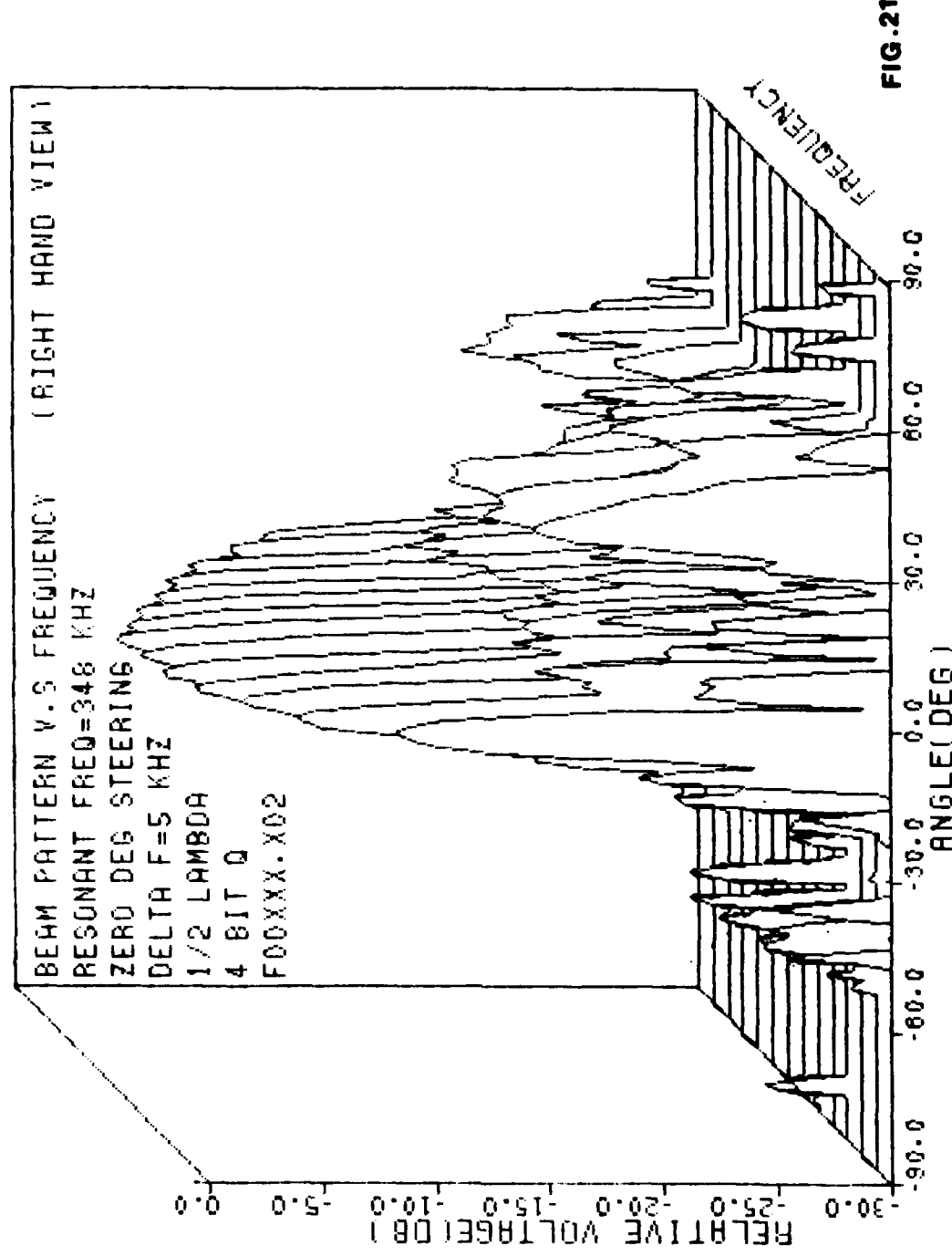


Fig. 21 3D view of  $0^\circ$  beam (right hand view)

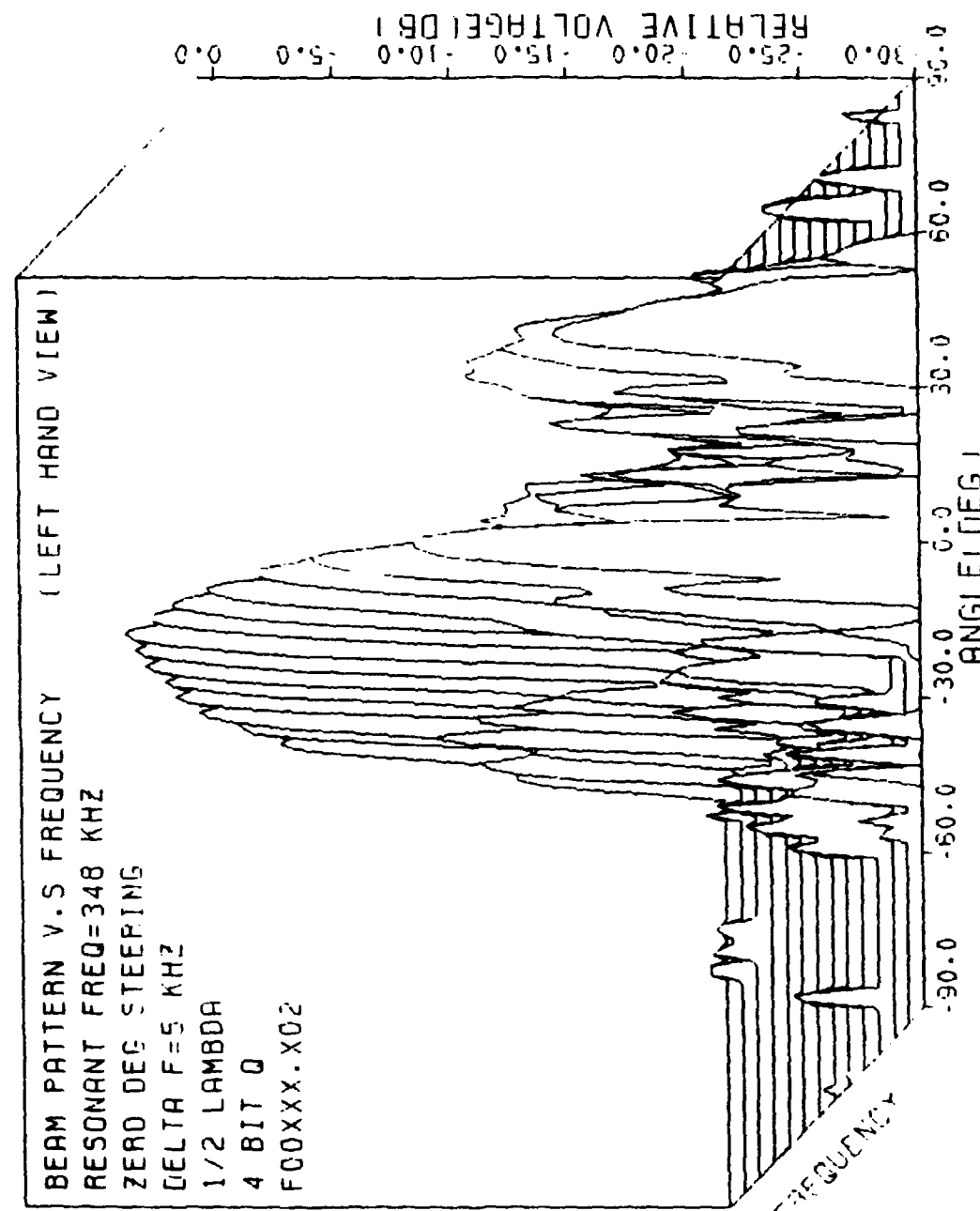


FIG.22

Fig. 22 30 view of 0° beam (left hand view)

0=1/2 LAMBDA 4 BIT Q. UNIFORM SHADING  
20 STAVES DISCRETE TYPE  
EXPERIMENTAL DATA

卷之三

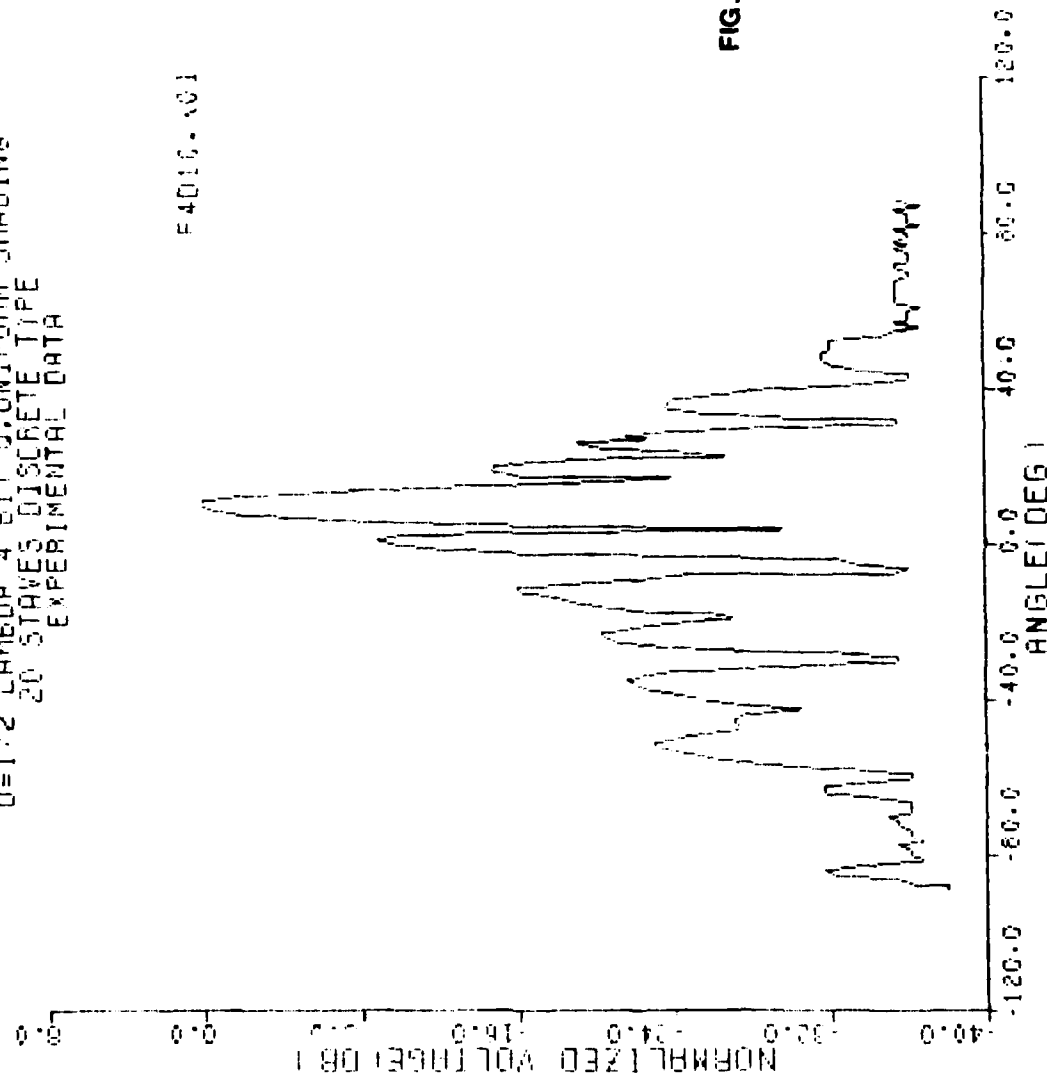


Fig. 23a Beam pattern,  $\frac{1}{2}\lambda$ , 4 bit quantization, discrete plate

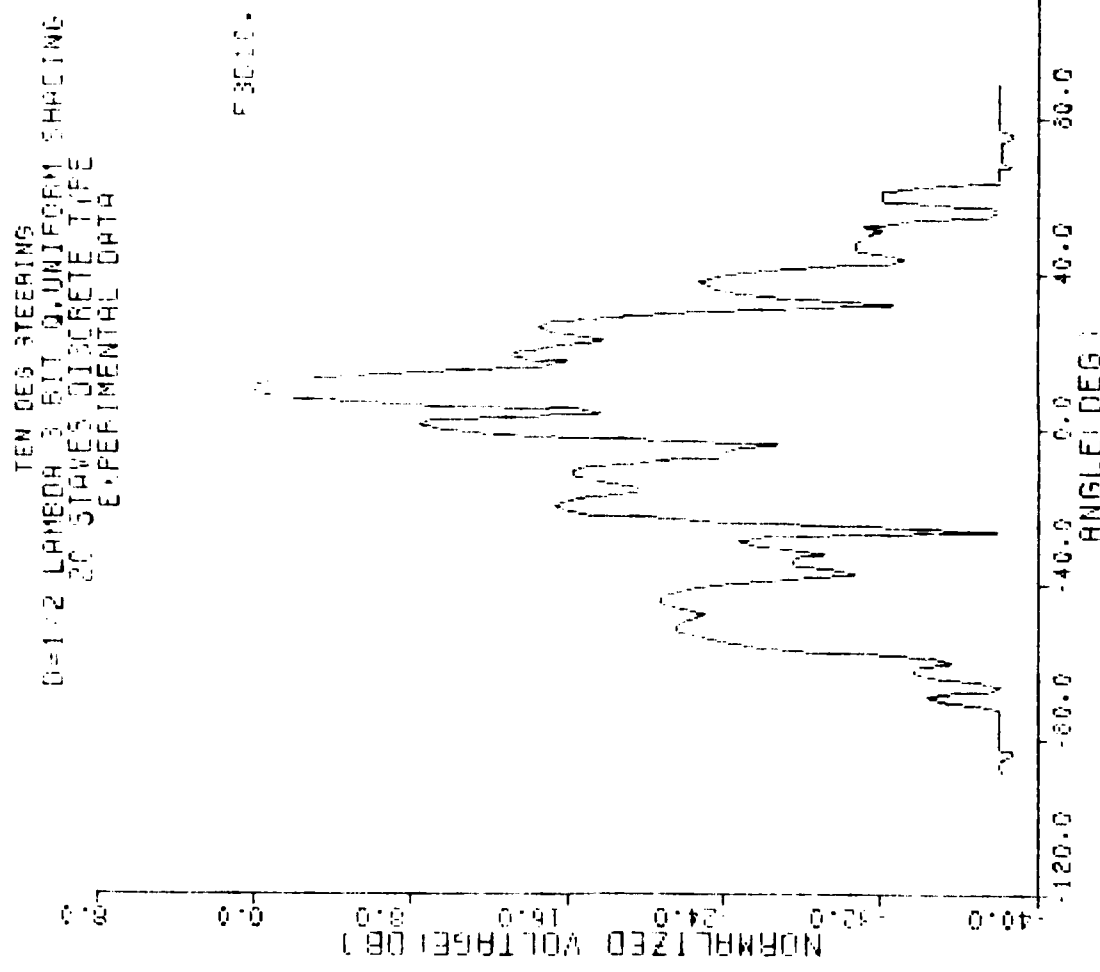


FIG. 23b

Fig. 23b Beam pattern,  $\frac{1}{2} \lambda$ , 3 bit quantization, discrete plate

10 DEG STEERING  
 $\Gamma = 1.12$  LAMBDA/2 GUIT Q. UNIFORM CHROMING  
 20 STAVES DISCRETE TYPE  
 EXPERIMENTAL DATA

F2010 • 013

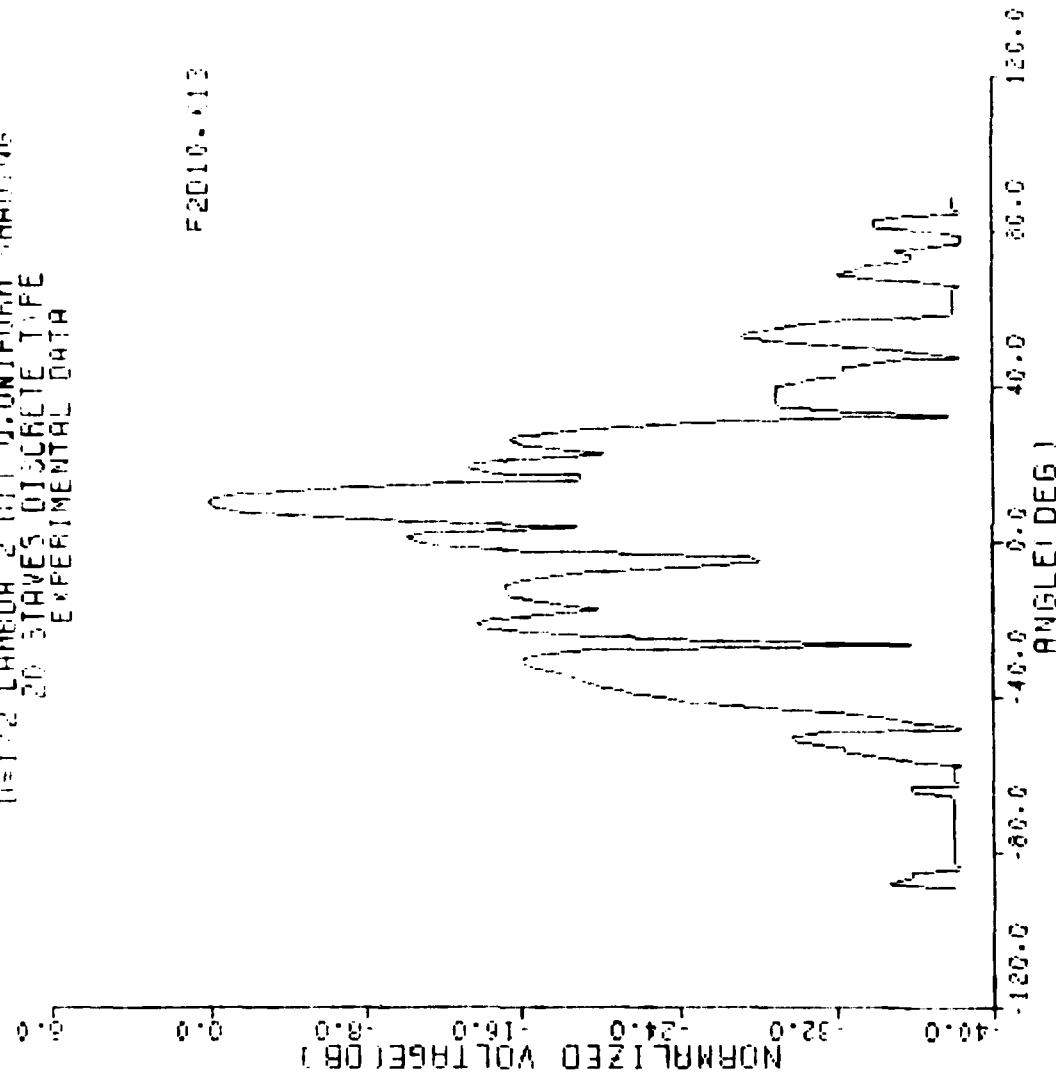


FIG.23c

Fig. 23c Beam pattern,  $\frac{1}{2} \lambda$ , 2 bit quantization, discrete plate

two bit, respectively. The first side-lobe of the main beam for the four bit is -9.5 db versus the side-lobe of about -8.5 db and -8 db for the three and two bit, respectively. The better performance of the four bit quantization can also be seen at -50° where the side-lobe is at -24 db versus the side-lobes of -20 db and -16 db for the three and two bit cases, respectively. The effect of quantization ranges (2-6 db) at -23° and (1-2 db) for the first side-lobe.

Figure 24a, 24b and 24c shows a 5° steered beam for  $1/2\lambda$  spacing in a continuous plate for four, three and two bit, respectively. All side-lobes for the continuous plate are lower than those of the discrete plate and the effect of phase quantization is also smaller for the continuous plate. The first side-lobe is about -15 db for all the quantizations. The four bit has a side-lobe of about -19 db at a 28° angle. The three and two bit shows the same side-lobe at about -14 db and -17 db, respectively, which is not too much improvement at that particular angle. But at -12° the side-lobe for the two bit is about -16 db versus -24 db of the three bit quantization. This is rather a good improvement in the side-lobe structure of a continuous plate.

5 IN. STEERING  
25 STRAWS CONTINENTAL DATA  
2 LAMBOA 4 BIT DYNAMIC TYPE  
EXPERIMENTAL DATA



FIGURE 24a

FIG. 24a

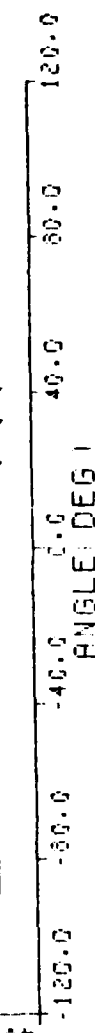


Fig. 24a Beam pattern,  $\frac{1}{2} \lambda$ , 4 bit quantization, continuous plate

FIVE DEG STEERING  
 $\Omega = 1/2 \text{ LAMBDA}$  ; EIT Q, UNIFORM SHADING  
 20 STAVES CONTINUOUS TIME  
 EXPERIMENTAL DATA

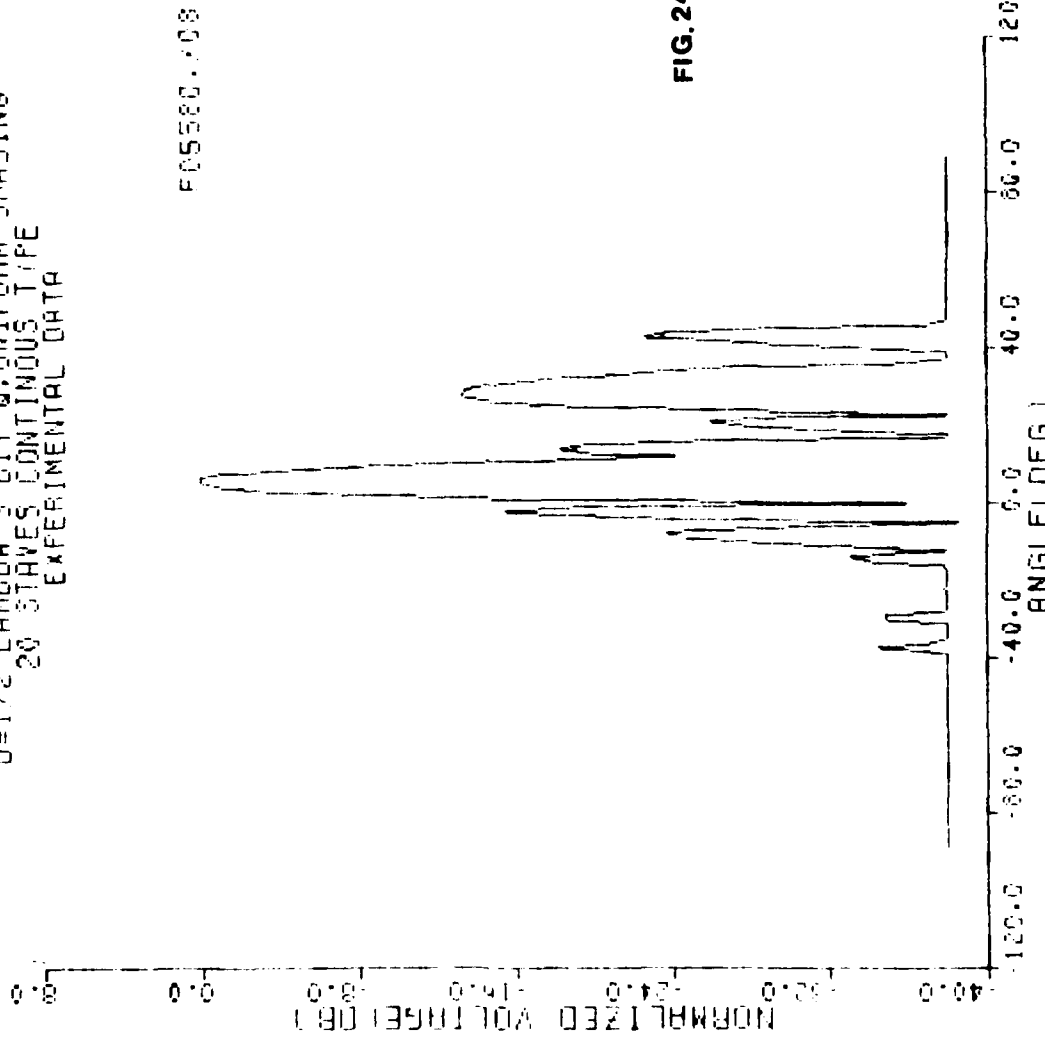


Fig. 24b Beam pattern,  $\frac{1}{2} \lambda$ , 3 bit quantization, continuous plate

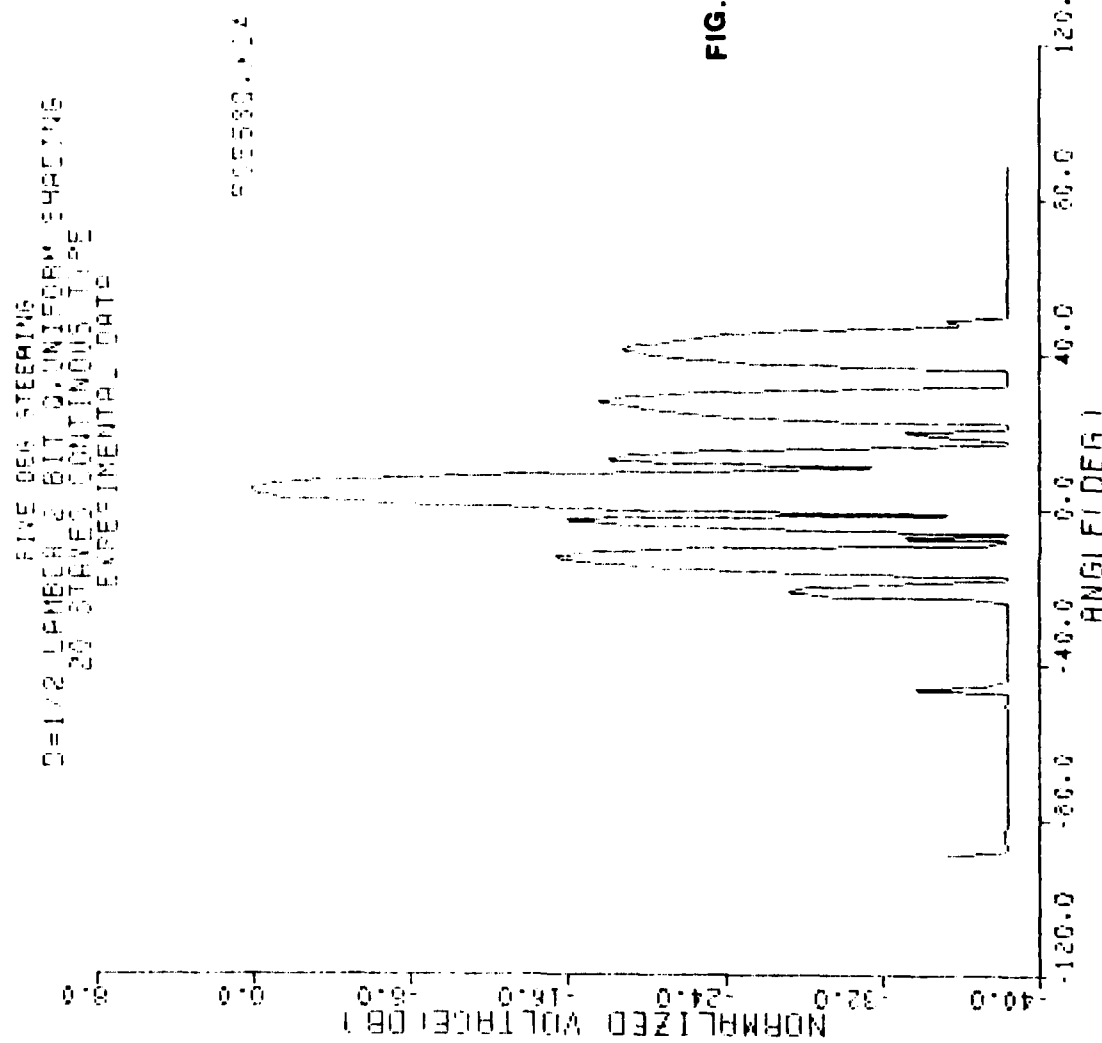


FIG. 24c

Fig. 24c Beam pattern,  $\frac{1}{2} \lambda$ , 2 bit quantization, continuous plate

The grating lobe in the discrete plate also shows a dependency on the quantization. Figure 25a, 25b and 25c shows a  $5^\circ$  steered beam for  $2\lambda$  spacing for four, three and two bit, respectively. The first grating lobe for four bit quantization is about -14 db. The three and two bit also show that they have grating lobes of about -12 db and -10 db, respectively, at about  $-28^\circ$  angle. The four bit quantization is shown to have a considerably reduced grating lobe compared to the others.

For a continuous plate, the grating lobe was considerably reduced because of the spatial filtering effect. The effect of coarser quantization is also shown to be less than for the discrete plate. Figure 26a, 26b and 26c shows a  $5^\circ$  steered beam for  $2\lambda$  spacing. The grating lobe is about -30, -24, -24 for four, three and two bit, respectively.

For the continuous plate the mirror lobe was suppressed more effectively with four bit quantization because of the finer phase adjustment that was available to drive the last three segments for cancellation. Figure 27a, 27b and 27c shows a  $10^\circ$  steering for  $1\lambda$  spacing, uniform shading for four, three and two bit quantization, respectively. The four bit quantization effect on the mirror lobe is about -22 db versus the -20 and -19.5 db for the three and two bit, respectively.

FIVE DEG STEERING  
 $\Delta$ =2 LAMBDA 4 BIT UNIFORM SHADING  
 5 STRAVES DISCRETE TIME  
 EXPERIMENTAL DATA

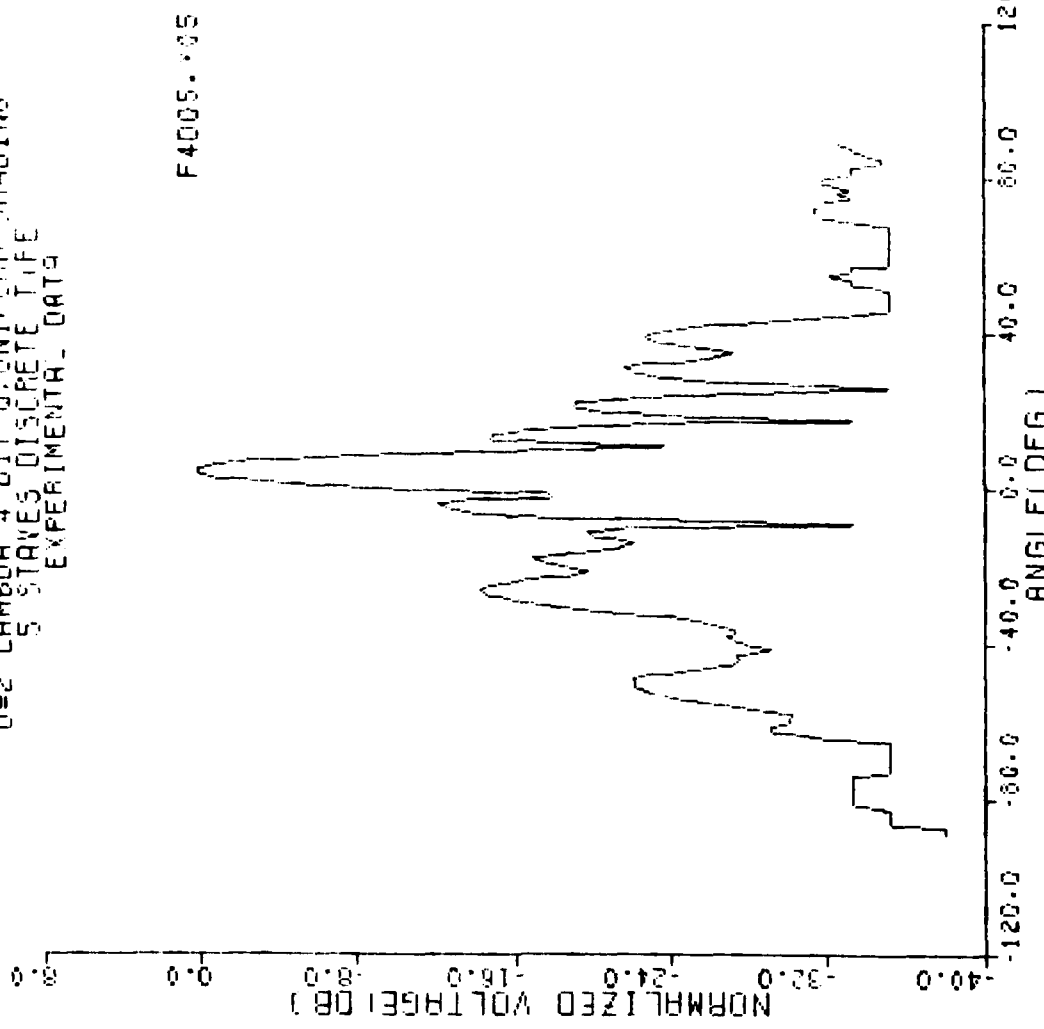


Fig. 25a Beam pattern, 5° steering, 4 bit quantization, discrete plate

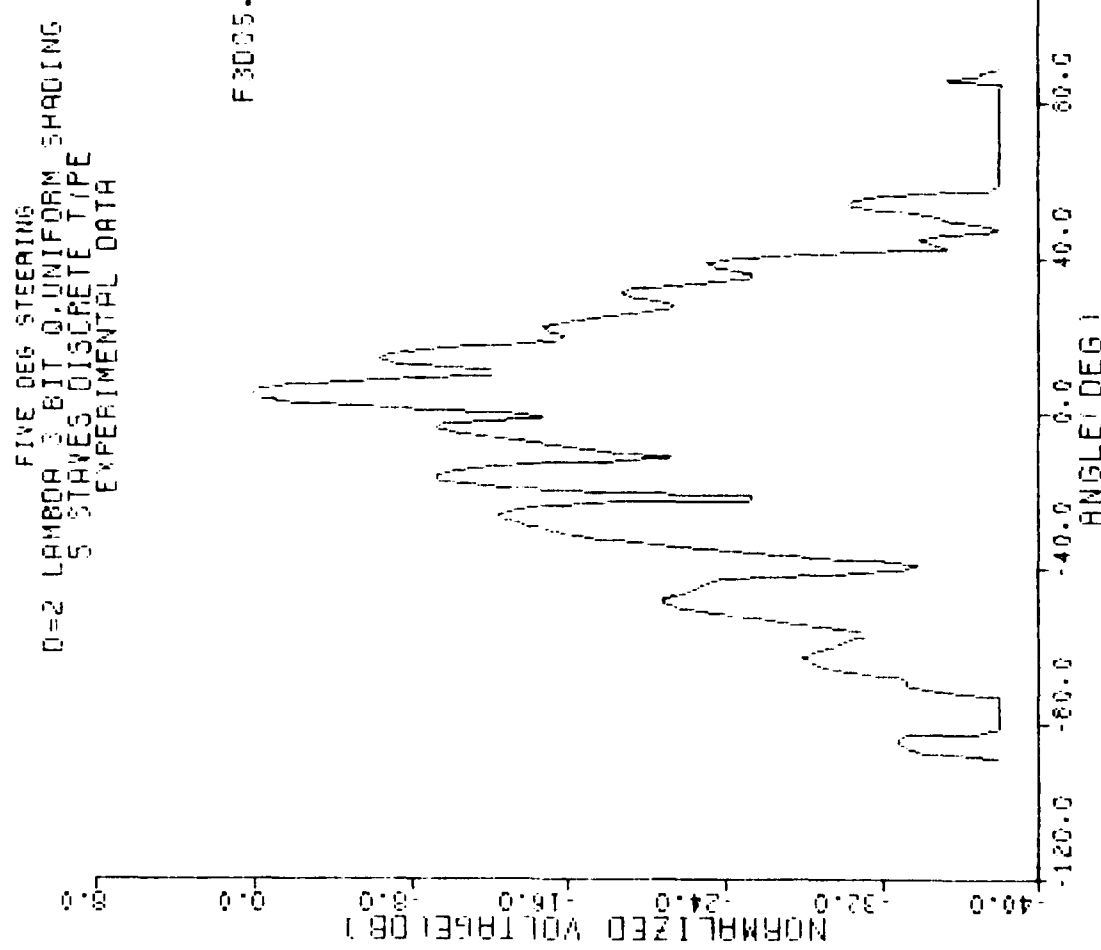


Fig. 25b Beam pattern, 5° steering, 3 bit quantization, discrete plate

FINE DEG STEERING  
D=2 LAMBDA 0.2 BIT Q. UNIFORM SHADING  
5 STAVES DISCRETE TIME  
EXPERIMENTAL DATA

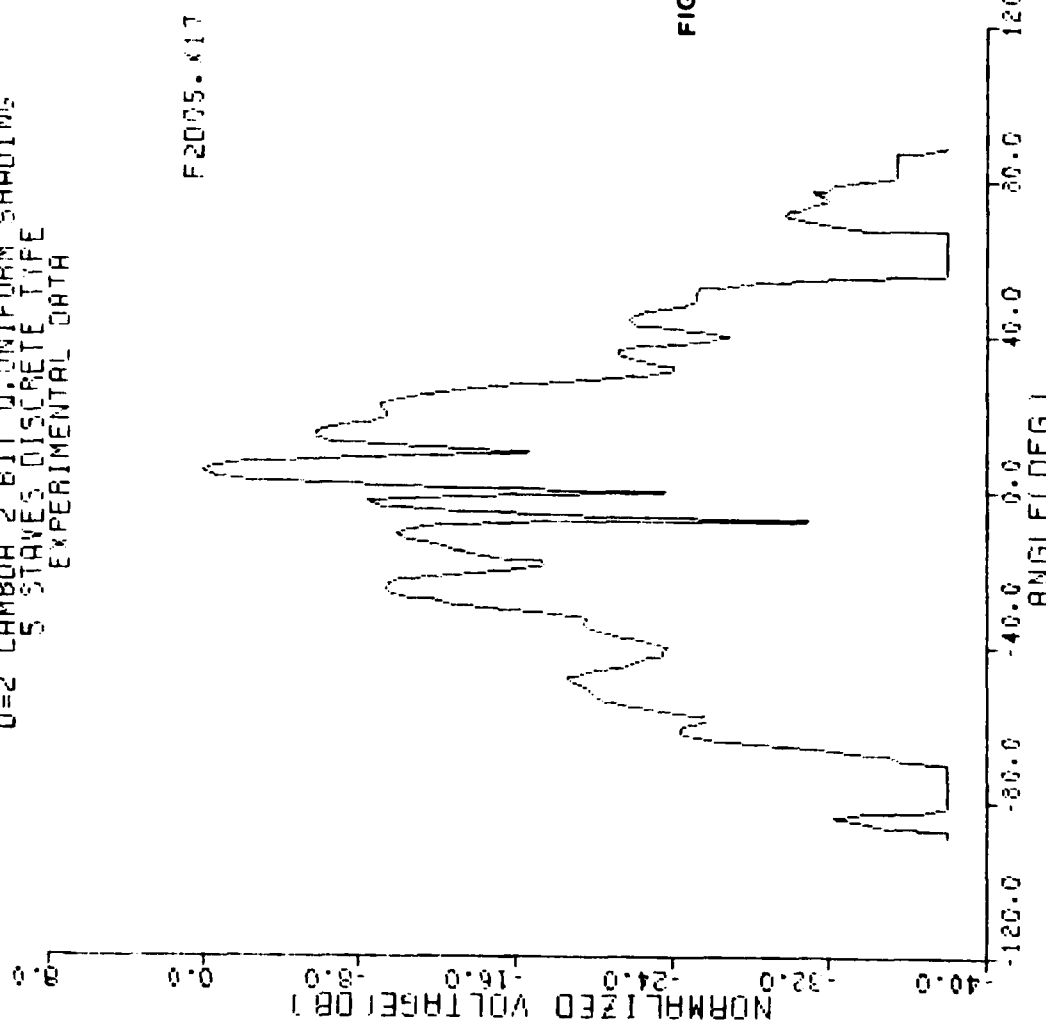


Fig. 25c Beam pattern, 5° steering, 2 bit quantization, discrete plate

FIVE DEG STEERING  
 $\lambda/2$  LAMBDA 4 BIT Q. UNIFORM SHADING  
 $\lambda/2$  STAVES CONTINUOUS TYPE  
 EXPERIMENTAL DATA

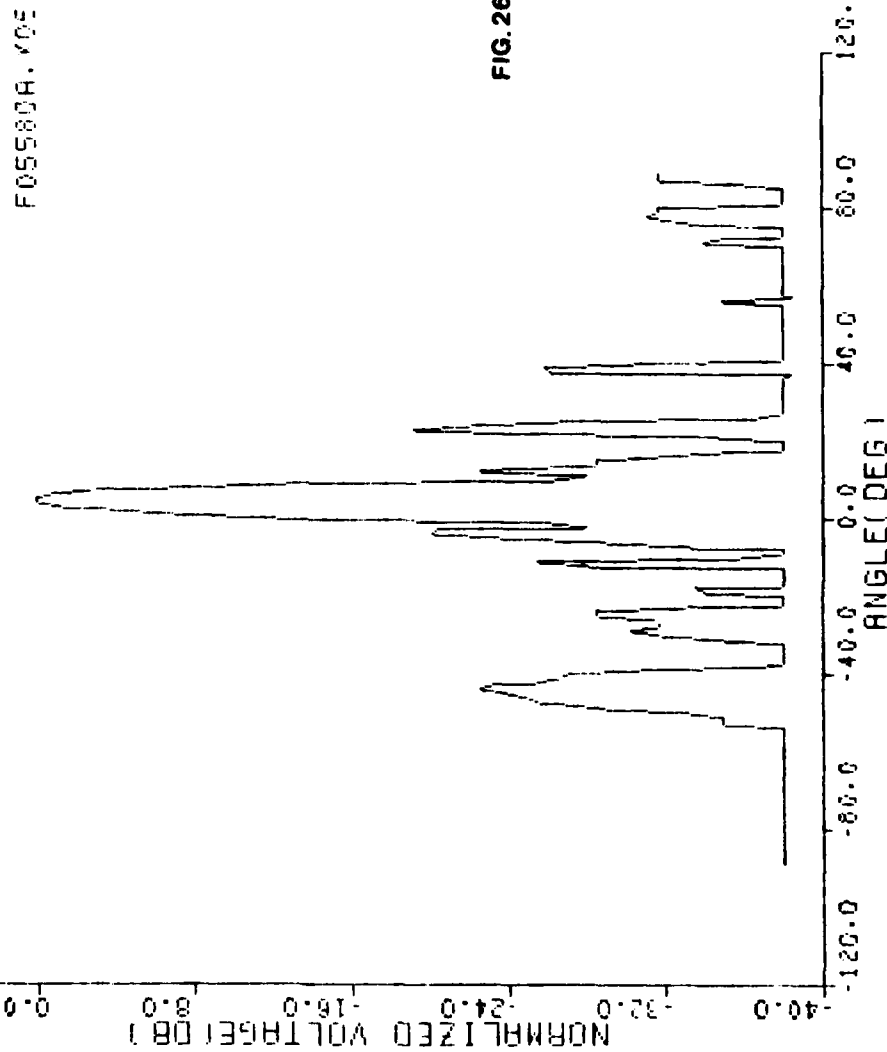


Fig. 26a Beam pattern,  $5^\circ$  steering,  $2\lambda$ , 4 bit quantization, continuous plate

0=2 LAMBDA 3 BIT Q. UNIFORM SHADING  
 5 STAVES CONTINUOUS TYPE  
 EXPERIMENTAL DATA

FIG. 26b

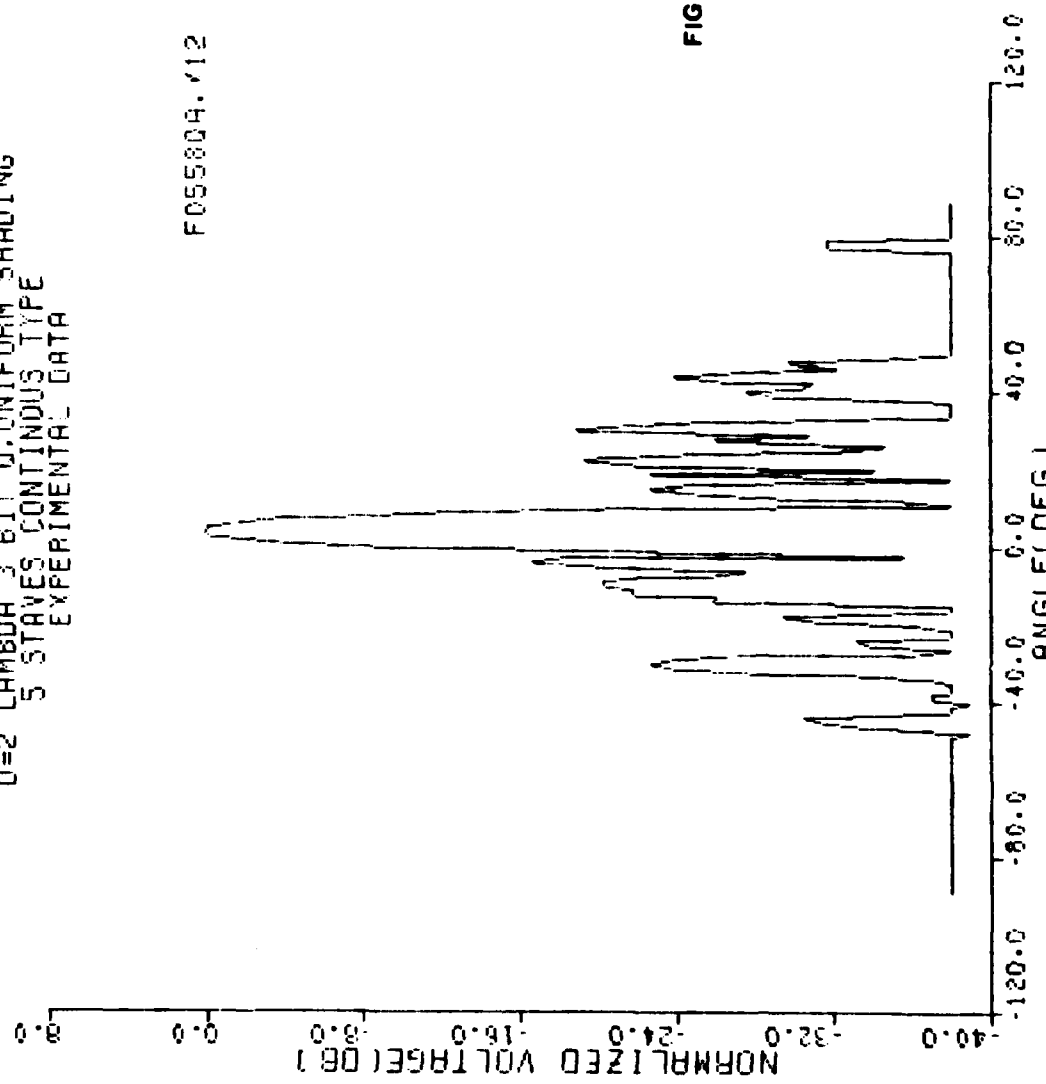


Fig. 26b Beam pattern,  $5^\circ$  steering,  $2\lambda$ , 3 bit quantization, continuous plate

D=2 LAMBDA 2 BIT Q. UNIFORM SHADING  
 5 SHAVES CONTINUOUS TYPE  
 EXPERIMENTAL DATA

F05580A. x18

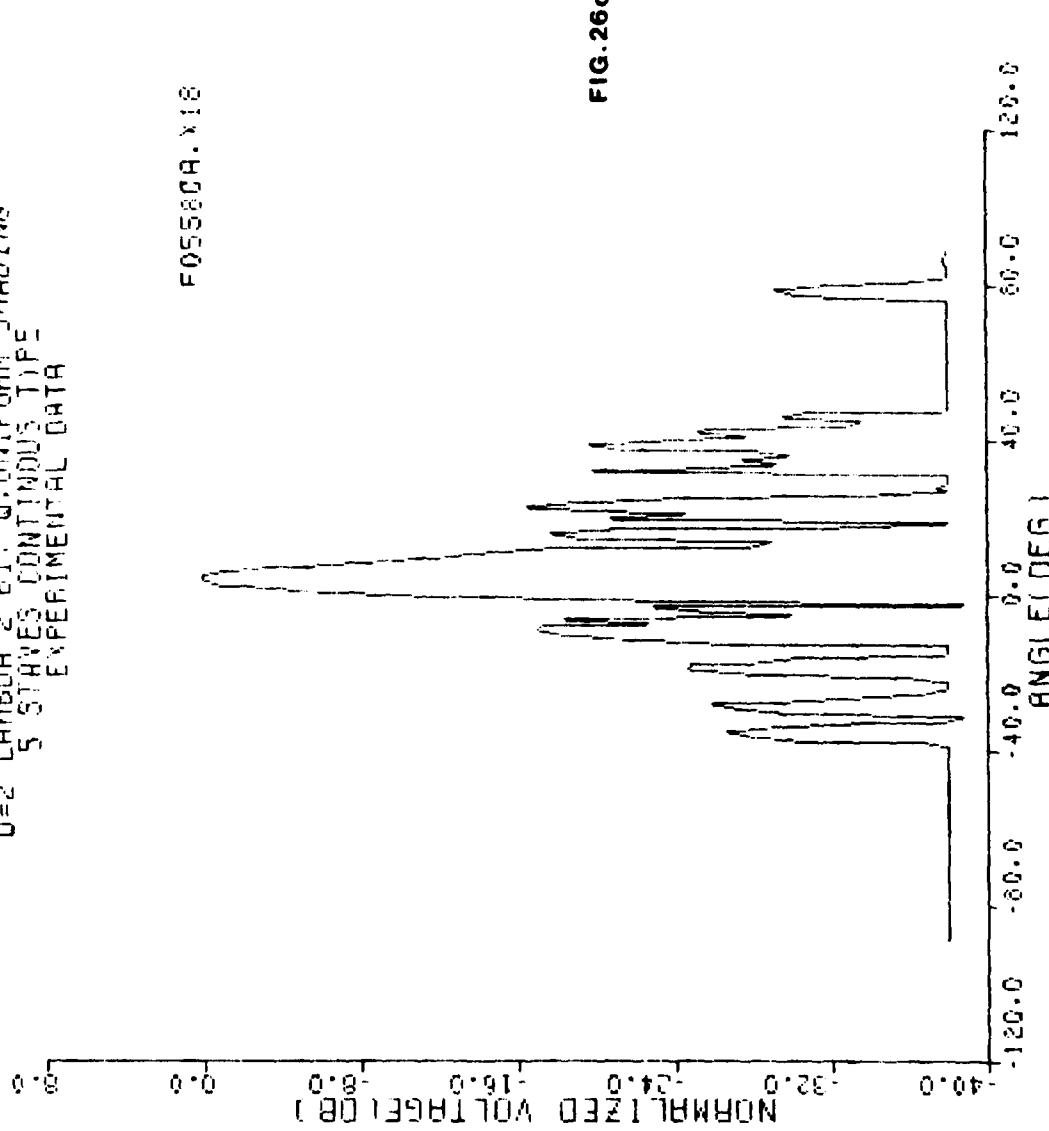


Fig. 26c Beam pattern,  $5^\circ$  steering,  $2\lambda$ , 2 bit quantization, continuous plate

D=1/2 LAMBDA 4 BIT Q. UNIFORM SHADING  
 20 STRIVES CONTINUOUS TYPE  
 EXPERIMENTAL DATA

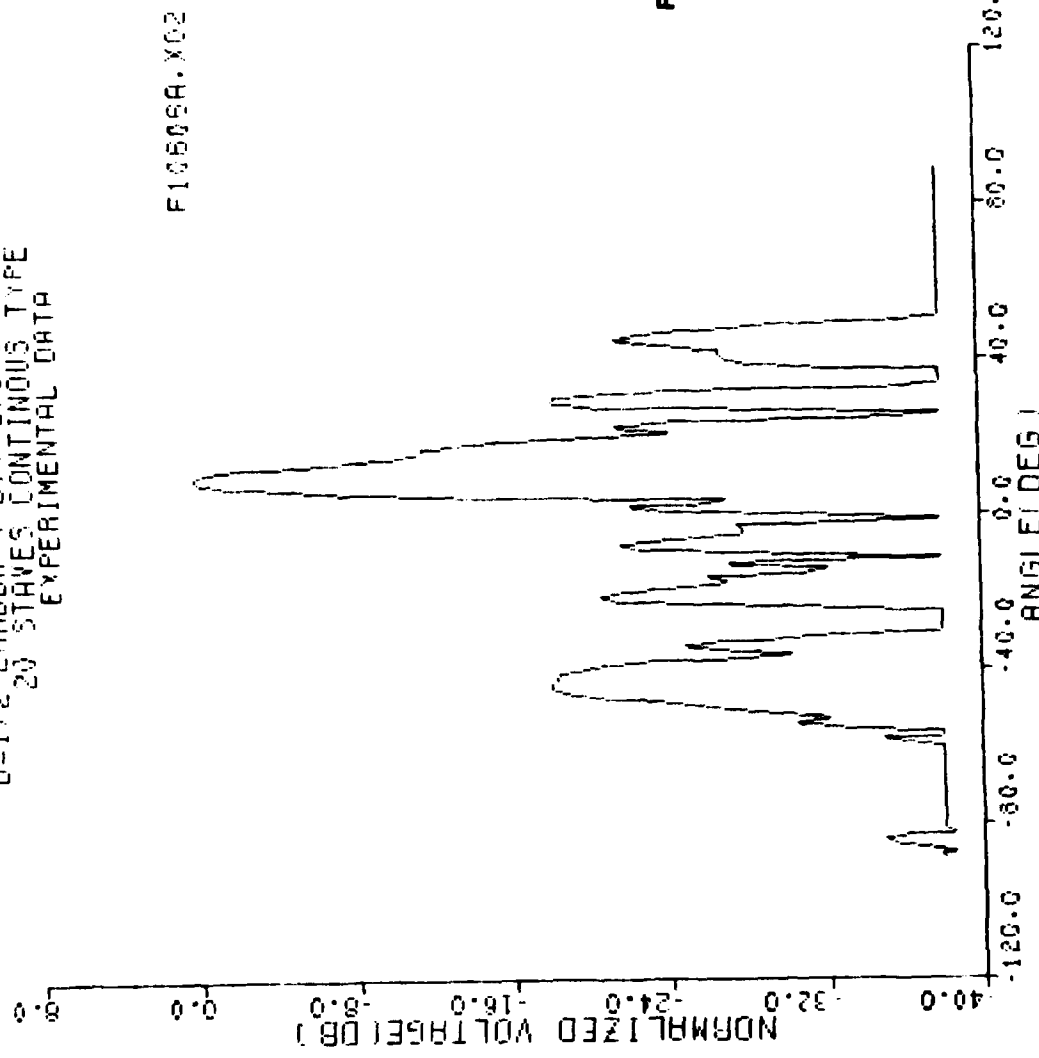


Fig. 27a Beam pattern,  $10^\circ$  steering,  $\frac{1}{2} \lambda$ , 4 bit quantization, continuous plate

Reproduced from  
best available copy.

TEN DEG STEERING  
 $\lambda/2$  LAMBDA SIT Q. UNIFORM SHADING  
 $2\lambda$  SPHERE CONTINUOUS TYPE  
 EXPERIMENTAL DATA

FIG. 27b

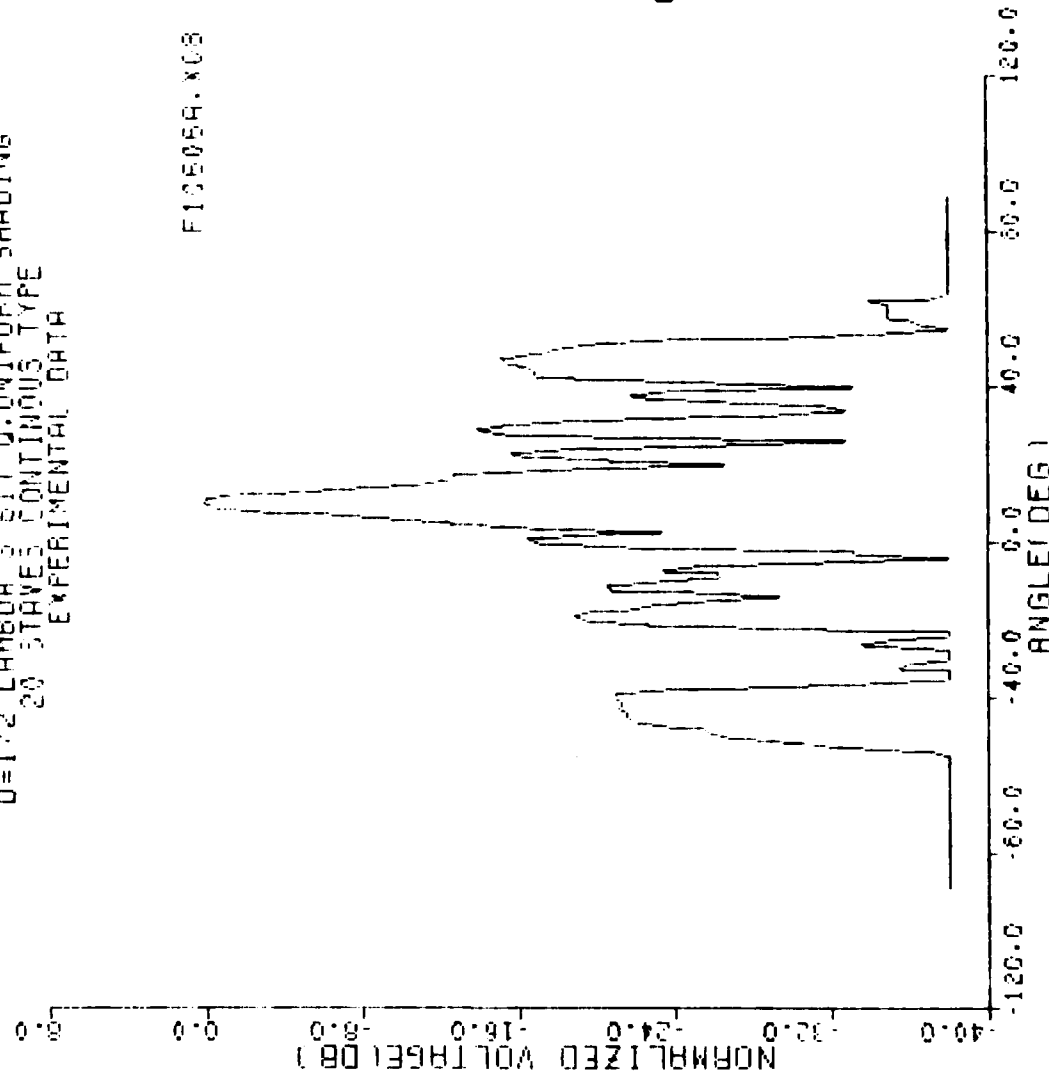
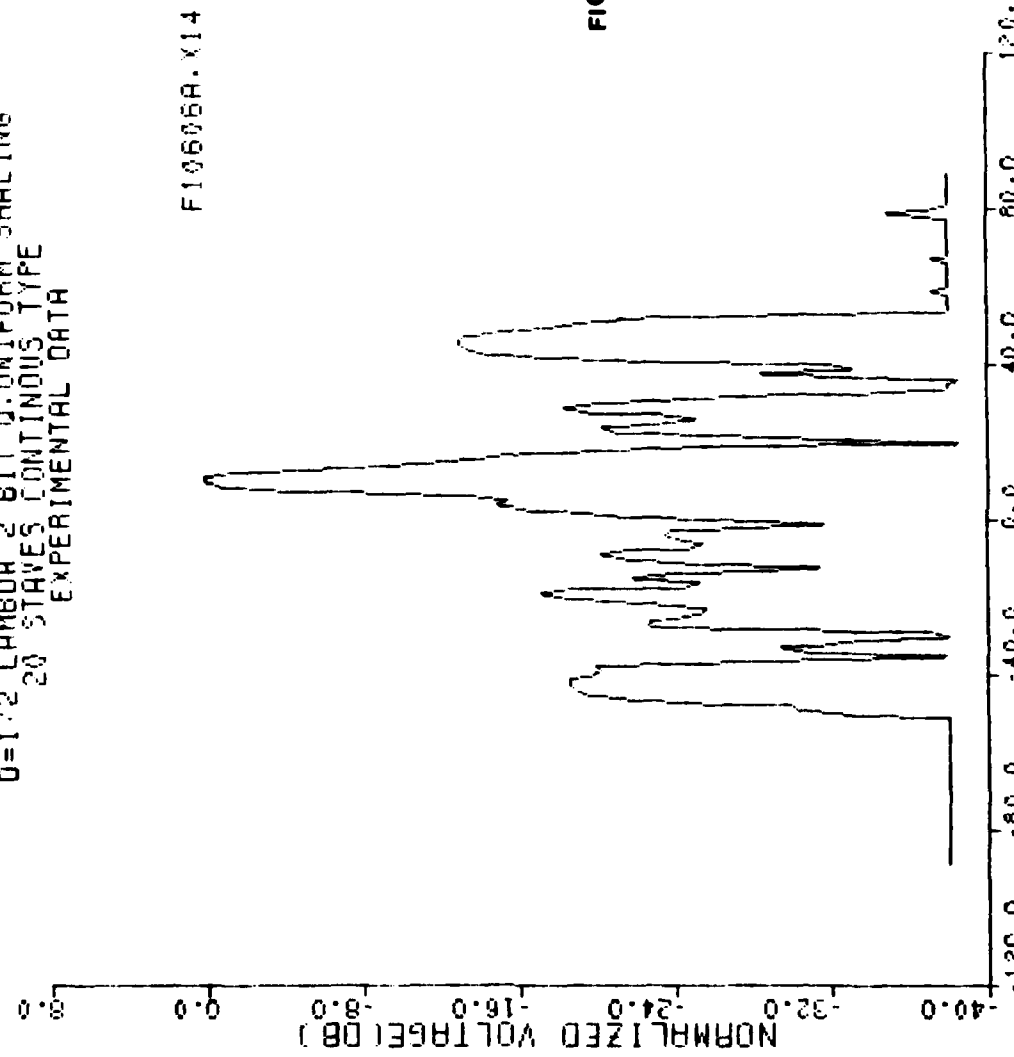


FIG. 27b

Fig. 27b Beam pattern,  $10^\circ$  steering,  $\frac{1}{2} \lambda$ . 3 bit quantization,  
 continuous plate

TEN DEG STEERING  
 $\Omega = 1/2 \lambda$  MAMBA 2 BIT Q. UNIFORM SHADING  
 20 STRIPES CONTINUOUS TYPE  
 EXPERIMENTAL DATA



continuous plate

Fig. 27c Beam pattern,  $10^\circ$  steering,  $\frac{1}{2} \lambda$ , 2 bit quantization,

CHAPTER IV  
CONCLUSION

#### 4.0 Conclusion

The purpose of this thesis was the study of the radiating properties of a segmented continuous piezoelectric plate transducer in comparison with a discrete segmented plate. Continuous plates have been shown to have both advantages and disadvantages. The major advantages of the continuous plates are the spatial filtering effect and ease of fabrication. The disadvantages are spurious shear lobes and mirror lobes, and a narrow operating frequency bandwidth.

The spatial filtering effect of the continuous plate had a very noticeable impact on the grating lobes. This effect was evaluated both theoretically and experimentally. The theoretical analysis was carried out by computing the response of the plate in wavenumber space and using that response as a weighting function on the wavenumber spectrum of the impressed driving voltage. Experimental measurements confirmed the theoretical predictions. The first grating lobe for the continuous plate was down to -29 db compared to -4 db for the discrete plate.

The spatial filtering effect of the continuous piezoelectric plate transducer served to smooth the side-lobe

structure significantly. The side-lobe performance of the continuous plate was lower than that of the discrete plate. The first side lobe for the continuous plate was down -12 db compared to -8 db for the discrete plate.

The spatial spectrum of quantized drive for different phasing was also investigated for four, three and two bit. The four bit quantization gave the best performance compared to the two bit quantization for both continuous and discrete plate. The first side lobe for the four bit quantization in a continuous plate was down -12 db compared to -10 db for the two bit quantization for  $2\lambda$  spacing and  $10^\circ$  steering, a degradation of 2 db due to quantization. The first side lobe for the four bit quantization of the discrete plate was down -9 db compared to -3 db of the two bit quantization for  $2\lambda$  spacing and  $10^\circ$  steering, showing a greater degradation of 6 db.

In the continuous plate the mirror and shear lobes were shown in Chapter II to be of major concern. The mirror lobe was generated by the reflection of the travelling wave from the edge boundary which created a standing wave. The mirror lobe was experimentally cancelled by actively driving the last three segments out of phase, which reduced the mirror lobe by about

18 db. Shear lobes were experimentally observed to be at approximately  $42^\circ$ . These were symmetrical shear waves which were weakly coupled to the electrical drive.

A suggestion which could be made here is to passively suppress both the mirror lobe and shear lobe by using a proper damping at the edges of the continuous plate to eliminate a standing shear wave or normal mode which might be generated in the continuous plate.

A very important physical advantage of the continuous plate over the discrete plate may be in the ease of fabrication, especially for high frequencies. At high frequencies, wavelengths are small and fabrication of a multi-element array is difficult, particularly for imaging sonars working in the megahertz region with apertures on the order of 100 wavelengths. For narrow scanning apertures the conducting electrode of the continuous plate can be cut at rather large spacing (greater than  $1/2$  wavelength) without worrying about the grating lobes, since they will be reduced by the spatial filtering effect of the continuous plate. The necessity of dicing the fragile ceramic plate may also be circumvented by merely using individual electrodes created by silk screening the electrode pattern initially or created by etching a continuous electrode surface.

ONR/MPL GENERAL DISTRIBUTION LIST

Chief of Naval Research  
Department of the Navy  
Arlington, Virginia 22217  
Code 200, 220(2), 102C  
410, 420, 430, 440,  
422-PO, 425-AC, 460

ONRDET  
NSTL Station  
Bay St. Louis, Mississippi 39529  
Code 420, 421, 422CS, 422CB,  
422PO, 425-GG

Director  
Office of Naval Research  
Branch Office  
1030 East Green Street  
Pasadena, California 91101

Commander  
Naval Sea Systems Command  
Washington, D. C. 20362  
Code 63, 63R, 63R-23

Defense Advanced Res. Proj. Agency  
TTO - Tactical Technology Office  
1400 Wilson Boulevard  
Arlington, Virginia 22209  
Atten: CDR Kirk Evans

Commander  
Naval Air Systems Command  
Washington, D. C. 20361  
Code 370

Commander  
Naval Ship Res. & Dev. Center  
Bethesda, Maryland 20084

Director  
Strategic Systems Proj. Ofc. (PM-1)  
Department of the Navy  
Washington, D. C. 20361  
Code NSP-2023

Commander  
Naval Surface Combat Systems Center  
White Oak  
Silver Spring, Maryland 20910

Commanding Officer  
Civil Engineering Laboratory  
Naval Construction Battalion Center  
Port Hueneme, California 93043  
Code L40, L42

Commanding Officer  
Naval Ocean Research and  
Development Activity (NORDA)  
NSTL Station  
Bay. St. Louis, Mississippi 39529  
Code 100, 110, 300, 330,  
340, 350, 360, 500

Commander  
U.S. Naval Oceanographic Office  
NSTL Station  
Bay St. Louis, Mississippi 39522  
Bill Jobst

Commander  
Submarine Development Group ONE  
Fleet Post Office  
San Diego, California 92152

Commander  
Naval Electronics Systems Command  
Washington, D. C. 20360  
Code PME-124, 3204

Commanding Officer  
U.S. Naval Air Development Center  
Attention: Jim Howard  
Warminster, Pennsylvania 18974

Executive Secretary, Naval Studies  
Board  
National Academy of Sciences  
2101 Constitution Avenue, N.W.  
Washington, D.C. 20418

Commander  
Naval Ocean Systems Center  
San Diego, California 92152  
Code 00, 01, 16, 94, 531  
5301, 71, 72

Commanding Officer  
Naval Underwater Systems Center  
Newport, Rhode Island 28044  
John D'Albora

Officer in Charge  
Naval Underwater Systems Center  
New London Laboratory  
New London, Connecticut 06320  
Code 900, 905, 910, 930, 960

Assistant Secretary of the Navy  
(Research Engineering & Systems)  
Department of the Navy  
Washington, D. C. 20350

STOIAC  
Battelle Columbus Laboratories  
505 King Avenue  
Columbus, Ohio 43201

National Oceanic & Atmospheric  
Administration  
Ocean Engineering Office  
6001 Executive Boulevard  
Rockville, Maryland 20852

Superintendent  
U.S. Naval Postgraduate School  
Monterey, California 93940

Director of Admin. Services  
Campus,  
University of Alaska  
Fairbanks, Alaska 99701

Director  
Applied Physics Laboratory  
Johns Hopkins University  
Johns Hopkins Road  
Laurel, Maryland 20810  
Atten: J. R. Austin

Director  
Applied Physics Laboratory  
University of Washington  
1013 East 40th Street  
Seattle, Washington 98105

Office of Naval Research  
Resident Representative  
c/o Univ. of California, San Diego  
La Jolla, California 92093

University of California, San Diego  
Marine Physical Laboratory Branch Office  
La Jolla, California 92093

Director of Research  
U.S. Naval Research Laboratory  
Washington, D. C. 20375  
Code 2620, 2627, 5000, 5100, 5800

Commanding Officer  
Naval Coastal Systems Laboratory  
Panama City, Florida 32401

Director  
Defense Documentation Center  
(TIMA), Cameron Station  
5010 Duke Street  
Alexandria, Virginia 22314

Institute for Defense Analyses  
1801 N. Beauregard St.  
Alexandria, Virginia 22311

Chief Scientist  
Navy Underwater Sound Reference Div.  
U.S. Naval Research Laboratory  
P.O. Box 8337  
Orlando, Florida 32806

Supreme Allied Commander  
U.S. Atlantic Fleet  
ASW Research Center, APO  
New York, New York 09019  
Via: ONR 100 M, CNO OP092D1,  
Secretariat of Military,  
Information Control, Committee

Director  
Applied Research Laboratory  
Pennsylvania State University  
P.O. Box 30  
State College, Pennsylvania 16802

Director  
The Univ. of Texas at Austin  
Applied Research Laboratory  
P.O. Box 8029  
Austin, Texas 78712

Director  
Woods Hole Oceanographic Institution  
Woods Hole, Massachusetts 02543

National Science Foundation  
Washington, D. C. 20550

July 1984

**END**

**FILMED**

**9-85**

**DTIC**